ROGÉRIO PAES MENEZES FILHO

ANALYSIS AND IMPLEMENTATION OF CALIBRATION METHODS FOR MAGNETOMETERS AND ACCELEROMETERS

LAVRAS – MG

2021

ROGÉRIO PAES MENEZES FILHO

ANALYSIS AND IMPLEMENTATION OF CALIBRATION METHODS FOR MAGNETOMETERS AND ACCELEROMETERS

Thesis presented to the Universidade Federal de Lavras, in partial fulfillment of the requirements for the degree of Master of Science in the Graduate Program of Systems and Automation Engineering.

Prof. Dr. Felipe Oliveira e Silva

Advisor

LAVRAS – MG

2021

Ficha catalográfica elaborada pelo Sistema de Geração de Ficha Catalográfica da Biblioteca Universitária da UFLA, com dados informados pelo(a) próprio(a) autor(a).

Menezes Filho, Rogério Paes.
Analysis and Implementation of Calibration Methods for Magnetometers and Accelerometers / Rogério Paes Menezes Filho. - 2021.
144 p. : il.

Orientador(a): Felipe Oliveira e Silva.

Dissertação (mestrado acadêmico) - Universidade Federal de Lavras, 2021.
Bibliografia.

1. Calibration. 2. Magnetometers. 3. Accelerometers. I. e Silva, Felipe Oliveira. II. Título.

ROGÉRIO PAES MENEZES FILHO

ANALYSIS AND IMPLEMENTATION OF CALIBRATION METHODS FOR MAGNETOMETERS AND ACCELEROMETERS

Thesis presented to the Universidade Federal de Lavras, in partial fulfillment of the requirements for the degree of Master of Science in the Graduate Program of Systems and Automation Engineering.

APPROVED on April 22, 2021.

Prof. Dr. Felipe Oliveira e Silva	UFLA
Prof. Dr. Bruno Henrique Groenner Barbosa	UFLA
Prof. Dr. Helio Koiti Kuga	INPE

Prof. Dr. Felipe Oliveira e Silva
Advisor

LAVRAS – MG
2021

To my family.

ACKNOWLEDGEMENTS

First and foremost, I would like to thank God, the Father Almighty, Jesus Christ, His only Son, and the Holy Spirit.

To my wonderful parents Rogério P. Menezes and Ana Paula T. Menezes, and my kind sister Ana Luiza T. Menezes, for their endless love and extraordinary support.

To my lovely girlfriend Sara C. Abreu, for her incessant love and encouragement.

To my brilliant advisor Prof. Felipe O. Silva, for his devoted support, patience, meticulous reviews, and for giving me the honor of working with him.

To my colleagues from Universidade Federal de Lavras (UFLA), Ícaro Viterbre, Leonardo Vieira, Lucas Paiva, Victor Hugo Pereira, for their assistance and friendship; a special thanks to Gustavo Carvalho, who greatly helped me with the laboratory experiments.

To the faculty of the Graduate Program of Systems and Automation Engineering.

Finally, to my thesis committee members, Prof. Bruno H. G. Barbosa and Prof. Helio K. Kuga, who promptly accepted my invitation.

"Requiem aeternam dona ets, Domine,
et lux perpetua luceat ets.
Te decet hymnus, Deus, in Sion,
et tibi reddetur votum in Jerusalem.
Exaudi orationem meam,
ad te omnis caro veniet.
Requiem aeternam dona ets, Domine,
et lux perpetua luceat ets."

Wolfgang Amadeus Mozart - Requiem

ABSTRACT

Throughout human history, navigation has always been an elementary necessity, from hunting to traveling overseas, and even outside of planet Earth. Agriculture is another area where navigation is progressively required, especially in the scope of the so-called precision agriculture, which considers and handles intrinsic spatial variabilities along cultivations. In order to meet the demands for navigation, numerous techniques have been developed; one of the most used and known is the GNSS (Global Navigation Satelite System) technology, which can provide navigation aid in a broad range of accuracy and cost. Navigation based on IMUs (Inertial Measurement Units) and AHRSs (Attitude and Heading Reference Systems), on the other hand, which basically consist of inertial and magnetic sensors, follows a complementary pattern in terms of cost benefit. Despite being possible, navigation systems based on only one navigation technique often do not produce a sufficiently accurate navigation solution, since those individual technologies, such as marine-grade IMUs and accurate GNSS signals, are generally too expensive. A possible solution for producing low-cost, high-precision navigation systems is the combination of different navigation techniques into an integrated system via sensor fusion. One of the biggest challenges involving low-cost inertial and magnetic sensors, especially the latter, is that their measurements are strongly corrupted by inherent and external errors. Such errors can be so compromising as to make it impossible to use the corrupted measurements for navigation purposes. In addition to sensor fusion, which contributes to the mitigation of errors, calibration techniques can precisely estimate systematic errors, which, then, can be compensated for. Therefore, this work analyzes and implements current calibration techniques for magnetometers and accelerometers. One of the objectives is to determine the suitability/robustness of the investigated algorithms for consumer-grade sensors. As the main contribution of this work, numerical and analytical solutions are presented for the compensation of systematic errors from intermediate estimates computed via one of the addressed methods. In addition, the work provides a complete mathematical description of the investigated calibration techniques, both for each type of sensor individually and for several types simultaneously. For validation purposes, the algorithms are subjected to simulations and comparisons with the results obtained via the proposed solutions, followed by implementations in hardware. Finally, a traditional magnetometer calibration method, for which new numerical and analytical solutions have been proposed, is adapted for the calibration of accelerometers.

Keywords: Calibration. Magnetometers. Accelerometers.

RESUMO

Ao longo da história humana, a navegação tem sido uma necessidade elementar, desde a caça, às viagens marítimas, e até mesmo extraplanetárias. A agricultura é mais uma área que progressivamente requer navegação, especialmente no âmbito da chamada agricultura de precisão, onde variabilidades espaciais intrínsecas às plantações são consideradas e tratadas. Para suprir as demandas por navegação, várias técnicas foram desenvolvidas; uma das mais usadas e conhecidas é a tecnologia GNSS (Sistema de Navegação Global por Satélites), que pode prover navegação em uma larga faixa de precisão e custo. A navegação baseada em IMUs (Unidades de Medição Inercial) e AHRSs (Sistemas de Referência de Orientação e Rumo), por outro lado, os quais são compostos basicamente por sensores inerciais e magnéticos, segue um padrão complementar em termos de custo-benefício. Embora seja possível, muitas vezes sistemas de navegação baseados em apenas uma técnica de navegação não produzem uma solução de navegaçao suficientemente precisa, já que tais meios, como *marine-grade* IMUs e sinais de GNSS precisos, são geralmente dispendiosos. Uma possível solução para produzir sistemas de navegação de baixo custo e alta precisão é a combinação de diferentes técnicas de navegação em um sistema integrado via fusão sensorial. Um dos maiores desafios envolvendo sensores inerciais e magnéticos de baixo custo, especialmente os últimos, é que suas medições são fortemente corrompidas por erros inerentes e externos. Tais erros podem ser tão comprometedores a ponto de impossibilitar a utilização das medições por eles corrompidas para fins de navegação. Além da fusão sensorial, que contribui para a mitigação de erros, técnicas de calibração podem estimar com alta precisão erros sistemáticos, que podem ser compensados nas medições. Portanto, este trabalho analisa e implementa técnicas atuais para a calibração de magnetômetros e acelerômetros. Um dos objetivos é determinar a adequação/robustez dos algoritmos investigados para sensores com nível de desempenho *consumer-grade*. Como principal contribuição deste trabalho, soluções numéricas e analíticas são apresentadas para a compensação de erros sistemáticos a partir de estimativas intermediárias de um dos métodos abordados. Ademais, o trabalho fornece a descrição matemática completa dos métodos de calibração investigados, tanto para cada tipo de sensor individualmente, quanto para vários tipos simultaneamente. Para fins de validação, os algoritmos são submetidos a simulações e comparações com os resultados obtidos a partir das soluções propostas, seguidas pelas implementações em *hardware*. Por fim, um tradicional método de calibração de magnetômetros, para o qual as novas soluções numéricas e analíticas foram propostas, é adaptado para a calibração de acelerômetros.

Palavras-chave: Calibração. Magnetômetros. Acelerômetros.

LIST OF FIGURES

LIST OF TABLES

LIST OF SYMBOLS

b_x x-axis bias

b_y y-axis bias

b_z z-axis bias

$\boldsymbol{m}$ uncorrupted magnetic field density

$\tilde{\boldsymbol{m}}$ measured magnetic field density

$\hat{\boldsymbol{m}}$ estimated magnetic field density

m_t magnitude of Earth's local magnetic field density

m_h magnitude of Earth's local horizontal magnetic field density

m_x uncorrupted x-axis magnetic field density

m_y uncorrupted y-axis magnetic field density

m_z uncorrupted z-axis magnetic field density

$\tilde{m}_x$ measured x-axis magnetic field density

$\tilde{m}_y$ measured y-axis magnetic field density

$\tilde{m}_z$ measured z-axis magnetic field density

$\boldsymbol{c}_b$ bias vector

$\hat{\boldsymbol{c}}_b$ estimated bias vector

C_m misalignment matrix

$\hat{C}_m$ estimated misalignment matrix

$\boldsymbol{c}_\mu$ noise vector

C_s scale factor matrix

$\hat{C}_s$ estimated scale factor matrix

$\boldsymbol{f}$ uncorrupted specific force vector

$\tilde{\boldsymbol{f}}$ measured specific force vector

$\hat{\boldsymbol{f}}$ estimated specific force vector

f_x uncorrupted x-axis specific force

f_y uncorrupted z-axis specific force

f_z uncorrupted z-axis specific force

$\tilde{f}_x$ measured x-axis specific force

$\tilde{f}_y$ measured z-axis specific force

$\tilde{f}_z$ measured z-axis specific force

g gravity vector

λ misalignment between the z-axis of the sensor frame and the yz-plane of the body frame

ϕ misalignment between the z-axis of the sensor frame and the xz-plane of the body frame

ρ misalignment between the y-axes of the body and sensor frames

s_x x-axis scale factor

s_y y-axis scale factor

s_z z-axis scale factor

X_{2D} least-squares estimates from the two-dimensional calibration method ETS

X_{3D} least-squares estimates from the three-dimensional calibration method ETS

LIST OF ABBREVIATIONS AND ACRONYMS

ABS	Anti-lock Breaking System
AHRS	Attitude and Heading Reference System
ANN	Artificial Neural Network
EKF	Extended Kalman Filter
GA	Genetic Algorithm
GNSS	Global Navigation Satelite System
IFOG	Interferometric Fiber Optic Gyro
IGRF	International Geomagnetic Reference Field
IMU	Inertial Measurement Unit
INS	Inertial Navigation System
MAME	Mean Absolute Magnitude Error
MAPE	Mean Absolute Percentage Error
MEMS	Microelectromechanical Systems
MLE	Maximum Likelihood Estimator
MVEE	Minimum-Volume Enclosing Ellipsoid
RLG	Ring Laser Gyro
RLS	Recursive Least-Squares
UAV	Unmanned Aerial Vehicles
UF	Unscented Filter
UKF	Unscented Kalman Filter
WMM	World Magnetic Model

CONTENTS

1 INTRODUCTION

The term *navigation* may be conceived differently by different authors. Groves (2013) and Thompson (1995), for instance, break down the concept into two distinct ideas: (a) science navigation, which stands for the determination of position and velocity of a moving body with respect to a reference point; (b) art of navigation, which relates to the planning of the trajectory between two points, avoiding obstacles and collisions. Throughout this work, definition (a) is adopted.

Inertial sensors and magnetometers are essential devices in many areas of industry, particularly those dependent on navigation systems technology. Although there are other approaches for navigation, such as Global Navigation Satellite System (GNSS), inertial sensors and magnetometers have their specific set of applications. For instance, whenever a GNSS cannot provide constant or accurate enough signal, there should be an alternative, which, in many cases, is an Inertial Measurement Unit (IMU) or an Attitude and Heading Reference System (AHRS). However, techniques can be implemented cooperatively, where one complements the shortcomings of the other.

In this study, we are primarily interested in techniques that can be implemented in the agricultural field, as it is a very technological demanding area and one of the main economical activities in Brazil (MOLIN; AMARAL; COLAÇO, 2015). In this context, a notably effective and emerging set of techniques is called precision agriculture, which aims to manage cultivations based on precise analyses, considering soil and climate variability (ZHANG; WANG; WANG, 2002). Geostatistics is used in order to analyze the spatial variabilities, and define the appropriate actions: e.g., fertilizing, irrigation, harvesting, etc. For this reason, machines employed in these processes must be aided with spacial referencing; hence, a minimally accurate navigation system is necessary in order to implement precision agriculture. Nevertheless, this type of technology is also interchangeably applied to a number of areas (GROVES, 2013), which reinforces even more the relevance of studies like this. Therefore, we do not restrict this work to any particular field, keeping it general, so readers from different areas can have the same understanding and applicability.

Even though GNSS can provide extremely accurate measurements, such precise services may be excessively costly for some small farmers, as also are precise IMUs and AHRSs. One possible solution for this problem comes from sensor fusion, which, in this case, consists of combining low-cost GNSS and IMU/AHRS to produce a more robust navigation solution.

One of the problems involving low-cost sensors is that they may present poor performance, being corrupted by many stochastic and systematic error sources. Magnetometers, in particular, can only be used for navigation purposes if they exclusively measure the Earth's magnetic field, like a compass. However, the Earth is not the only source of magnetic fields. Many ferromagnetic materials may be present in the surrounding of the sensor, producing and distorting the underlying magnetic fields. If the magnetometers sense such spurious fields, in addition to that produced by Earth, navigation is not possible. Therefore, compensating for corrupted measurements, i.e. calibration, is a central task in a navigation system. Fortunately, this topic has been broadly addressed by many authors throughout the years, and many effective methodologies have been proposed. Nonetheless, there is still much room for improvements and new investigations.

The main contributions of this work are twofold: (a) providing the reader with a comprehensive review on the main calibration methodologies available for magnetometers, including a full description of their mathematical implementation; (b) proposing novel numerical and analytical solutions that complement traditional existing calibration methodologies. Minor contributions of this work include the correction of errors detected in the papers that originally described the calibration techniques under investigation, the adaptation of a magnetometer calibration technique for accelerometers, and the execution of comprehensive experiments and analyses involving traditional methodologies and the novel procedures proposed here.

Some of the aforementioned contributions are being separated for posterior journal submissions, and some have already been presented and published in the proceedings of national and international conferences: (FILHO et al., 2020b) and (FILHO et al., 2020a).

This work is organized as follows. Chapter 2 reviews the concepts and technologies related to the sensors of interest, namely, accelerometers, gyroscopes and magnetometers. Section 2.1 presents a review on inertial sensors, i.e., accelerometers and gyroscopes, describes their main architectures, characterizes the errors that corrupt their measurements, and establishes an error model. Section 2.2 does the same as the previous, but for magnetometers. Chapter 3 provides a comprehensive literature review on the calibration techniques available for accelerometers, magnetometers and multiple sensors, including gyroscopes. In sequence, some of the most traditional magnetometer calibration techniques are mathematically described. Chapter 4 presents novel two-dimensional, numerical and analytical calibration solutions that complement the methodology proposed by Foster and Elkaim (2008), since the original work lacks in pro-

viding a complete procedure, yet presenting an effective estimation algorithm. In addition, real and simulated experiments, including a Monte Carlo analysis, are conducted in order to validate the proposed solutions. Chapter 5 contains the most important contributions of this work, which include the derivation of numerical and analytical solutions for the three-dimensional magnetometer calibration methodology presented by Foster and Elkaim (2008), correcting a previous attempt by Vasconcelos et al. (2011). Moreover, real and simulated experiments are exhaustively performed in order to validate the developed solutions and compare their performances with those of other calibration techniques investigated in this work. Chapter 6 extends the contribution of adapting the magnetometer calibration technique by Foster and Elkaim (2008) for accelerometer calibration. This adaptation also involves the solutions proposed in Chapter 5. Again, real and simulated experiments are conducted in order to validate the adapted calibration methodology. Finally, Chapter 7 recaps the entire work, analyzes the achieved contributions and suggests future work guidelines within the topic of inertial and (mainly) magnetic sensors calibration.

2 INERTIAL AND MAGNETIC SENSORS USED FOR NAVIGATION

In this chapter, we describe the inertial and magnetic sensors that are commonly used for navigation purposes, briefly addressing their constructive aspects, and focusing on characterizing the main sources of errors that corrupt their measurements.

2.1 Inertial Measurement Unit

An Inertial Measurement Unit (IMU) is a device capable of sensing the non-gravitational acceleration and angular velocity of a body with respect to an inertial reference. As the name suggests, it works based on the principle of inertia, namely, Newton's Laws of Motion; thus, inertial sensors – the components of an IMU – do not need an external reference/signal to operate, unlike other types of referencing approaches (TITTERTON; WESTON, 2004). There are two different types of inertial sensors to consider: accelerometers and gyroscopes (which is the terminology adopted here for any angular rate sensor based on inertia). In general, along with data processing, control, and power units, three accelerometers and three gyroscopes constitute an IMU, as displayed in Figure 2.1 (see (GROVES, 2013) for more details). Sections 2.1.1, 2.1.2, and 2.1.3 provide a more detailed explanation on inertial sensors; however, in short, accelerometers and gyros measure specific force acceleration and angular rate, respectively.

In order to categorize the different levels of IMU performance, the classification presented by Groves (2013) is adopted here; it classifies the levels of performance into five categories: *marine-grade*, *aviation-grade* (or navigation-grade), *intermediate-grade*, *tactical-grade*, and *automotive-grade* (or consumer-grade). First, considered the best category, the marine-grade is mostly used in ships, submarines, and some spacecraft; a marine-grade Inertial Navigation System (INS), which comprises a marine-grade IMU and a navigation processor (Figure 2.2), can cost more than one million US dollars and presents navigation-solution drift of less than 1.8 km per day. One category step below is the aviation-grade; it is largely used in commercial and military aircrafts; the price for one of these INSs is around US$100,000 and the performance can guarantee horizontal drift of less than 1.5 km for the first hour. Next, the intermediate-grade is used primarily in helicopters and small aircrafts; such an IMU costs from US$20,000 to US$50,000, and the performance is approximately one order of magnitude inferior compared to aviation-grade. Tactical-grade inertial sensors, which cost up to US$20,000, are usually used in guided weapons and Unmanned Aerial Vehicles (UAVs); they can only provide reliable stand-alone measurements for a few minutes. For this reason, GNSS is often a complemen-

Figure 2.1 – General IMU scheme that consists primarily of inertial sensors and auxiliary components

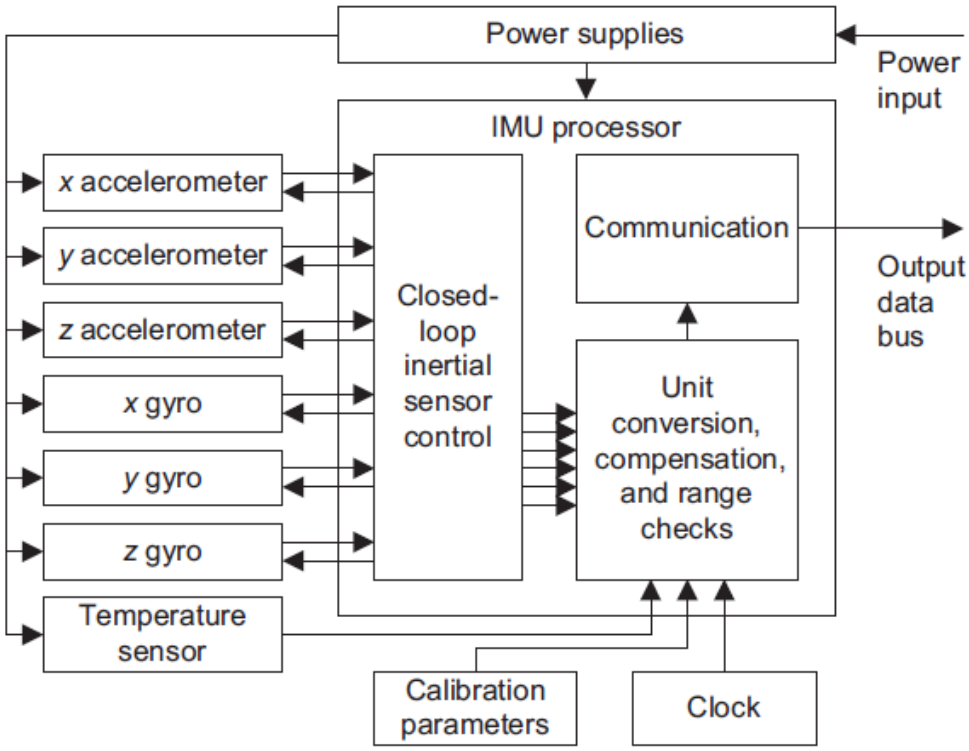

Source: (GROVES, 2013)

tary source of navigation for them. Lastly, the automotive-grade, mostly used for Anti-lock Breaking System (ABS), active suspension, and airbags, are commonly sold as individuals accelerometers and gyroscopes, whose price range from 1 to 10 US dollars; however, due to their poor accuracy, these sensors are generally not appropriate for navigation.

Figure 2.2 – Scheme of a basic Inertial Navigation System, which basically comprises an IMU plus a navigation processor

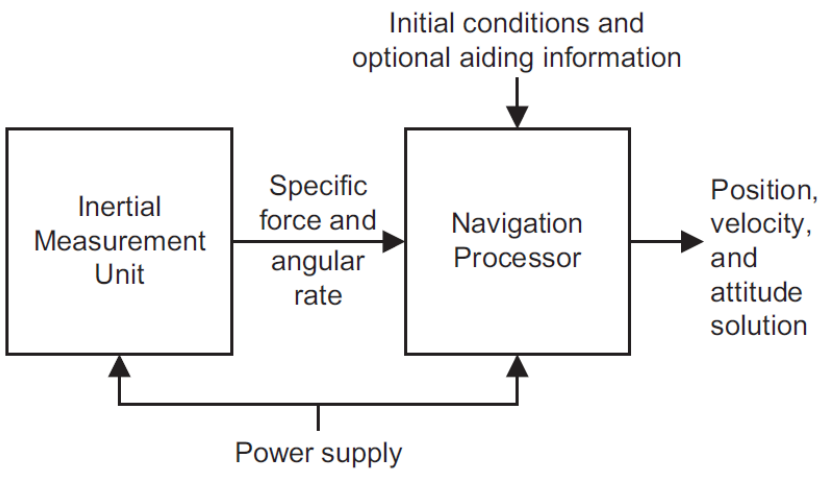

Source: (GROVES, 2013)

2.1.1 Accelerometers

In order to measure the translational motion of a rigid body, one could observe the resultant force applied upon it, and calculate the acceleration using Newton's Second Law of Motion (TITTERTON; WESTON, 2004). Therefore, the acceleration of a rigid body, which can be integrated twice over time to determine position, has a linear correlation with the applied force. As long as the mass is known, acceleration can be computed. However, instead of calculating the total force acting upon the whole body (e.g. an aircraft), it is convenient to restrict the measurements to a proof mass. The idea is presented in Figure 2.3, where a proof mass is free to move along a given displacement range, restricted only by two springs; the specific force is then proportional to the measured displacement.

Figure 2.3 – Basic accelerometer that transmits the inertial measurement idea of translational movements

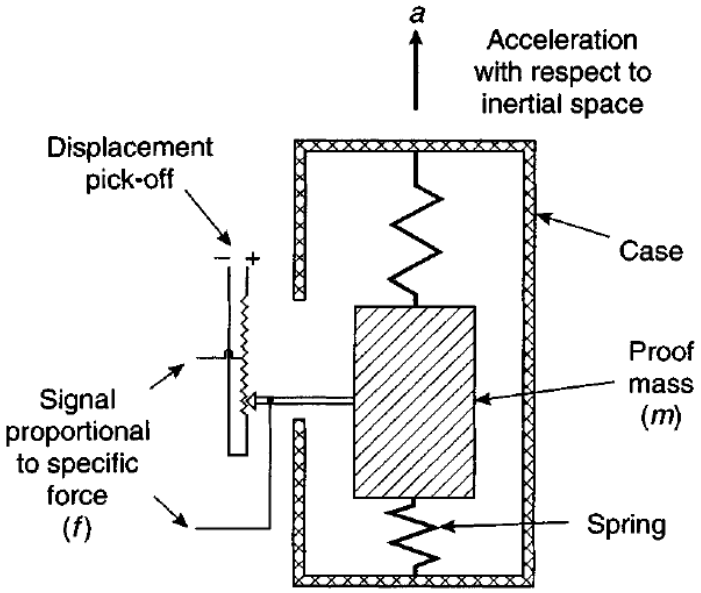

Source: (TITTERTON; WESTON, 2004)

The actual sensors are slightly more sophisticated than showed in Figure 2.3. Commercially available accelerometers commonly fall into one of the two categories: pendulous or vibrating-beam. In the first case, the proof mass is attached to a pendulous arm, which converts the translational motion described in Figure 2.3 into a rotation, as illustrated by Figure 2.4.

Nevertheless, there are three main drawbacks involving pendulous accelerometers: (a) resolution is limited by the pick-off length; (b) overtime, the springs may present hysteresis; (c) since the proof mass rotates around the hinge, the sensitive axis varies with respect to the case. In order to overcome these shortcomings, a control system is added to the sensor, preventing the proof mass from moving (Figure 2.5). In this case, instead of taking measurements from

Figure 2.4 – Scheme representing the pendulous accelerometer

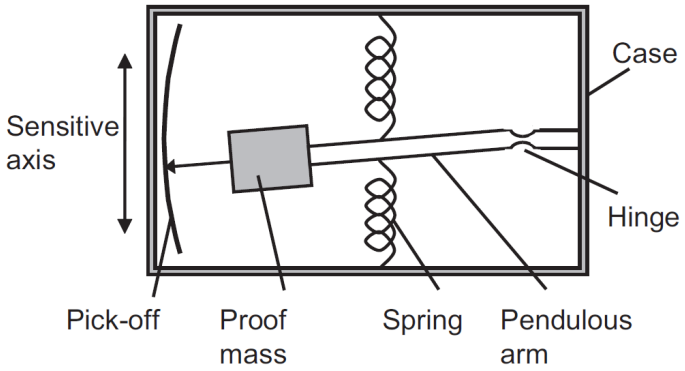

Source: (GROVES, 2013)

the pick-off, they are obtained from the torque exerted by the electromagnet (actuator), which is proportional to the applied specific force; besides, it provides improved resolution and linearity. However, whenever the sensor is not operating (energized), the proof mass is free to move inside the case, which is a considerable shortcoming, since these movements could damage the device, especially during transportation.

Figure 2.5 – Scheme of the force-feedback pendulous accelerometer

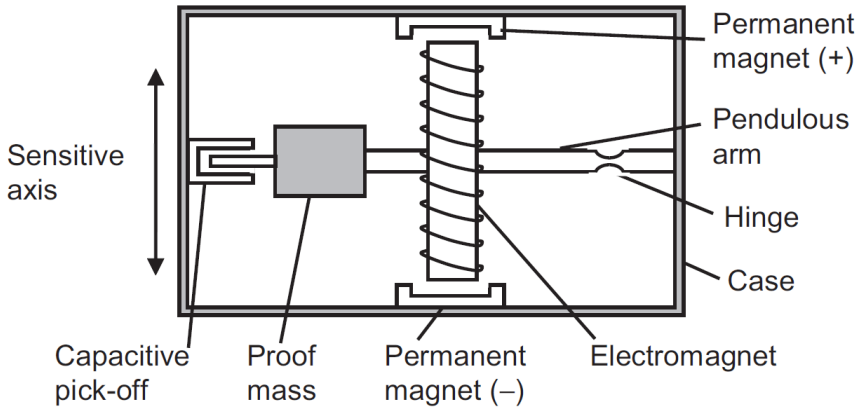

Source: (GROVES, 2013)

Similarly to pendulous accelerometers, vibrating-beam accelerometers are also largely used. These sensors estimate acceleration by measuring the resonant frequency of a vibrating-beam attached to a proof mass (Figure 2.6). This is possible because the resonant frequency of the beam varies according to the total force applied to the sensitive axis of the proof mass. This sensor has virtually no moving parts, which is an evident improvement, compared to pendulous accelerometers. Since 2005, Microelectromechanical Systems (MEMSs) have been expanding quite rapidly, which manifests the need for effective calibration techniques, considering their manufacturing limitations (GLUECK et al., 2014).

Figure 2.6 – Vibrating-beam accelerometer

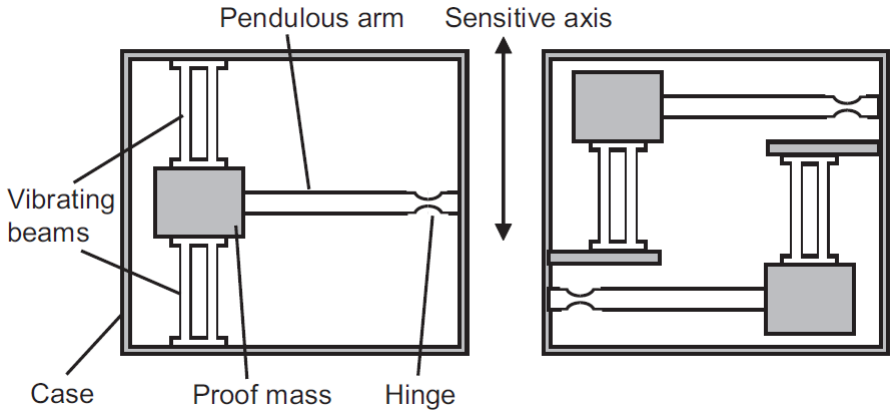

Source: (GROVES, 2013)

2.1.2 Gyroscopes

Gyroscopes are sensors that measure angular rate without any external reference; they can be classified into three main groups: spinning-mass, optical and vibratory gyros. Throughout history, these sensors have been considerably improved through the discovery of new technologies, as summarized in Figure 2.7.

Figure 2.7 – Gyroscopes development timeline

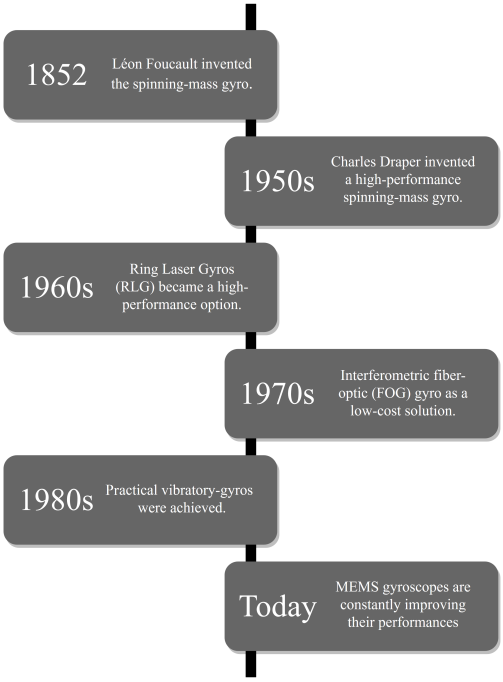

Source: Author

Spinning-mass gyros were the main source of self-contained angular position in the past, as explained by Draper (1958). However, this technology has been superseded by optical and

vibratory gyros. Essentially, a spinning-mass gyroscope works based on the idea of angular momentum conservation; a circular mass is continually rotated while a pick-off measures the displacement caused by a torque upon the sensitive axis. This approach, unfortunately, presents the same shortcomings reported for pendulous accelerometers, even when a closed-loop format is adopted.

Optical gyroscopes, on the other hand, do not have moving parts (except for the dither wheel, in Ring Laser Gyros (RLGs)), which eliminates most of the shortcomings existing in spinning-mass gyros. In this study, we categorize them into two groups: RLG and Interferometric Fiber Optic Gyro (IFOG). RLGs were the first that appeared as a viable option for strapdown IMU configuration in high dynamical environments, such as military vehicles (BARBOUR, 2010). Basically, two lasing modes (one in each direction) are generated inside the sensor cavity. When it is rotated around the sensitive axis, the frequency of one laser mode decreases, while the other increases; then, these changes in wavelength, later converted into angular rate, are sensed by a detector, as illustrated in Figure 2.8 (see (GROVES, 2013) for more details). Although RGLs are a well established technology in terms of performance, they are still an expensive option; thus, most improvements on these sensors focus on cost reduction, rather than performance enhancement (BARBOUR, 2010).

Figure 2.8 – Drawing of a ring laser gyro in a 2D plane perpendicular to the sensitive axis

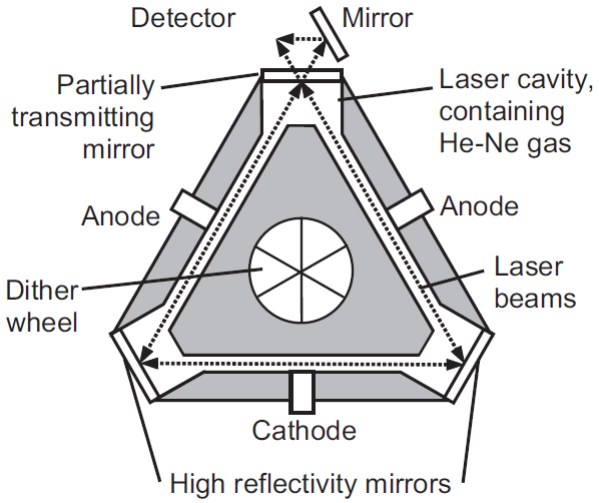

Source: (GROVES, 2013)

The other class of optical gyros presented here is the IFOG. Originally conceived as a cheaper alternative to RLGs (BARBOUR, 2010), IFOGs rely on the Sagnac effect: a light beam is split into two parts traveling in opposite directions inside a fiber-optic coil that can range from

100m to 3km in length (Figure 2.9); if rotation is applied to the axis perpendicular to the coil plane, the recombined beams will present a phase change that can be converted into angular rate. They have some advantages over RLGs that include: lower cost, weight and voltage requirements. However, there are also disadvantages, such as a more limited dynamic range.

Figure 2.9 – Interferometric fiber-optic gyro

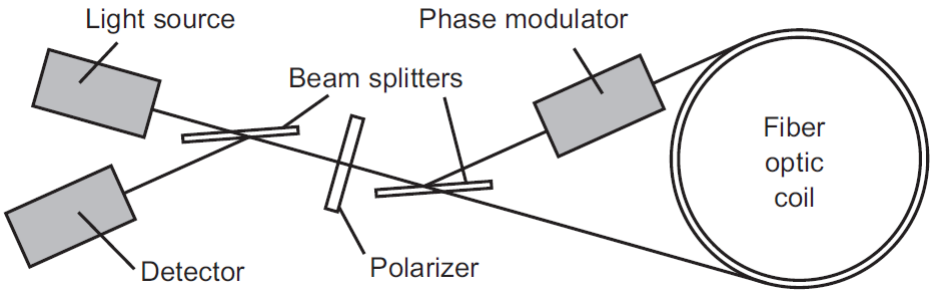

Source: (GROVES, 2013)

2.1.3 Error Characteristics

Inertial sensors exhibit at least four types of error: biases, scale factors, cross-coupling errors (misalignments), and random noise. They comprise four components: constant, temperature-varying, run-to-run, and in-run contribution. The constant (or fixed) component is generally compensated by the IMU processor, based on laboratory calibration parameters. Temperature-varying errors can also be modeled and compensated by prior estimation. The run-to-run contribution, which is the focus of this study, varies each time the sensor is turned on, but stays the same until power is turned back off. Therefore, these errors cannot be previously estimated, then, a calibration algorithm is required whenever the sensor is turned on. Lastly, the in-run component comprises errors that appear during sensor activity. Even though they cannot be fully estimated, integration with other sensors (sensor fusion) collaborates to mitigate them (GROVES, 2013).

2.1.3.1 Biases

Biases, which are present both in accelerometers and gyroscopes, have a static and a dynamic component. The first comprises the run-to-run contributions plus residual constant biases remaining from laboratory calibration; the latter stands for the in-run biases. They are expressed as: b_x, b_y, and b_z, which refer to biases along the x, y, and z-axes of the sensor

frame, respectively. Figure 2.10 shows the effect of a constant bias b on a sinusoidal signal that represents the measurements over time of an individual sensor (in one axis) of an IMU.

Figure 2.10 – Effect of bias on sensor measurements

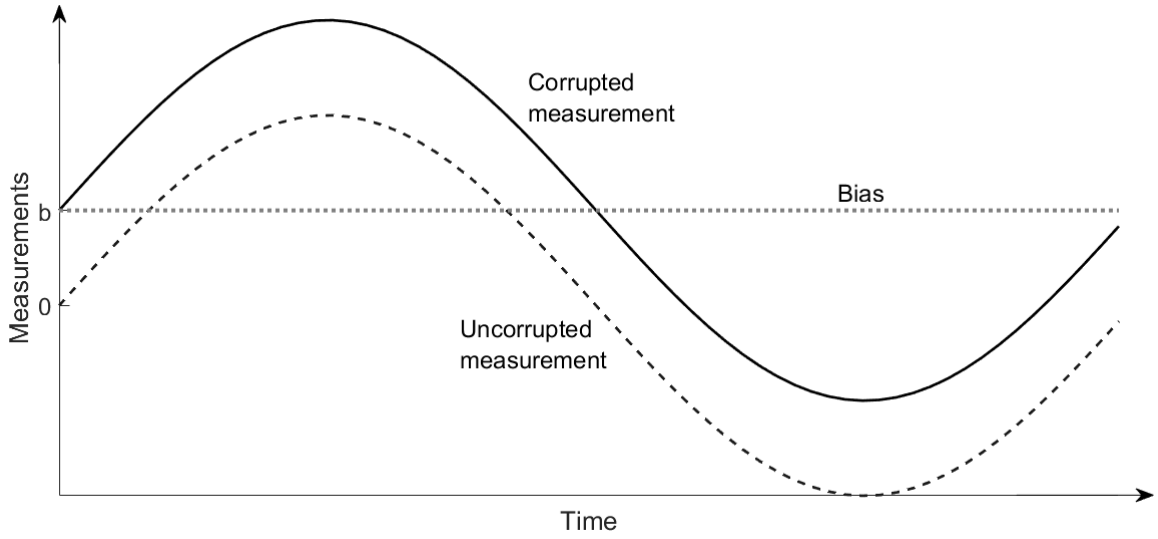

Source: Author

2.1.3.2 Scale Factors

Scale factors, denoted here by s_x, s_y and s_z, also manifest both in accelerometers and gyroscopes; they corrupt the measurements by multiplying them by a parameter. Therefore, the error caused by a scale factor is proportional to the sensor measurement. Figure 2.11 illustrates the effect of a constant scale factor s acting upon a sinusoidal shaped measurement. Observing the gray area, representing the error over time, we can notice the linear relation (caused by a constant scale factor) between the corrupted and uncorrupted measurements. Therefore, the sensor's output can be calibrated by a simple division; the challenge, then, becomes estimating these error parameters, as discussed in Chapter 3.

Figure 2.11 – Effect of scale factor on sensor measurements

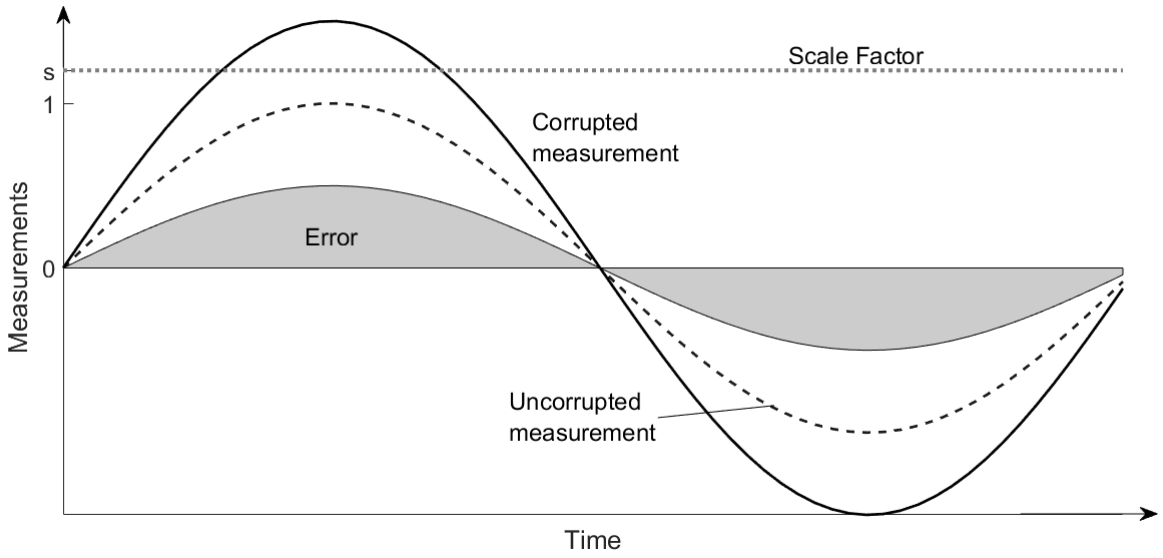

Source: Author

2.1.3.3 Cross-Coupling Errors

Cross-coupling errors, also referred to as misalignments, occur when the sensitive axes of the sensors are not orthogonally aligned; thus, they become sensitive to each other's acceleration or angular rate. For instance, if the *y*-axis accelerometer is misaligned towards the *x*-axis (Figure 2.12), measurements of the former will be corrupted by specific forces applied to the latter.

Figure 2.12 – Misalignment in one axis

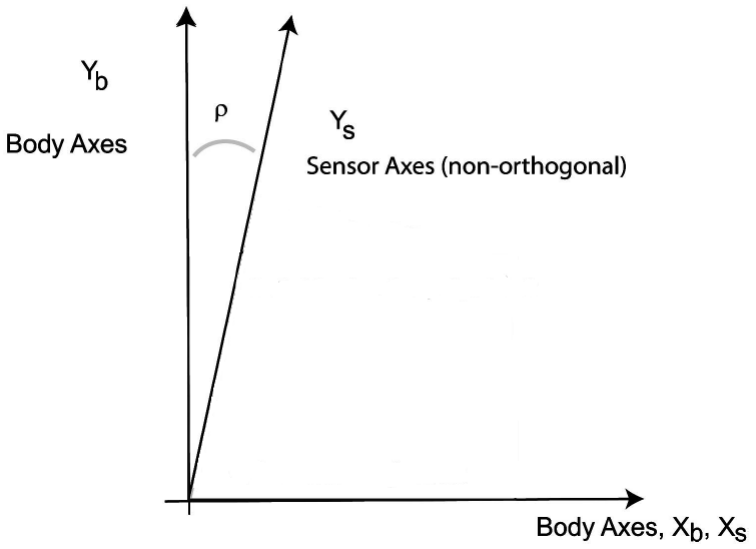

Source: (FOSTER; ELKAIM, 2008)

In the three-dimensional case, the misalignments appear as in Figure 2.13, where ρ is defined as the angle between the y body and sensitive axes, ϕ is the error from z-sensor to x-z plane of the body frame, and λ, from z-sensor to y-z plane of the body frame.

Figure 2.13 – Misalignments in a triaxial sensor.

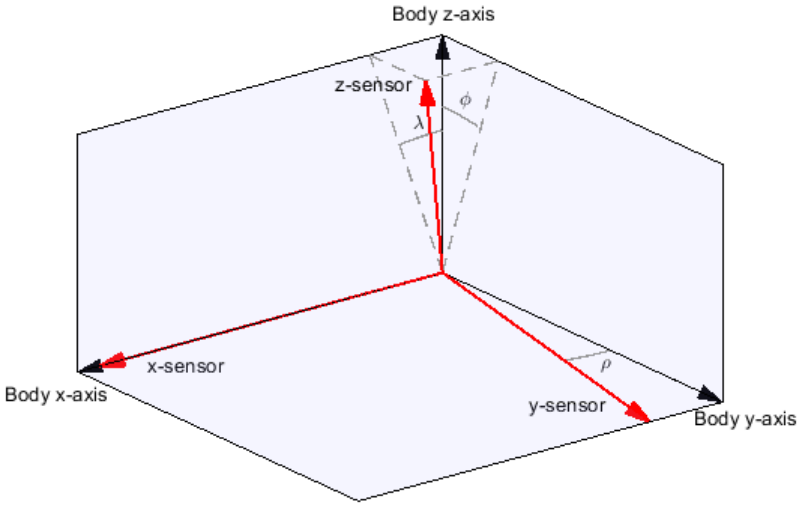

Source: Author

Considering the three aforementioned sources of error (bias, scale-factor and cross-coupling), one could model the specific force accelerations measured by the triaxial accelerometer of Figure 2.13 as follows:

$$\tilde{f}_x = s_x f_x + b_x \tag{2.1}$$

$$\tilde{f}_y = s_y[f_y \cos(\rho) + f_x \sin(\rho)] + b_y, \tag{2.2}$$

$$\tilde{f}_z = s_z[f_z \cos(\phi)\cos(\lambda) + f_x \sin(\phi)\cos(\lambda) + f_y \sin(\lambda)] + b_z \tag{2.3}$$

where $\tilde{f}_x$, $\tilde{f}_y$, and $\tilde{f}_z$ are the measured specific force accelerations at x, y and z-axes of the sensor frame, and f_x, f_y and f_z the uncorrupted counterparts at x, y and z-axes of the body frame, respectively. Notice that, because the x- body and sensor axes are, by definition, coincident, there is no cross-coupling error between them. The same model is assumed here for gyros.

2.1.3.4 Other Sources of Error

Besides the three aforementioned systematic contributions, additional errors can arise from further sources. Firstly, *random noise* manifests in every inertial sensor, contributing differently depending on the sensor design. As examples, we may cite: electrical noise (affects especially MEMS), noise due to mechanical instabilities (pendulous accelerometers and spinning-mass gyros), RLG residual lock-in effect and high frequency resonances (vibrating-beam accelerometers and vibratory gyros), etc.. Random noise on specific force and angular rate measurements, when integrated into velocity and attitude, respectively, produce a stochastic error process called random-walk. Furthermore, quantization (necessary in any digital computer) inherently causes error, which varies according to the Analog-to-Digital (A/D) converter resolution. Spinning-mass and vibratory gyros also present additional acceleration-dependent biases, named g-dependent biases. Nonlinearity along the sensor range also occurs to a certain level, depending on design characteristics. Finally, spinning-mass gyros and pendulous accelerometers also suffer from other higher-order errors (GROVES, 2013). Among the mentioned additional error sources, only random noises, assumed here to be white and Gaussian, are considered in the inertial sensor error model hereinafter, where only accelerometers will be addressed.

2.1.3.5 Complete Error Model

Accounting for the four aforementioned error sources, the complete error model, described for accelerometers, but also applicable for gyros, is written as follows (GROVES, 2013):

$$\tilde{\boldsymbol{f}} = C_s C_m \boldsymbol{f} + \boldsymbol{c}_b + \boldsymbol{c}_\mu, \tag{2.4}$$

where $\tilde{\boldsymbol{f}}$ and $\boldsymbol{f}$ are 3×1 vectors that contain the measured and uncorrupted specific force measurements in the sensor frame, respectively; C_m is a lower triangular matrix whose entries are functions of ρ, ϕ and λ, as displayed in (2.5); C_s is a diagonal matrix whose elements are the scale factors of each axis, as displayed in (2.6); $\boldsymbol{c}_b$ and $\boldsymbol{c}_\mu$ are 3×1 vectors containing the biases and random noises affecting each sensor, as displayed in (2.7) and (2.8), respectively.

$$C_m = \begin{bmatrix} 1 & 0 & 0 \\ \sin(\rho) & \cos(\rho) & 0 \\ \sin(\phi)\cos(\lambda) & \sin(\lambda) & \cos(\phi)\cos(\lambda) \end{bmatrix} \tag{2.5}$$

$$C_s = \begin{bmatrix} s_x & 0 & 0 \\ 0 & s_y & 0 \\ 0 & 0 & s_z \end{bmatrix} \tag{2.6}$$

$$\boldsymbol{c}_b = \begin{bmatrix} b_x \\ b_y \\ b_z \end{bmatrix} \tag{2.7}$$

$$\boldsymbol{c}_\mu = \begin{bmatrix} \mu_x \\ \mu_y \\ \mu_z \end{bmatrix} \tag{2.8}$$

Notice that we represent C_m as a 3×3 lower triangular matrix (2.5) and C_s as a 3×3 positive diagonal matrix (2.6). Therefore, $C_s C_m$ is also a lower triangular matrix. However, the format of $C_s C_m$ could have been different, if C_m had been defined, for instance, as a fully populated 3×3 matrix (as preferred by some authors). Nevertheless, conversion between these different formats is always possible, so, in this work, the simplifying assumption of C_m being a lower triangular matrix is preferred, as defined by Foster and Elkaim (2008).

2.2 Attitude and Heading Reference System

An Attitude and Heading Reference System (AHRS) comprises an IMU (tactical or lower grade) plus a triaxial magnetometer (covered in more details in Section 2.2.1) (FARRELL, 2008). This device provides attitude based on the combination of these sensors, which can be obtained by integration via Kalman Filter, for example. Figure 2.14 presents a block diagram of an AHRS, where the attitude solution is computed after processing data from the three blocks representing the gyroscope, magnetometer, and accelerometer triads.

AHRSs are mainly used as a source of attitude for UAVs, small aircrafts and other low-cost aviation applications. As the goal of this study is to analyze and implement calibration techniques for AHRSs, the next two sections (2.2.1 and 2.2.2) will discuss the most relevant topics relative to magnetometers and their error characteristics.

Figure 2.14 – Block diagram of a basic AHRS

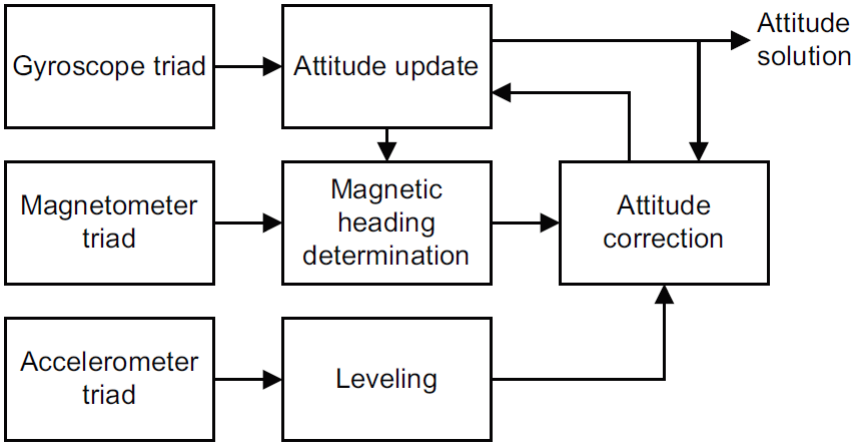

Source: (GROVES, 2013)

2.2.1 Magnetometers

Earth's magnetic field has been a navigation reference for thousands of years. One of the first techniques consisted of placing a plate containing a magnetic lodestone into a water container for leveling; then, the floating plate would rotate according to Earth's magnetic field, providing heading (RENAUDIN; AFZAL; LACHAPELLE, 2010). Floating-needle magnetic compass is another traditional technology for heading reference. Nowadays, with the advent of digital computers, magnetometers offer digital measurements of Earth's magnetic field, which can be used for calculating attitude, particularly with the aid of models like the International Geomagnetic Reference Field (IGRF) and the World Magnetic Model (WMM).

Four types of magnetometers are suitable for navigation: fluxgates, Hall-effect sensors, magnetoinductive sensors, and magnetoresistive sensors (GROVES, 2013). Langley (2003) described each of these designs. The fluxgate magnetometer was invented in the 1930s by Victor Vacquier. It is basically a transformer whose coils are submitted to an alternating current, producing a varying magnetic field; whenever there is an external magnetic field acting upon the sensor, it interferes on the alternating one, which can be measured and computed into magnetic field density. Although a good accuracy is provided, they are larger and more expensive sensors. In 1879, Edwin Hall "...discovered that if a current is passed lengthwise through a thin conductor in the presence of a magnetic field, a small voltage develops across the width of the conductor." (LANGLEY, 2003, p. 74). This discovery led to the development of many devices for magnetic field measurement, whose construction was relatively simple, although their performance was inferior. A magnetoinductive magnetometer was first patented in 1989. This

sensor works by measuring, through the frequency of an oscillator, the variation of inductance in a coil submitted to a magnetic field. Lastly, magnetoresistive sensors comprise a resistor, first described by William Thompson, a.k.a. Lord Kelvin, in 1856, sensitive to magnetic fields; it is usually mounted as a Wheatstone bridge, so the variation in resistance can be measured as voltage (Figure 2.15). The two aforementioned sensors, which are small, provide measurements accurate enough for most navigation applications (GROVES, 2013).

Figure 2.15 – Wheatstone bridge of magnetoresistive sensors

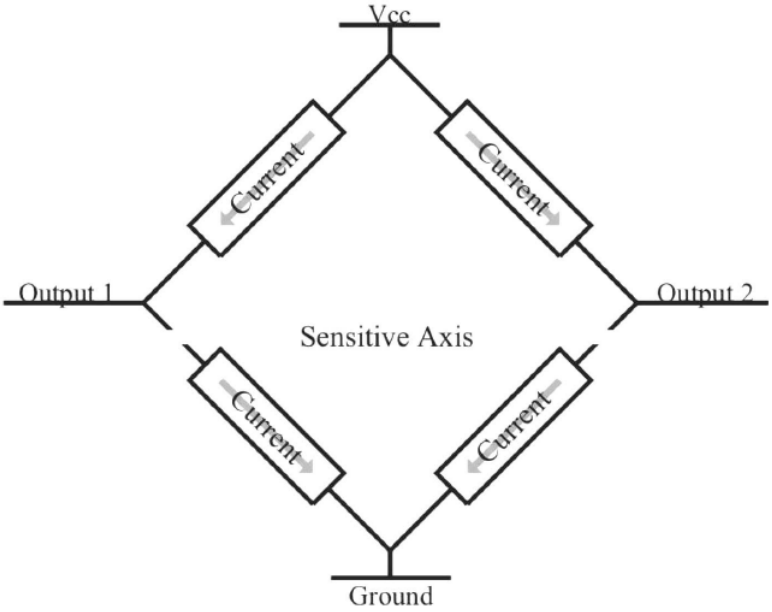

Source: (FOSTER; ELKAIM, 2008)

2.2.2 Error Characteristics

Magnetometers present the same types of error described in Section 2.1.3 for accelerometers and gyroscopes in addition to *hard iron* and *soft iron* errors, denoted here by *hi* and *si*, respectively. Foster and Elkaim (2008) described the last two as side effects of measuring magnetic fields, where hard iron interferences are caused by the permanent magnetization of materials in the vicinity of the sensor, while soft iron effects occur due to variable magnetic permeability, which enables inducted magnetic fields to arise. Even though hard iron has its own causes, it manifests in the same way as regular sensor bias and is constant. Therefore, they are often mathematically represented together as one single bias parameter. Since soft iron errors are induced by external magnetic fields, and they are proportional to the magnitude of these fields, their effects manifest in the same way as scale factors and misalignments. Thus, if a linear relation can be assumed between the intensity of the magnetic field and the soft iron error, it can

be modeled as regular scale factor and misalignments. In short, hard iron and soft iron errors are often modeled as part of biases, and scale factors and misalignments, respectively. Therefore, magnetometers reading are modeled here with the same parameters as accelerometers, as follows.

$$\tilde{\boldsymbol{m}} = C_s C_m \boldsymbol{m} + \boldsymbol{c}_b + \boldsymbol{c}_\mu, \tag{2.9}$$

where $\tilde{m}$ is the measured magnetic field density in the sensor frame, and m is the real magnetic field density in the sensor frame.

After the systematic parameters are estimated, one may correct the corrupted measurements using [1]:

$$\hat{\boldsymbol{m}} = \hat{C}_m^{-1} \hat{C}_s^{-1} (\tilde{\boldsymbol{m}} - \hat{\boldsymbol{c}}_b), \tag{2.10}$$

where $\hat{}$ indicates estimated variables.

[1] The same formulation can be used for accelerometers.

3 CONVENTIONAL CALIBRATION METHODS

As stated in Chapter 1, the aim of this study is to provide a comparison between the most relevant calibration algorithms for accelerometers, gyroscopes and magnetometers. Thus, this chapter presents a general description of some of the most relevant calibration methods available in the literature. By calibration, we should understand the ensemble of techniques devoted to identify the systematic errors sources addressed in Chapter 2, and to compensate them in the sensor readings. As shown by Särkkä et al. (2017), there are numerous approaches for calibration: some can only be performed for a single kind of sensor (i.e., either accelerometers, gyros or magnetometers); while other are capable of calibrating two or even all three of them simultaneously. Therefore, Section 3.1 focuses on calibration techniques used for accelerometers, gyros and magnetometers individually, following then on methods used for multiple sensors.

3.1 Accelerometer Calibration

One of the most referred calibration techniques for accelerometers has been presented by Lötters et al. (1998) for medical applications. This method estimates the biases and scale factors (referred to as offsets and sensitivities, respectively) of a triaxial accelerometer, which results in output values with mean errors of less than 3%. As the procedure is intended to be performed automatically in-field, no specific sensor positions or orientations are required; instead, quasi-static random movements (producing not detectable centripetal force) must be applied to the sensors in order to collect the data so that the module of the three outputs equals the local gravity acceleration (in error free conditions):

$$\sqrt{f_x^2 + f_y^2 + f_z^2} = g \tag{3.1}$$

where g is the local gravity acceleration. However, considering the actual measurements corrupted by biases and scale factors, (3.1) becomes (cross-coupling errors have not been considered by (LÖTTERS et al., 1998)):

$$\sqrt{\left(\frac{\tilde{f}_x - b_x}{s_x}\right)^2 + \left(\frac{\tilde{f}_y - b_y}{s_y}\right)^2 + \left(\frac{\tilde{f}_z - b_z}{s_z}\right)^2} = g \tag{3.2}$$

If a perfectly calibrated triaxial accelerometer is submitted to quasi-static movements, the total compilation of the output module draws a perfect sphere with center at the origin; by

contrast, the raw measurements (with errors) produce an ellipsoid with center moved away from the origin (Figure 3.1). Consequently, taking the ideal sphere as a reference, the method uses a linear estimator to compute the bias and scale factor.

Figure 3.1 – Distortion caused by the errors on accelerometer measurements.

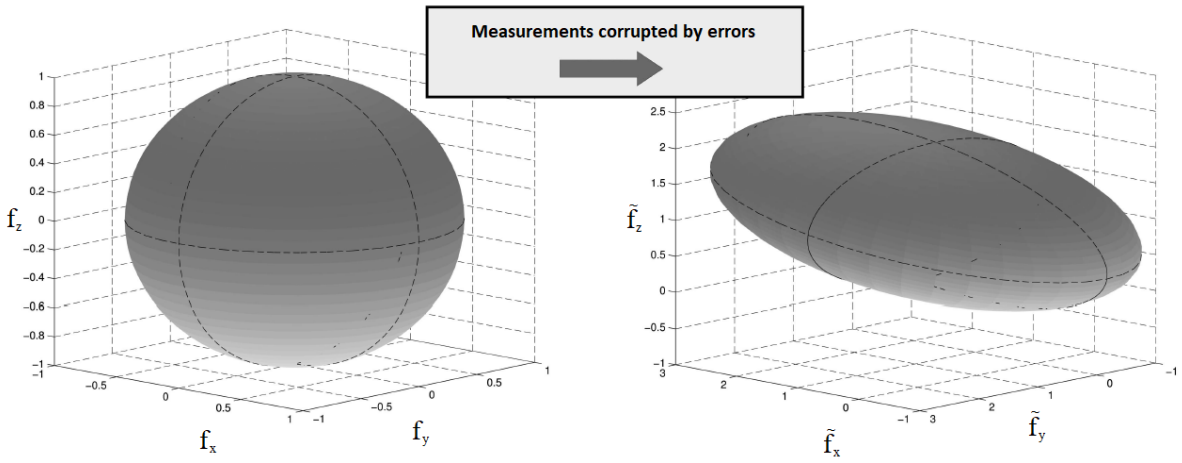

Source: Adapted from (VASCONCELOS et al., 2011)

Lötters et al. (1998) referred to some previous approaches for accelerometer calibration as "laboratory oriented techniques", such as (ESTRICH; RANGAN, 1989) and (MARIOLI; SARDINI; TARONI, 1993), in the sense that these methods can only be performed with aid of laboratory equipment, which limits practical implementations. Alternatively, the so-called "in-field calibration techniques" have been proposed (GREWAL; HENDERSON; MIYASAKO, 1991) and (BARSHAN; DURRANT-WHYTE, 1995). Although they do not rely on laboratory procedures, they still require measurements from other sources - such as gyros - to provide orientation or position reference for calibration.

Afterwards, Wu, Wang and Ge (2002) adapted the calibration method presented by Lötters et al. (1998) for acceleration measurement in elevators. However, instead of using a predictor to estimate whether the sensor was under quasi-static conditions, this information was directly attainable from the control system, which figured as a relevant benefit. Following the same initial concepts, Krohn et al. (2004) improved the technique by also considering intrinsic the non-orthogonalities (cross-coupling errors) of most sensors commercially available – particularly the inexpensive ones.

Techniques based on similar ideas have been reported in the literature; even though they vary considerably in performance. For instance, Frosio, Pedersini and Borghese (2009) proposed a new method whose working principle relies on the same fact that the module of a

triaxial accelerometer equals 1g in static conditions. However, in contrast to (LÖTTERS et al., 1998), (WU; WANG; GE, 2002), (ESTRICH; RANGAN, 1989), (MARIOLI; SARDINI; TARONI, 1993), (GREWAL; HENDERSON; MIYASAKO, 1991), and (BARSHAN; DURRANT-WHYTE, 1995), this approach estimates, in addition to the biases and scale factors, the misalignments between the sensor axes, which, as stated in Section 2.1.3.3, need to be accounted for in order to guarantee the reliability of the measurements. Moreover, this procedure requires the triaxial accelerometer to perform only nine random rotations; and, parameters are estimated using Newton's method for optimization. It provides an improved accuracy, of about one order of magnitude compared to past works (WU; WANG; GE, 2002). In the paper by Won and Golnaraghi (2009), the authors proposed another enhanced approach; in contrast to preceding methods, it used an iterative algorithm for computing the error parameters, in this case, only biases and scale factors.

More recently, Forsberg, Grip and Sabourova (2013) presented a non-iterative method for accelerometer calibration. The working principle, similar to most of the aforementioned techniques, is based on measurements of the Earth gravity vector in different positions; requiring however, the sensor to be placed into, at least, nine different orientations. Alike Frosio, Pedersini and Borghese (2009) and Krohn et al. (2004), this approach computes biases, scale factors and misalignments.

As pointed by Glueck et al. (2014), an issue in most of the procedures based on gravity measurements is that these algorithms have to deal with nonlinear optimization problems, which brings shortcomings. For instance, Frosio, Pedersini and Borghese (2009) and Krohn et al. (2004) express the calibration in terms of a first or second-order Taylor series. This approach is usually solved by the Newton or adapted-Newton algorithm, which inherently creates a local convergence issue that demands proper initial values for convergence. Another conventional way to handle the problem, via analytical linearization-based parameter estimation, is described by Lötters et al. (1998), which however, does not solve the aforementioned convergence issue. To solve this drawback, a statistical linearization, implemented through an Unscented Kalman Filter (UKF) can be adopted (GLUECK; BUHMANN; MANOLI, 2012). Despite overcoming the problem, this approach only estimates six parameters: three biases and three scale factors.

3.2 Magnetometer Calibration

Regarding magnetometer calibration, one of the most classic approaches is called compass swinging, originally proposed by Bowditch (1995). This technique requires the magnetic sensor to be rotated around each axis, while measurements are acquired. In this case, an external source of orientation is required in order to provide the reference needed for the subsequent non-linear parameter estimation. However, as stated by Alonso and Shuster (2002a), the need for an external source of attitude is a major drawback, since the magnetometers are often the only source of orientation available. Therefore, in order to overcome the attitude-dependence issue, Alonso and Shuster (2002a) presented a new technique called TWOSTEP, which was an extension of the work by Gambhir (1975). As the name implies, this approach has two stages: (a) a so-called "centering technique"is used to estimate the biases; (b) the estimated values are used as initial conditions for the Gauss-Newton method, which runs until the minimization reaches a predetermined desired threshold. Although this method is attitude-independent, it only estimates biases, which is a significant shortcoming. Nevertheless, Alonso and Shuster (2002b) presented an extension of their own method that was also able to estimate scale factors and misalignments regardless of attitude, in contrast to common wisdom. This methodology is fully mathematically described in Section 3.4.1 and implemented in Chapter 5.

In 2005, Crassidis, Lai and Harman (2005) presented a relevant improvement to the work by Alonso and Shuster (2002b) for real-time implementation; three approaches were tested and analyzed: the first was based on the centering approximation, the second was derived using an Extended Kalman Filter (EKF), and the third employed an Unscented Filter (UF). Simulations and real data tests showed that the last two approaches are considerably superior to the first one, providing better calibration.

Gebre-Egziabher et al. (2006) also pointed some issues involving compass swinging: (a) as previously mentioned, compass swinging is attitude-dependent; (b) the sensor must be horizontally leveled during calibration; (c) the procedure is location dependent, that is, the accuracy degrades as the sensor is moved away. In order to tackle these issues, the authors presented a new calibration method performed in the magnetic field domain. The procedure is very similar to the scaling check presented by Lötters et al. (1998) for accelerometer calibration. However, instead of taking the local gravity vector as a reference, this approach uses the local Earth magnetic field density vector (Equation 3.3), which is available with high accuracy via models like the IGRF and WMM.

$$\sqrt{m_x^2 + m_y^2 + m_z^2} = m_t \tag{3.3}$$

where m_x, m_y and m_z are the uncorrupted magnetic field density components at each axis: x, y and z, respectively; and m_t is the magnitude of the local Earth magnetic density.

In Gebre-Egziabher's approach, a linearized iterative batch least squares is the parameter estimator, initialized by a non-linear two-step estimator (shall not be confused with Alonso and Shuster's TWOSTEP estimator, referred to in this work, with capital letters). Despite the improvements, this method does not account for misalignments between the sensors axes. This shortcoming was handled by Foster and Elkaim (2008), who successfully included these parameters in their calibration algorithm (herein called "Extended Two-Step"(ETS)), which is mathematically described in Section 3.4.2 and implemented in Chapters 4 and 5. Springmann and Cutler (2012) improved the work by Foster and Elkaim (2008) by including a time-varying bias component into the calibration parameters. Destined to small satellite applications, this method models the time-varying (in-run) biases by considering telemetered currents from the spacecraft circuits, which produces magnetic interferences. Another improvement to the work by Gebre-Egziabher et al. (2006) came from the study presented by Renaudin, Afzal and Lachapelle (2010), which considered, in addition to biases, scale factors and misalignments, the effects of spatially-varying magnetic perturbations (soft iron errors).

Vasconcelos et al. (2011) claimed to have further improved the preceding methods by presenting an algorithm based on a Maximum Likelihood Estimation (MLE). This calibration methodology is mathematically described in Section 3.4.3 and implemented in Chapter 5. There are additional improvements to this method in the literature, but they will be discussed in Section 3.3, since their algorithms are able to handle multiple sensors.

Besides the aforementioned magnetometer calibration techniques, other procedures have been proposed. Kayton and Fried (1997), for instance, presented a solution for the inconvenient motions required in most calibration algorithms; in their approach, a device produces an artificial magnetic field that submits the sensor to various known scenarios. However, a major drawback is the need for extra equipment on-board. Wang and Gao (2005) introduced a different solution for the ellipsoid fitting problem: they used an Artificial Neural Network (ANN) in order to map the relation between the corrupted measurements and the ideal output values. Pang et al. (2013) presented another attitude-independent approach, also based on scaling calibration. This method, which relies on a differential evolution algorithm, presented better calibration

performance and robustness compared to methods derived from UKF, Genetic Algorithm (GA) and Recursive Least-Squares (RLS). In order to deal with the local minima convergence issue, a problem faced by many optimization-based calibration methods, Wu et al. (2012) presented a stochastic-based algorithm named Stretching Particle Swarm Optimization. In the same year, Wu et al. (2013) proposed a methodology based on a Constrained Total Least-Squares (CTLS), which is described in details in Section 3.4.4 and implemented in Chapter 5. Other methodologies have been proposed in the following years. We call attention to the optimal MLE-based methodology described in (WU; SHI, 2015), which is also fully mathematically described in Section 3.4.5 and implemented in Chapter 5.

In addition, some national studies have addressed the topic of magnetometer calibration. Hemerly and Coelho (2014) present the procedure as an ellipsoid fitting problem, solved via a constrained least squares. Furthermore, Mucciaccia, Frizera and Salles (2016) proposed a similar method, also described as a ellipsoid fitting solved via least squares, but with a direct solution based on algebraic distance.

3.3 Calibration of Multiple Sensors

The calibration algorithms available in the literature are often adapted for multiple sensors, which is absolutely convenient for practical implementations. From Sections 3.1 and 3.2, it is possible to notice consistent similarities between the calibration techniques for accelerometers and magnetometers, especially those based on the ellipsoid fitting idea. As mentioned in Section 3.2, Foster and Elkaim (2008) implemented a technique for magnetometer calibration; however, they also suggested that the procedure could be adapted for accelerometers, even though no tests were performed for this purpose.

Renk et al. (2005) presented a calibration algorithm for accelerometers and magnetometers that estimates biases, scale factors and non-orthogonality between the sensors, through a least squares problem, solved after they are rotated (quasi-statically, for the accelerometers) using a robotic arm. Even though this method provides reasonably accurate calibration, it depends on a robotic actuator, which precludes in-field application; in addition, misalignments between each sensor axis are not taken into account. Furthermore, Zhu and Zhou (2006) proposed another laboratory calibration technique that complements the work by Renk et al. (2005), by estimating misalignments within each triaxial sensor. The procedure is based on an optical analysis of the misalignments, followed by a least squares estimation of the calibration para-

meters. Following, Včelák et al. (2005) presented a method that accounts for the contributions by both Renk et al. (2005) and Zhu and Zhou (2006). Biases, scale factors and misalignments are estimated through a scalar calibration algorithm. In the latter, the sensors are positioned in random orientations, while a novel two-step method estimates the non-orthogonality between the magnetometers and accelerometers, with the aid of a laboratory non-magnetic calibration device. In addition, the authors suggest that the technique can be used for any kind of triaxial sensor.

Jurman et al. (2007) considered, in addition to magnetometers and accelerometers, the calibration of gyroscopes. The first two had the calibration parameters estimated via a constrained Newton optimization, using data obtained while the sensors were moved through different orientations; the latter was submitted to a more sophisticated procedure that required known constant angular rates, produced by a laboratory device. For each case, biases, scale factors and misalignments were estimated.

Bonnet et al. (2009) presented a new algorithm for in-field calibration of accelerometers and magnetometers, considering biases, scale factors and misalignments. Basically, the sensors must be rotated into different positions; then, the parameters are estimated via a Minimum-Volume Enclosing Ellipsoid (MVEE) algorithm, which performs more effectively as the measurements are better distributed around the ellipsoid.

Taking the work by Vasconcelos et al. (2011) as a benchmark, Xiaoming et al. (2014) extended their work by calibrating not only biases, scale factors and misalignments, but also estimating mounting errors between magnetometer and other sensors (usually an IMU). Zhang and Yang (2014) presented an algorithm based on least squares ellipsoid fitting that, in addition to what Xiaoming's approach comprises, performs gyroscope calibration. Lastly, Särkkä et al. (2017) provided one of the most comprehensive methodologies so far, which estimates the usual calibration parameters for each sensor (in the same frame), and can be performed in-field with fairly simple tools (a cube and a jig). Another comprehensive methodology, based on an iterative algorithm initialized with a least squares, was presented by Papafotis and Sotiriadis (2019); although variations for accelerometers, gyroscopes and magnetometers are presented, only the last one is mathematically described in Section 3.4.6 and implemented in Chapter 5.

3.4 Mathematical Description of the Implemented Methods

In this section, six main calibration methods reviewed in Sections 3.1 to 3.3 and implemented in Chapters 4 and 5 are mathematically described. The choice for these techniques was based on practicality for in-field use, effectiveness, and relevance amongst its pairs. As magnetometers are traditionally known to require more frequent in-field calibrations (due to the effects of hard and soft iron magnetisms) in comparison to inertial sensors, we also prioritized the selection/description of magnetometer calibration algorithms. As will be discussed in Chapter 6, some of them can, and will, be adapted for inertial sensor (accelerometer, in particular) calibration.

Notice also that each algorithm presents its own variable definitions. In order to maintain a pattern throughout this work, and also to preserve the original variables of each method, we define two sets of variables called *inputs* and *outputs* according to Chapter 2, and relate them with the ones used at the calibration methods. Therefore, besides the variables classified as *inputs* or *outputs*, the ones presented in each mathematical description are only valid for that specific method. They are referred to here as *local variables*, and shall not be confused with the ones used regularly, called *global variables*.

3.4.1 TWOSTEP Method

The first calibration method described here, referred to as TWOSTEP, was introduced by Alonso and Shuster (2002a) and expanded by Alonso and Shuster (2002b). In addition, Dinale (2013) implemented and comprehensively described the TWOSTEP technique. For this reason, we follow Dinale's description of TWOSTEP, presenting it in 12 steps focused on implementation. The code used throughout this work to implement the TWOSTEP method is available in the work by Dinale (2013).

Before going through the implementation steps, it is necessary to introduce the error model adopted in the TWOSTEP method, which significantly differs from that presented in Chapter 2. The error model is defined as follows:

$$\boldsymbol{B}_k = (I+D)^{-1}(\vartheta^T A_k \boldsymbol{H}_k + \boldsymbol{b} + \varepsilon_k) \tag{3.4}$$

where $\boldsymbol{B}_k$ is the k^{th} sample of the triaxial magnetometer; I is an identity matrix; D is a fully populated symmetric matrix that comprehends scale factor errors and misalignments; A_k and

ϑ are two rotation matrices used to convert $\boldsymbol{H}_k$, the true magnetic field density vector resolved in Earth-Centered-Earth-Fixed (ECEF) coordinates, to body frame and to sensor frame, respectively; $\boldsymbol{b}$ is the bias vector; and ε_k is the measurement noise vector.

However, the model of (3.4) must be adapted, since A_k and ϑ^T are not estimated, and $|\boldsymbol{H}_k|$ is known via magnetic models, yielding:

$$|\boldsymbol{H}_k|^2 = [(I+D)\boldsymbol{B}_k - \boldsymbol{b} - \varepsilon_k]^T[(I+D)\boldsymbol{B}_k - \boldsymbol{b} - \varepsilon_k] \tag{3.5}$$

which is further manipulated into:

$$|\boldsymbol{H}_k|^2 = |\boldsymbol{B}_k|^2 + \boldsymbol{B}_k^T E\boldsymbol{B}_k - 2\boldsymbol{B}_k^T\boldsymbol{c} - \nu_k + |\boldsymbol{b}|^2 \tag{3.6}$$

where E and $\boldsymbol{c}$ are included in order to eliminate nonlinearities related to D, and ν_k is the new measurement noise. They are defined as follows:

$$E = 2D + D^2 \tag{3.7}$$

$$\boldsymbol{c} = (I+D)\boldsymbol{b} \tag{3.8}$$

$$\nu_k = 2[(I+D)\boldsymbol{B}_k - \boldsymbol{b}]\varepsilon_k - |\varepsilon_k|^2 \tag{3.9}$$

In addition, a scalar measurement z_k is introduced:

$$z_k = |\boldsymbol{B}_k|^2 - |\boldsymbol{H}_k|^2 \tag{3.10}$$

which becomes:

$$z_k = -\boldsymbol{B}_k^T E\boldsymbol{B}_k + 2\boldsymbol{B}_k^T\boldsymbol{c} + \nu_k - |\boldsymbol{b}|^2 \tag{3.11}$$

In practice, z_k represents the scalar error between the measured and expected total magnetic field density.

In order to simplify the implementation, z_k can be recast as:

$$z_k = \boldsymbol{L}_k\boldsymbol{\theta}' - |\boldsymbol{b}|^2 + \nu_k \tag{3.12}$$

where

$$\boldsymbol{L}_k = (2\boldsymbol{B}_k^T - \boldsymbol{K}_k) \tag{3.13}$$

where

$$\boldsymbol{K}_k = \begin{bmatrix} B_{1k}^2 & B_{2k}^2 & B_{3k}^2 & 2B_{1k}B_{2k} & 2B_{1k}B_{3k} & 2B_{2k}B_{3k} \end{bmatrix} \tag{3.14}$$

and

$$\boldsymbol{\theta}' = \begin{bmatrix} \boldsymbol{c} \\ E_{11} \\ E_{22} \\ E_{33} \\ E_{12} \\ E_{13} \\ E_{23} \end{bmatrix} \tag{3.15}$$

Lastly, the noise v_k must be characterized. It is considered a white Gaussian noise, such that $v_k \sim \mathcal{N}(\mu_k, \sigma_k^2)$. Its mean and variance are calculated as follows:

$$\mu_k = -tr(\Sigma_k) \tag{3.16}$$

$$\sigma_k^2 = 4[(I+D)\boldsymbol{B}_k - \boldsymbol{b}]^T \Sigma_k [(I+D)\boldsymbol{B}_k - \boldsymbol{b}] + 2tr(\Sigma_k^2) \tag{3.17}$$

where Σ_k is the covariance matrix of the measurement noise ε_k.

The step-by-step implementation of TWOSTEP is given as follows. Given the known inputs $|\boldsymbol{H}_k|$, $\boldsymbol{B}_k$ and Σ_k, then:

- Calculate the noise mean μ_k via (3.16).
- Calculate z_k via (3.10).
- Calculate $\boldsymbol{L}_k$ via (3.13).
- Calculate σ_k^2 via (3.17), where the initial estimates for $\boldsymbol{b}$ and D are zero.
- Calculate centre components $\bar{\sigma}^2$, $\bar{\boldsymbol{B}}$, $\bar{z}$, $\bar{\boldsymbol{L}}$ and $\bar{\mu}$, over the whole data length (N):

$$\bar{\sigma}^2 = \left(\sum_{k=1}^{N} \frac{1}{\sigma_k^2} \right)^{-1} \tag{3.18}$$

$$\bar{\boldsymbol{B}} = \bar{\sigma}^2 \sum_{k=1}^{N} \frac{1}{\sigma_k^2} \boldsymbol{B}_k \tag{3.19}$$

$$\bar{z} = \bar{\sigma}^2 \sum_{k=1}^{N} \frac{1}{\sigma_k^2} z_k \tag{3.20}$$

$$\bar{\boldsymbol{L}} = \bar{\sigma}^2 \sum_{k=1}^{N} \frac{1}{\sigma_k^2} \boldsymbol{L}_k \tag{3.21}$$

$$\bar{\mu} = \bar{\sigma}^2 \sum_{k=1}^{N} \frac{1}{\sigma_k^2} \mu_k \tag{3.22}$$

- Calculate centred components $\tilde{B}_k$, $\tilde{z}_k$, $\tilde{L}_k$ and $\tilde{\mu}_k$:

$$\tilde{\boldsymbol{B}}_k = \boldsymbol{B}_k - \bar{\boldsymbol{B}} \qquad \tilde{z}_k = z_k - \bar{z} \qquad \tilde{\boldsymbol{L}}_k = \boldsymbol{L}_k - \bar{\boldsymbol{L}} \qquad \tilde{\mu}_k = \mu_k - \bar{\mu} \tag{3.23}$$

- Calculate centred Fisher Information Matrix $\tilde{\mathscr{I}}(\theta')$:

$$\tilde{\mathscr{I}}(\boldsymbol{\theta}') = E\left\{ \frac{\partial^2 \tilde{J}(\boldsymbol{\theta}')}{\partial \boldsymbol{\theta}'^2} \right\} \tag{3.24}$$

  which is manipulated into:

$$\tilde{\mathscr{I}}(\boldsymbol{\theta}') = \sum_{k=1}^{N} \frac{1}{\sigma_k^2} \tilde{\boldsymbol{L}}_k^T \tilde{\boldsymbol{L}}_k \tag{3.25}$$

- Estimate $\tilde{\boldsymbol{\theta}}'^*$, where the asterisk indicates the value is an estimate:

$$\tilde{\boldsymbol{\theta}}'^* = [\tilde{\mathscr{I}}(\boldsymbol{\theta}')]^{-1} \sum_{k=1}^{N} \frac{1}{\sigma_k^2} (\tilde{z}_k - \tilde{\mu}_k) \tilde{\boldsymbol{L}}_k^T \tag{3.26}$$

- Calculate log likelihood gradients:

$$\frac{\partial}{\partial \boldsymbol{\theta}'} \tilde{J} = \sum_{k=1}^{N} \frac{-1}{\sigma_k^2} (\tilde{z}_k - \tilde{\mu}_k) \tilde{\boldsymbol{L}}_k^T + \tilde{\mathscr{I}}(\boldsymbol{\theta}') \boldsymbol{\theta}' \tag{3.27}$$

$$\frac{\partial}{\partial \boldsymbol{\theta}'} \bar{J} = -\frac{1}{\bar{\sigma}^2} \left(\bar{\boldsymbol{L}} \boldsymbol{\theta}' - \frac{\partial}{\partial \boldsymbol{\theta}'} |\boldsymbol{b}|^2 \right) \left(\bar{z} - \bar{\boldsymbol{L}} \boldsymbol{\theta}' + |\boldsymbol{b}|^2 - \bar{\mu} \right) \tag{3.28}$$

- Calculate centre Fisher Information Matrix $\bar{\mathscr{I}}(\boldsymbol{\theta}'^{*})$:

$$\bar{\mathscr{I}}(\boldsymbol{\theta}'^{*}) = \frac{1}{\bar{\sigma}^2}\left(\bar{\boldsymbol{L}} - \frac{\partial|\boldsymbol{b}|^2}{\partial\boldsymbol{\theta}'}\right)^T\left(\bar{\boldsymbol{L}} - \frac{\partial|\boldsymbol{b}|^2}{\partial\boldsymbol{\theta}'}\right) \tag{3.29}$$

- Iterate (3.30), updating $\bar{\mathscr{I}}(\boldsymbol{\theta}'^{*})$ at each iteration, until η_i reaches a desired value or i exceeds a maximum iteration number.

$$\boldsymbol{\theta}'_{i+1} = \boldsymbol{\theta}'_i - \mathscr{I}(\boldsymbol{\theta}'_i)^{-1}\frac{\partial}{\partial\boldsymbol{\theta}'}J(\boldsymbol{\theta}'_i) \tag{3.30}$$

$$\eta_i = (\boldsymbol{\theta}'_i - \boldsymbol{\theta}'_{i-1})^T\mathscr{I}(\boldsymbol{\theta}'_{i-1})(\boldsymbol{\theta}'_i - \boldsymbol{\theta}'_{i-1}) \tag{3.31}$$

- Recover desired values $\boldsymbol{b}$ and D.

  Firstly, we need to recover E and $\boldsymbol{c}$ via (3.15), where E is a symmetric 3x3 matrix, and $\boldsymbol{c}$ is a 3x1. Then, U, S and W must be calculated, where the first two are the E's eigenvalues and eigenvectors, respectively. The diagonal matrix W relates to S as:

$$S = 2W + W^2 \tag{3.32}$$

  Therefore, each element of W can be calculated as:

$$w_j = -1 + \sqrt{1 + s_j} \tag{3.33}$$

  Finally, we can calculate D and $\boldsymbol{b}$:

$$D^* = UWU^T \tag{3.34}$$

$$\boldsymbol{b}^* = (I + D^*)^{-1}\boldsymbol{c}^* \tag{3.35}$$

  The covariance matrix for $\boldsymbol{\theta}$, with $\boldsymbol{\theta} = [\ \boldsymbol{b}\quad \boldsymbol{D}\ ]^T$, where $\boldsymbol{D} =$ $[\ D_{1,1}\quad D_{2,2}\quad D_{3,3}\quad D_{1,2}\quad D_{1,3}\quad D_{2,3}\ ]^T$, is calculated as follows:

$$\mathscr{I}(\boldsymbol{\theta})^{-1} = \left(\frac{\partial(\boldsymbol{b},\boldsymbol{D})}{\partial(\boldsymbol{c},\boldsymbol{E})}\right) \mathscr{I}(\boldsymbol{\theta}')^{-1} \left(\frac{\partial(\boldsymbol{b},\boldsymbol{D})}{\partial(\boldsymbol{c},\boldsymbol{E})}\right)^{T} \tag{3.36}$$

where

$$\left(\frac{\partial(\boldsymbol{b},\boldsymbol{D})}{\partial(\boldsymbol{c},\boldsymbol{E})}\right) = \left(\frac{\partial(\boldsymbol{c},\boldsymbol{E})}{\partial(\boldsymbol{b},\boldsymbol{D})}\right)^{-1} \tag{3.37}$$

$$\left(\frac{\partial(\boldsymbol{b},\boldsymbol{D})}{\partial(\boldsymbol{c},\boldsymbol{E})}\right) = \begin{bmatrix} (I+D) & M_{\boldsymbol{cD}} \\ 0_{6\times 3} & 2I+M_{\boldsymbol{ED}} \end{bmatrix}, \tag{3.38}$$

$$M_{\boldsymbol{cD}} = \begin{bmatrix} b_1 & 0 & 0 & b_2 & b_3 & 0 \\ 0 & b_2 & 0 & b_1 & 0 & b_3 \\ 0 & 0 & b_3 & 0 & b_1 & b_2 \end{bmatrix}, \tag{3.39}$$

and

$$M_{\boldsymbol{ED}} = \begin{bmatrix} 2D_1 & 0 & 0 & 2D_4 & 2D_5 & 0 \\ 0 & 2D_2 & 0 & 2D_4 & 0 & 2D_6 \\ 0 & 0 & 2D_3 & 0 & 2D_5 & 2D_6 \\ D_4 & D_4 & 0 & D_1+D_2 & D_6 & D_5 \\ D_5 & 0 & D_5 & D_6 & D_1+D_3 & D_4 \\ 0 & D_6 & D_6 & D_5 & D_4 & D_2+D_3 \end{bmatrix} \tag{3.40}$$

Table 3.1 provides the relation between the input/output variables defined by Alonso and Shuster (2002b) and Dinale (2013), and the ones used interchangeably throughout this work, referred to here as global variables.

The individual misalignments and scale factors (outputs) in global format are derived as follows:

Table 3.1 – Input and output variables equivalency for the TWOSTEP method

Local variables	Global equivalent	Type (I/O)	Definition
$\boldsymbol{B}_k$	$\tilde{\boldsymbol{m}}$	I	Measured magnetic field density
$\lvert\boldsymbol{H}_k\rvert$	m_t	I	Earth's total local magnetic field density magnitude
$\sum_k$	$cov(c_\mu)$	I	Covariance matrix of the measurement noise
$(I+D)^{-1}\boldsymbol{b}$	$\boldsymbol{c}_b$	O	Biases
$(I+D)^{-1}$	$C_s C_m$	O	Misalignments and scale factors
ε_k	$\boldsymbol{c}_\mu$	N/A	Misalignments and scale factors

$$
\begin{aligned}
\rho &= \arctan\left(\frac{M'_{2,1}}{M'_{2,2}}\right) \\
\phi &= \arctan\left(\frac{M'_{3,1}}{M'_{3,3}}\right) \\
\lambda &= \arctan\left(\frac{M'_{3,2}}{M'_{3,1}}\right)\sin\phi \\
s_x &= M'_{1,1} \\
s_y &= \frac{M'_{2,1}}{\sin\rho} \\
s_z &= \frac{M'_{3,2}}{\sin\lambda}
\end{aligned}
\tag{3.41}
$$

where

$$
M = (I+D)^{-1} \tag{3.42}
$$

$$
M' = \begin{bmatrix} M_{1,1} & 0 & 0 \\ M_{2,1}+M_{1,2} & M_{2,2} & 0 \\ M_{3,1}+M_{1,3} & M_{3,2}+M_{2,3} & M_{3,3} \end{bmatrix} \tag{3.43}
$$

3.4.2 Extended Two-Step Method

The second method described here, the Extended Two-Step (ETS), developed by Foster and Elkaim (2008) as an extension of the work by Gebre-Egziabher et al. (2006), where misalignments are not estimated, can be used both for two- or three-axial magnetometers. Since

there are applications for 2D compasses, such as in maritime navigation, both cases will be presented, starting with the simplest.

3.4.2.1 Two-dimensional Calibration

The two-dimensional ETS technique (shall not be confused with TWOSTEP) is based on the idea that a pair of leveled, uncorrupted magnetometers rotated about the z-axis would produce outputs that, if plotted together, would have the shape of a centered circle with radius of B_H (total horizontal magnetic field density). Equation 3.44 describes this relation:

$$B_H^2 = B_x^{b2} + B_y^{b2}, \tag{3.44}$$

However, the errors described in Chapter 2 reshape that circle into a shifted, rotated ellipse. Each effect can be observed in Figure 3.2, where δB_H stands for the combined effect of both biases and hard iron errors (FOSTER; ELKAIM, 2008).

Figure 3.2 – Effects of error components on original circle. (Adapted from Gebre-Egziabher et al. (2006))

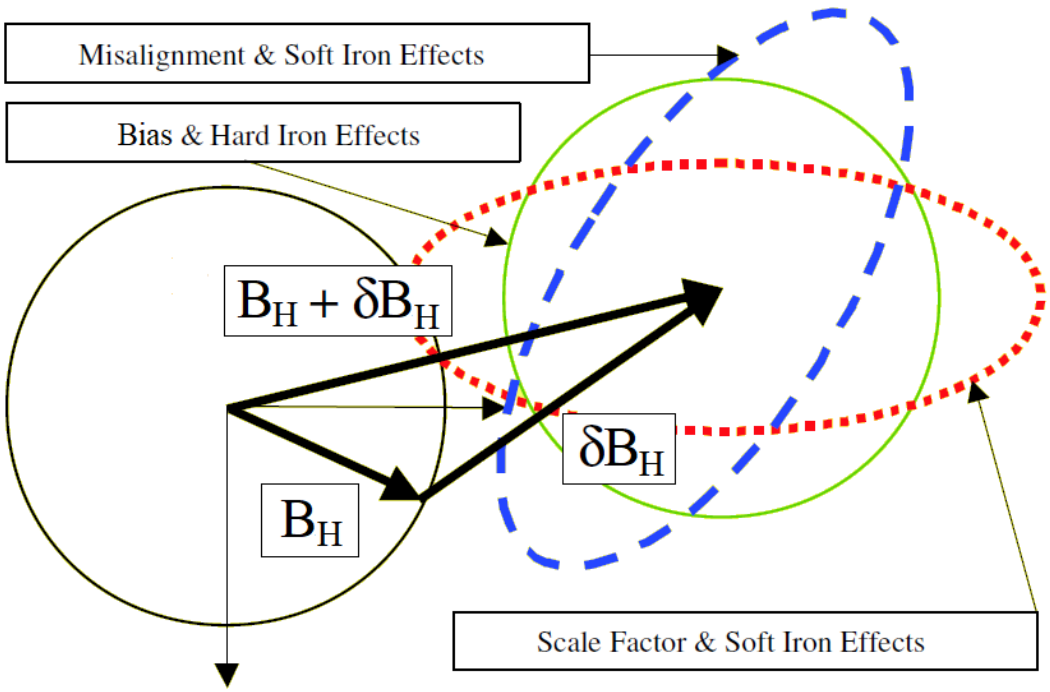

Therefore, it is clear that the ellipse parameters are directly related to the errors. Nevertheless, notice that some error parameters are mathematically indistinguishable, since they produce the same distortions on the plotted ellipse. The shifting effect, for instance, is caused

by both biases and hard iron effects. Thus, they are treated in ETS simply as the biases x_o and y_o. Conversely, the distortions caused by soft iron effects are the same as those produced by misalignments and scale factors. Therefore, soft iron effects are also represented in ETS as part of the scale factors a and b, and the misalignment ρ. Lastly, as noise is considered to have a zero-mean, Gaussian distribution, whose effect is smoothed over the progression of the calibration method, it is not considered in the estimation model.

Based on the preceding assumptions and in agreement with Chapter 2, the measured magnetometer outputs are described as follows, where the x-sensor is considered to be aligned with body x-axis:

$$\hat{B}_x^b = aB_x^b + x_o \tag{3.45}$$

$$\hat{B}_y^b = b[B_y^b \cos(\rho) + B_x^b \sin(\rho)] + y_o, \tag{3.46}$$

The first step in the ETS calibration methodology consists of estimating the parameters that define the shifted, rotated ellipse. Without loss of generality, geometrical shapes can be represented by parametric models. In this case, the ellipse is represented as a conic section. The relation can be found, starting by solving (3.45) and (3.46) for B_x^b and B_y^b, respectively, and plugging the results into (3.44), yielding:

$$A\hat{B}_x^{b2} + B\hat{B}_x^b\hat{B}_y^b + C\hat{B}_y^{b2} + D\hat{B}_x^b + E\hat{B}_y^b + F = 0, \tag{3.47}$$

Notice that (3.47) is linear in terms of A, B, C, D, E, and F, but not in terms of the actual error parameters x_o, y_o, a, b, and ρ. Estimates of the former parameters are found via a least squares algorithm, which requires some adjustments to (3.47), as follows:

$$\begin{bmatrix} \hat{B}_x^{b2} & \hat{B}_x^b\hat{B}_y^b & \hat{B}_x^b & \hat{B}_y^b & 1 \end{bmatrix} \begin{bmatrix} \frac{A}{C} \\ \frac{B}{C} \\ \frac{D}{C} \\ \frac{E}{C} \\ \frac{F}{C} \end{bmatrix} = -\hat{B}_y^{b2} \tag{3.48}$$

Next, magnetometer measurements of all available epochs are combined into matrices H_{2D} and $\boldsymbol{Y}$ [1].

$$H_{2D}\boldsymbol{X}_{2D} = \boldsymbol{Y}, \tag{3.49}$$

with

$$\boldsymbol{X}_{2D} = \begin{bmatrix} \frac{A}{C} & \frac{B}{C} & \frac{D}{C} & \frac{E}{C} & \frac{F}{C} \end{bmatrix}^T, \tag{3.50}$$

$$\boldsymbol{Y} = \begin{bmatrix} -\hat{B}_{y1}^{b2} & -\hat{B}_{y2}^{b2} & \dots & -\hat{B}_{yk}^{b2} \end{bmatrix}^T, \tag{3.51}$$

$$H_{2D} = \begin{bmatrix} \hat{B}_{x1}^{b2} & \hat{B}_{x1}^{b}\hat{B}_{y1}^{b} & \hat{B}_{x1}^{b} & \hat{B}_{y1}^{b} & 1 \\ \hat{B}_{x2}^{b2} & \hat{B}_{x2}^{b}\hat{B}_{y2}^{b} & \hat{B}_{x2}^{b} & \hat{B}_{y2}^{b} & 1 \\ \vdots & \vdots & \vdots & \vdots & \vdots \\ \hat{B}_{xk}^{b2} & \hat{B}_{xk}^{b}\hat{B}_{yk}^{b} & \hat{B}_{xk}^{b} & \hat{B}_{yk}^{b} & 1 \end{bmatrix} \tag{3.52}$$

where k is the epoch of each measurement taken.

Lastly, where $k \geq 5$, (3.53) is the pseudo [2] least squares solution [3]:

$$\hat{\boldsymbol{X}}_{2D} = (H_{2D}^T H_{2D})^{-1} H_{2D}^T \boldsymbol{Y} \tag{3.53}$$

where $\hat{\boldsymbol{X}}_{2D}$ are the estimated parameters that best fit the ellipse. Finally, even though not included in (FOSTER; ELKAIM, 2008), x_o, y_o, a, b, and ρ, are found to be functions of A, B, C, D, E, and F, and can be calculated either algebraically or numerically, as long as B_H is known. The latter is easily computed through world magnetic field models, as the US/UK World Magnetic Model (WMM) and International Geomagnetic Reference Field (IGRF) (CHULLIAT et al., 2015; THÉBAULT et al., 2015). The fact that Foster and Elkaim (2008) did not provide a clear

[1] These matrices, in their current format, are defined differently than in the original algorithm proposed by Foster and Elkaim (2008), as we wish to differentiate the two-dimensional from the three-dimensional ETS calibration matrices.

[2] The term pseudo least squares is adopted here, as in the work by Vasconcelos et al. (2011), as the measurement matrix H_{2D} is not independent on the measurement readings (requirement of the classical least squares)

[3] Notice the typo (lack of $\boldsymbol{Y}$) in Equation (15) of the work by Foster and Elkaim (2008)

methodology (either numerical or analytical) for recuperating the sough calibration parameters from $\hat{\boldsymbol{X}}_{2D}$ was the main motivation for the study conducted in Chapter 4.

3.4.2.2 Three-dimensional Calibration

The three-dimensional magnetometer calibration via ETS methodology follows the same ideas described in Section 3.4.2.1. However, instead of calculating the parameters of an ellipse, defined as a conic section, the objective now is to estimate the parameters of a shifted, rotated ellipsoid, defined as a quadric surface. Firstly, the parametrization of the z-axis' magnetometer measurements is necessary, in agreement with Chapter 2:

$$\hat{B}_z^b = c[B_z^b \cos(\phi)\cos(\lambda) + B_x^b \sin(\phi)\cos(\lambda) + B_y^b \sin(\lambda)] + z_o \tag{3.54}$$

In addition, instead of taking the horizontal magnetic field density magnitude B_H as a reference, the total magnetic field intensity B is necessary. The relation described in (3.55) suggests, analogously to (3.44), that the magnitude of the vectors B_x^b, B_y^b, and B_z^b always falls onto the surface of a sphere with radius B:

$$B^2 = B_x^{b2} + B_y^{b2} + B_z^{b2} \tag{3.55}$$

The ellipsoid whose parameters are to be estimated is described by the quadric surface general equation (3.56), which can be obtained by isolating B_x^b, B_y^b and B_z^b in (3.45), (3.46) and (3.54), respectively, and plugging the results into (3.55) [4].

$$A\hat{B}_x^{b2} + B\hat{B}_x^b\hat{B}_y^b + C\hat{B}_x^b\hat{B}_z^b + D\hat{B}_y^{b2} + E\hat{B}_y^b\hat{B}_z^b + F\hat{B}_z^{b2} + G\hat{B}_x^b + H\hat{B}_y^b + I\hat{B}_z^b + J = 0, \tag{3.56}$$

To proceed as suggested, we rewrite (3.56) in matrix format as [5]:

[4] Notice again, that there is a small typing error in this equation at the original work by Foster and Elkaim (2008), namely, an extra F in the sixth term.

[5] Again, the matrices arranged for the least squares computation are defined slightly differently from the original algorithm presented by Foster and Elkaim (2008).

$$\begin{bmatrix} \hat{B}_x^{b2} & \hat{B}_x^b\hat{B}_y^b & \hat{B}_x^b\hat{B}_z^b & \hat{B}_y^b\hat{B}_z^b & \hat{B}_z^{b2} & \hat{B}_x^b & \hat{B}_y^b & \hat{B}_z^b & 1 \end{bmatrix} \begin{bmatrix} \frac{A}{D} \\ \frac{B}{D} \\ \frac{C}{D} \\ \frac{E}{D} \\ \frac{F}{D} \\ \frac{G}{D} \\ \frac{H}{D} \\ \frac{I}{D} \\ \frac{J}{D} \end{bmatrix} = -\hat{B}_y^{b2} \tag{3.57}$$

Next, (3.57) is augmented for arbitrary ($k \geq 9$) magnetometer measurements:

$$H_{3D}\boldsymbol{X}_{3D} = \boldsymbol{Y}, \tag{3.58}$$

where H_{3D}, $\boldsymbol{X}_{3D}$, and $\boldsymbol{Y}$ are:

$$\boldsymbol{X}_{3D} = \begin{bmatrix} \frac{A}{D} & \frac{B}{D} & \frac{C}{D} & \frac{E}{D} & \frac{F}{D} & \frac{G}{D} & \frac{H}{D} & \frac{I}{D} & \frac{J}{D} \end{bmatrix}^T, \tag{3.59}$$

$$\boldsymbol{Y} = \begin{bmatrix} -\hat{B}_{y1}^{b2} & -\hat{B}_{y2}^{b2} & . & . & -\hat{B}_{yk}^{b2} \end{bmatrix}^T, \tag{3.60}$$

$$H_{3D} = \begin{bmatrix} \hat{B}_{x1}^{b2} & \hat{B}_{x1}^b\hat{B}_{y1}^b & \hat{B}_{x1}^b\hat{B}_{z1}^b & \hat{B}_{y1}^b\hat{B}_{z1}^b & \hat{B}_{z1}^{b2} & \hat{B}_{x1}^b & \hat{B}_{y1}^b & \hat{B}_{z1}^b & 1 \\ \hat{B}_{x2}^{b2} & \hat{B}_{x2}^b\hat{B}_{y2}^b & \hat{B}_{x2}^b\hat{B}_{z2}^b & \hat{B}_{y2}^b\hat{B}_{z2}^b & \hat{B}_{z2}^{b2} & \hat{B}_{x2}^b & \hat{B}_{y2}^b & \hat{B}_{z2}^b & 1 \\ . & . & . & . & . & & & & \\ . & . & . & . & . & & & & \\ \hat{B}_{xk}^{b2} & \hat{B}_{xk}^b\hat{B}_{yk}^b & \hat{B}_{xk}^b\hat{B}_{zk}^b & \hat{B}_{yk}^b\hat{B}_{zk}^b & \hat{B}_{zk}^{b2} & \hat{B}_{xk}^b & \hat{B}_{yk}^b & \hat{B}_{zk}^b & 1 \end{bmatrix} \tag{3.61}$$

Finally, the pseudo least squares formulation is written as:

$$\boldsymbol{X}_{3D} = (H_{3D}^T H_{3D})^{-1} H_{3D}^T \boldsymbol{Y} \tag{3.62}$$

where $\boldsymbol{X}_{3D}$ are the estimated ellipsoid parameters (auxiliary or intermediate parameters) that minimize the quadratic error with respect to the measurements $\boldsymbol{Y}$, as in Section 3.4.2.1.

Again, the ellipsoid parameters are functions of the sought error parameters, and the relation between them can be found algebraically (or numerically). As such relation has not been clearly described by Foster and Elkaim (2008), this motivated the discussions of Chapter 5. The local-global variables equivalency is summarized in Table 3.2.

Table 3.2 – Input and output variables equivalency for the ETS method.

Local variables	Global equivalent	Type (I/O)	Definition
$\hat{B}^b$	$\tilde{\boldsymbol{m}}$	I	Measured magnetic field density
B	m_t	I	Earth's total local magnetic field density magnitude
B_H	m_h	I	Earth's total horizontal magnetic field density magnitude
x_o	b_x	O	x-axis bias
y_o	b_y	O	y-axis bias
z_o	b_z	O	z-axis bias
a	s_x	O	x-axis scale factor
b	s_y	O	y-axis scale factor
c	s_z	O	z-axis scale factor

3.4.3 Maximum Likelihood Estimation-based Method

The magnetometer calibration method developed by Vasconcelos et al. (2011) takes the technique by Foster and Elkaim (2008) described previously as an initial estimate of the systematic errors. For easiness of reference with Vasconcelos et al. (2011), the following magnetometer model is introduced, comprising local variables:

$$\boldsymbol{h}_{ri} = \boldsymbol{S}_M \boldsymbol{C}_{NO} (\boldsymbol{C}_{SI} \, {}^{B}_{E}\boldsymbol{R}_i \, | \, {}^{E}\boldsymbol{h} \, | \, {}^{E}\bar{\boldsymbol{h}}_i + \boldsymbol{b}_{HI}) + \boldsymbol{b}_M + \boldsymbol{n}_{mi} \tag{3.63}$$

where $\boldsymbol{h}_{ri}$ is the i_{th} sensor reading, $\boldsymbol{S}_M$ is the scale factor matrix, $\boldsymbol{C}_{NO}$ is the nonorthogonality (misalignment) matrix, $\boldsymbol{C}_{SI}$ is the soft iron matrix, ${}^{B}_{E}\boldsymbol{R}_i$ is the rotation matrix from body to ECEF frame, ${}^{E}\boldsymbol{h}$ is the Earth's total magnetic field density vector resolved in ECEF-axes, ${}^{E}\bar{\boldsymbol{h}}_i$ is the normalized Earth magnetic field density in ECEF-axes, $\boldsymbol{b}_{HI}$ is the hard iron vector, $\boldsymbol{b}_M$ is the

bias vector, and $\boldsymbol{n}_{mi}$ is the measurement noise, considered to have a zero mean, white, Gaussian distribution.

However, as in the work by Foster and Elkaim (2008), the error parameters are not observable separately. Therefore, only two matrices/vectors are actually estimated: $\boldsymbol{C}$ (or $\boldsymbol{T}$, where $\boldsymbol{T} = \boldsymbol{C}^{-1}$), which is a function of the combined effects of soft iron, scaling factors and misalignments, and $\boldsymbol{b}$, which is a function of the offset (hard iron and bias) effects. In terms of our previously defined global variables, $\boldsymbol{T}$ is a function of C_m and C_s, and $\boldsymbol{b}$ and $\boldsymbol{n}_{mi}$ are equivalent to $\boldsymbol{c}_b$ and $\boldsymbol{c}_\mu$, respectively. Consequently, the error model becomes:

$$\boldsymbol{h}_{ri} = \boldsymbol{C}\,{}^{B}\bar{\boldsymbol{h}}_i + \boldsymbol{b} + \boldsymbol{n}_{mi} \tag{3.64}$$

where $\boldsymbol{C} = \boldsymbol{S}_M\boldsymbol{C}_{NO}\boldsymbol{C}_{SI}|^{E}\boldsymbol{h}|$, $\boldsymbol{b} = \boldsymbol{S}_M\boldsymbol{C}_{NO}\boldsymbol{b}_{HI} + \boldsymbol{b}_M$ and ${}^{B}\bar{\boldsymbol{h}}_i = {}^{B}_{E}\boldsymbol{R}_i\,{}^{E}\bar{\boldsymbol{h}}_i$.

The first step to estimate $\boldsymbol{T}$ and $\boldsymbol{b}$ is to find the initial estimates via the work by Foster and Elkaim (2008). However, Foster and Elkaim (2008) only provided the ellipsoid parameters estimate of (3.62) in their work. Thus, Vasconcelos et al. (2011) proposed analytical solutions for the error parameters C_m, C_s and $\boldsymbol{c}_b$ via the estimates from (3.62). Nevertheless, such solutions are not directly comparable, since (3.59) and (3.60) are defined differently by Vasconcelos et al. (2011), as follows:

$$\boldsymbol{X}_v = -\begin{bmatrix} \frac{A}{F} & \frac{B}{F} & \frac{C}{F} & \frac{D}{F} & \frac{E}{F} & \frac{G}{F} & \frac{H}{F} & \frac{I}{F} & \frac{J}{F} \end{bmatrix}^T, \tag{3.65}$$

$$\boldsymbol{Y}_v = \begin{bmatrix} \tilde{m}_{z1}^2 & \tilde{m}_{z2}^2 & . & . & \tilde{m}_{zk}^2 \end{bmatrix}^T, \tag{3.66}$$

In the appendix of (VASCONCELOS et al., 2011), the estimates from (3.65) are referred to simply as A, B, C, D, E, G, H and J. In order to distinguish them from the ellipsoid parameters of (3.65), we write $\boldsymbol{X}_v$ as:

$$\boldsymbol{X}_v = \begin{bmatrix} x_{v1} & x_{v2} & x_{v3} & x_{v4} & x_{v5} & x_{v6} & x_{v7} & x_{v8} & x_{v9} \end{bmatrix}^T, \tag{3.67}$$

The estimates $\boldsymbol{X}_v$ relate to $\boldsymbol{X}_{3D}$ as:

$$\begin{bmatrix} x_{v1} \\ x_{v2} \\ x_{v3} \\ x_{v4} \\ x_{v5} \\ x_{v6} \\ x_{v7} \\ x_{v8} \\ x_{v9} \end{bmatrix} = - \begin{bmatrix} x_{3D_1} \\ x_{3D_2} \\ x_{3D_3} \\ 1 \\ x_{3D_4} \\ x_{3D_6} \\ x_{3D_7} \\ x_{3D_8} \\ x_{3D_9} \end{bmatrix} \frac{1}{x_{3D_5}} \tag{3.68}$$

Once $\boldsymbol{X}_v$ has been distinguished from $\boldsymbol{X}_{3D}$, we can present Vasconcelos' analytical solution for the error parameters in terms of the former, as follows:

$$\alpha_1 = -x_{v2}^2 + x_{v4}x_{v3}^2 + 4x_{v4}x_{v1} + x_{v1}x_{v5}^2 - x_{v2}x_{v5}x_{v3} \tag{3.69}$$

$$\begin{aligned} \alpha_2 = \; & 4x_{v1}x_{v5}^2x_{v9} - x_{v5}^2x_{v6}^2 - 4x_{v2}x_{v5}x_{v3}x_{v9} + 2x_{v5}x_{v3}x_{v7}x_{v6} + 2x_{v2}x_{v5}x_{v8}x_{v6} - 4x_{v5}x_{v7}x_{v1}x_{v8} \\ & -4x_{v4}x_{v8}x_{v3}x_{v6} - x_{v3}^2x_{v7}^2 + 4x_{v4}x_{v1}x_{v8}^2 + 2x_{v3}x_{v2}x_{v7}x_{v8} - 4x_{v4}x_{v6}^2 + 4x_{v4}x_{v3}^2x_{v9} \\ & +4x_{v2}x_{v7}x_{v6} - 4x_{v1}x_{v7}^2 - x_{v2}^2x_{v8}^2 - 4x_{v2}^2x_{v9} + 16x_{v4}x_{v1}x_{v9} \end{aligned} \tag{3.70}$$

$$\alpha_3 = x_{v5}^4x_{v1} - x_{v3}x_{v2}x_{v5}^3 + x_{v5}^2x_{v3}^2x_{v4} - 2x_{v2}^2x_{v5}^2 + 8x_{v4}x_{v1}x_{v5}^2 - 4x_{v4}x_{v2}^2 + 16x_{v4}^2x_{v1} \tag{3.71}$$

$$\beta_1 = 2x_{v2}x_{v7} + x_{v2}x_{v5}x_{v8} - 2x_{v3}x_{v4}x_{v8} - 4x_{v4}x_{v6} + x_{v5}x_{v3}x_{v7} - x_{v5}^2x_{v6} \tag{3.72}$$

$$\beta_2 = -2x_{v1}x_{v5}x_{v8} + 4x_{v1}x_{v7} - x_{v2}x_{v3}x_{v8} - 2x_{v2}x_{v6} + x_{v3}^2x_{v7} - x_{v3}x_{v5}x_{v6} \tag{3.73}$$

$$\beta_3 = 4x_{v4}x_{v8}x_{v1} - 2x_{v4}x_{v6}x_{v3} + x_{v5}x_{v6}x_{v2} - x_{v8}x_{v2}^2 - 2x_{v5}x_{v7}x_{v1} + x_{v3}x_{v2}x_{v7} \tag{3.74}$$

Next, we use the auxiliary parameters $\alpha_1, \alpha_2, \alpha_3, \beta_1, \beta_2$ and β_3 to find the initial estimate of the error parameters that describe $\boldsymbol{T}$ and $\boldsymbol{b}$.

$$a = \frac{1}{2\alpha_1}[-(4x_{v4} + x_{v5}^2)\alpha_2]^{1/2} \tag{3.75}$$

$$b = \frac{1}{2\alpha_1}[-(4x_{v1} + x_{v3}^2)\alpha_2]^{1/2} \tag{3.76}$$

$$c = \frac{1}{2\alpha_1}[(4x_{v4}x_{v1} - x_{v2}^2)\alpha_2]^{1/2} \tag{3.77}$$

$$\rho_v = \arctan\left[-\frac{1}{2}(2x_{v2} + x_{v5}x_{v3})(\alpha_1)^{-1/2}\right] \tag{3.78}$$

$$\phi_v = \arctan\left[(x_{v2}x_{v5} - x_{v3}x_{v4})(\alpha_1)^{-1/2}\right] \tag{3.79}$$

$$\lambda_v = \arctan\left[x_{v5}(-\alpha_1\alpha_3^{-1})^{1/2}\right] \tag{3.80}$$

The initial estimates for $\boldsymbol{T}$ and $\boldsymbol{b}$ are written as follows [6]:

$$\boldsymbol{T}_0 = \begin{bmatrix} \frac{1}{a} & 0 & 0 \\ -\frac{1}{a}\tan\rho_v & \frac{1}{b}\sec\rho_v & 0 \\ \frac{1}{a}(\tan\rho_v\tan\lambda_v\sec\phi_v - \tan\phi_v) & -\frac{1}{b}\sec\rho_v\tan\lambda_v\sec\phi_v & \frac{1}{c}\sec\lambda_v\sec\phi_v \end{bmatrix} \tag{3.81}$$

$$\boldsymbol{b}_0 = \frac{1}{2\alpha_1}\begin{bmatrix} \beta_1 \\ \beta_2 \\ \beta_3 \end{bmatrix} \tag{3.82}$$

[6] Notice that the term in position (2,2) of matrix $\boldsymbol{T}_0$ incorrectly has a minus sign in the original work. This mistake has been corrected in (3.81).

The next step is to implement a Gauss-Netwon's descent-based Maximum Likelihood Estimator (MLE), which iterates until a condition $||\nabla f|_{\boldsymbol{x}_k}|| < \varepsilon_{stop}$ is satisfied, where $\| \|$ is the representation for the Mahalanobis distance [7], as follows:

$$\begin{bmatrix} vec(\boldsymbol{T}_{k+1}) \\ \boldsymbol{b}_{k+1} \end{bmatrix} = \begin{bmatrix} vec(\boldsymbol{T}_k) \\ \boldsymbol{b}_k \end{bmatrix} - (\nabla^2 f|_{\boldsymbol{x}_k})^{-1} \nabla f|_{\boldsymbol{x}_k} \tag{3.83}$$

where the gradient of the likelihood function is defined as [8]:

$$\nabla f|_{\boldsymbol{x}} = \begin{bmatrix} \nabla f|_{\boldsymbol{T}} & \nabla f|_{\boldsymbol{b}} \end{bmatrix}^T \tag{3.84}$$

$$\nabla f|_{\boldsymbol{T}} = \sum_{i=1}^{n} \frac{2c_{\boldsymbol{T}}}{\sigma_{mi}^2} \boldsymbol{u}_i \otimes \boldsymbol{T}\boldsymbol{u}_i \tag{3.85}$$

$$\nabla f|_{\boldsymbol{b}} = \sum_{i=1}^{n} \frac{-2c_{\boldsymbol{T}}}{\sigma_{mi}^2} \boldsymbol{T}^T \boldsymbol{T}\boldsymbol{u}_i \tag{3.86}$$

with,

$$c_{\boldsymbol{T}} = 1 - |\boldsymbol{T}\boldsymbol{u}_i|^{-1} \tag{3.87}$$

$$\boldsymbol{u}_i = \boldsymbol{h}_{ri} - \boldsymbol{b} \tag{3.88}$$

where σ_{mi} is the magnetometer random noise standard deviation, $\otimes$ represents the Kronecker product (see Appendix A for details), and $|\,|$ the Euclidian norm. The Hessian of the likelihood function, in turn, is defined as:

$$\nabla^2 f|_{\boldsymbol{x}} = \begin{bmatrix} H_{\boldsymbol{T},\boldsymbol{T}} & H_{\boldsymbol{T},\boldsymbol{b}} \\ H_{\boldsymbol{T},\boldsymbol{b}}^T & H_{\boldsymbol{b},\boldsymbol{b}} \end{bmatrix} \tag{3.89}$$

where

$$H_{\boldsymbol{T},\boldsymbol{T}} = \sum_{i=1}^{n} \frac{2}{\sigma_{mi}^2} \left[\frac{(\boldsymbol{u}_i \boldsymbol{u}_i^T) \otimes (\boldsymbol{T}\boldsymbol{u}_i \boldsymbol{u}_i^T \boldsymbol{T}^T)}{|\boldsymbol{T}\boldsymbol{u}_i|^3} + c_{\boldsymbol{T}} [(\boldsymbol{u}_i \boldsymbol{u}_i^T) \otimes I_3] \right] \tag{3.90}$$

[7] The Mahalanobis distance considers the distribution of the object points in the variable space (as characterized by the covariance matrix) and is independent from the scaling of the variables. It is a distance measure that accounts for the covariance structure (VARMUZA; FILZMOSER, 2016).

[8] Notice that, in the work by Vasconcelos et al. (2011), equation (3.84) is missing the transpose sign ^{T}.

$$H_{\boldsymbol{T},\boldsymbol{b}} = \sum_{i=1}^{n} \frac{-2}{\sigma_{mi}^2} \left[\frac{(\boldsymbol{u}_i \otimes \boldsymbol{T}\boldsymbol{u}_i)\boldsymbol{u}_i^T \boldsymbol{T}^T \boldsymbol{T}}{|\boldsymbol{T}\boldsymbol{u}_i|^3} + c_{\boldsymbol{T}}(\boldsymbol{u}_i \otimes \boldsymbol{T} + I_3 \otimes \boldsymbol{T}\boldsymbol{u}_i) \right] \tag{3.91}$$

$$H_{\boldsymbol{b},\boldsymbol{b}} = \sum_{i=1}^{n} \frac{2}{\sigma_{mi}^2} \left[\frac{\boldsymbol{T}^T \boldsymbol{T}\boldsymbol{u}_i \boldsymbol{u}_i^T \boldsymbol{T}^T \boldsymbol{T}}{|\boldsymbol{T}\boldsymbol{u}_i|^3} + c_{\boldsymbol{T}} \boldsymbol{T}^T \boldsymbol{T} \right] \tag{3.92}$$

After $||\nabla f|_{\boldsymbol{x}}||$ reaches a desired threshold, the final estimates of $\boldsymbol{T}$ and $\boldsymbol{b}$ need to be converted back into the error parameters, which is achieved in terms of global variables as follows:

$$M = \frac{1}{|{}^E\boldsymbol{h}|} \boldsymbol{T}^{-1} \tag{3.93}$$

$$\rho = \arctan \frac{M_{2,1}}{M_{2,2}} \tag{3.94}$$

$$\phi = \arctan \frac{M_{3,1}}{M_{3,3}} \tag{3.95}$$

$$\lambda = \arctan \left(\frac{M_{3,2}}{M_{3,1}} \right) \sin \phi \tag{3.96}$$

$$s_x = M_{1,1} \tag{3.97}$$

$$s_y = \frac{M_{2,1}}{\sin \rho} \tag{3.98}$$

$$s_z = \frac{M_{3,2}}{\sin \lambda} \tag{3.99}$$

$$\boldsymbol{c}_b = \boldsymbol{b} \tag{3.100}$$

In summary, the technique by Vasconcelos et al. (2011) requires three inputs: $\boldsymbol{h}_{ri}$, $|{}^E\boldsymbol{h}|$ and σ_{mi}, which are equivalent in terms of global input variables to $\tilde{\boldsymbol{m}}$, m_t and σ_μ (standard deviation of the measurement noise $\boldsymbol{c}_\mu$). The relation between the local/global input/output variables is summarized in Table 3.3 and in (3.94) to (3.100).

Table 3.3 – Input and output variables equivalency for the MLE method.

Local variables	Global equivalent	Type (I/O)	Definition
$\boldsymbol{h}_{ri}$	$\tilde{\boldsymbol{m}}$	I	Measured magnetic field density
${}^{E}\boldsymbol{h}$	m_t	I	Earth's total local magnetic field density magnitude
$\boldsymbol{n}_{mi}$	$\boldsymbol{c}_{\mu}$	I	Measurement noise
$\boldsymbol{C}$	$C_s C_m C_b^s m_t$	I/O	Misalignments and scale factors
$\boldsymbol{b}$	$\boldsymbol{c}_b$	O	Biases

where C_b^s is a rotation matrix from body to sensor frame.

3.4.4 Constrained Total Least Squares-based Method

Wu et al. (2013) proposed a Constrained Total Least-Squares (CTLS) technique for tri-axial magnetometer calibration. The error model adopted in this methodology is the same adopted in this work, with a different notation (local variables are once again employed, for easiness of reference with the work by Wu et al. (2013)), as follows:

$$\mathbf{B}^s = \mathbf{K}\mathbf{B}^b + \mathbf{O} \tag{3.101}$$

with

$$\mathbf{K} = \begin{bmatrix} \kappa_1 & 0 & 0 \\ \kappa_2 \sin\rho_1 & k_2 \cos\rho_1 & 0 \\ \kappa_3 \sin\rho_2 \cos\rho_3 & \kappa_3 \sin\rho_3 & \kappa_3 \cos\rho_2 \cos\rho_3 \end{bmatrix} \tag{3.102}$$

$$\mathbf{O} = \begin{bmatrix} o_1 \\ o_2 \\ o_3 \end{bmatrix} \tag{3.103}$$

where $\mathbf{B}^s$ stands for the magnetometer readings in the sensor frame, $\mathbf{K}$ contains the scale factors and misalignment effects, $\mathbf{B}^b$ represents the Earth magnetic field density at each axis of the body frame, and $\mathbf{O}$ contains the total bias (offset) effects that corrupt the sensor readings. Once again, as in the methods presented previously, $\mathbf{K}$ and $\mathbf{O}$ include the mathematical effects of soft and hard iron errors, represented as scale factors, misalignments and biases, respectively.

The calibration methodology is summarized into four steps. The first consists of calculating initial estimates for the error parameters, which is achieved via the ETS estimator by Foster and Elkaim (2008), with a different notation:

$$\mathbf{X}_{LS} = (\mathbf{A}^T\mathbf{A})^{-1}\mathbf{A}^T\mathbf{b} \tag{3.104}$$

where the subscript LS indicates the least-squares estimate of vector $\mathbf{X}$, defined as:

$$\mathbf{X} = -\frac{1}{a_6}\begin{bmatrix} a_1 & a_2 & a_3 & a_4 & a_5 & a_7 & a_8 & a_9 & a_{10} \end{bmatrix}^T, \tag{3.105}$$

$$\mathbf{A} = \begin{bmatrix} (B^s_{x1})^2 & B^s_{x1}B^s_{y1} & B^s_{x1}B^s_{z1} & (B^s_{y1})^2 & B^s_{y1}B^s_{z1} & B^s_{x1} & B^s_{y1} & B^s_{z1} & 1 \\ (B^s_{x2})^2 & B^s_{x2}B^s_{y2} & B^s_{x2}B^s_{z2} & (B^s_{y2})^2 & B^s_{y2}B^s_{z2} & B^s_{x2} & B^s_{y2} & B^s_{z2} & 1 \\ \vdots & \vdots & \vdots & \vdots & \vdots & \vdots & \vdots & \vdots & \vdots \\ (B^s_{xq})^2 & B^s_{xq}B^s_{yq} & B^s_{xq}B^s_{zq} & (B^s_{yq})^2 & B^s_{yq}B^s_{zq} & B^s_{xq} & B^s_{yq} & B^s_{zq} & 1 \end{bmatrix} \tag{3.106}$$

$$\mathbf{b} = \begin{bmatrix} (B^s_{z1})^2 & (B^s_{z2})^2 & \dots & (B^s_{zq})^2 \end{bmatrix}^T, \tag{3.107}$$

where q is the q_{th} measurement, and $\mathbf{X}$ contains the estimated ellipsoid parameters.

Once the initial estimates are computed, we can move on to the second step, which consists of iteratively refining $\mathbf{X}$ using Gauss-Newton's descent method:

$$\mathbf{X}_{r+1} = \mathbf{X}_r - \mathbf{H}_r^{-1}\mathbf{T}_r \tag{3.108}$$

where r represents the r_{th} iteration, $\mathbf{H}_r$ is the Hessian matrix at $\mathbf{X}_r$, and $\mathbf{T}_r$ the gradient vector, computed as follows:

$$\mathbf{T}_r = 2(\mathbf{U}^T\mathbf{A} - \mathbf{U}^T\mathbf{B}_1)^T, \tag{3.109}$$

$$\mathbf{H}_r = 2(\mathbf{A} - \mathbf{B}_1 - \mathbf{B}_2)^T(\mathbf{H}_X\mathbf{H}_X^T)^{-1}(\mathbf{A} - \mathbf{B}_1 - \mathbf{B}_2) - 2\mathbf{B}_3^T\mathbf{B}_3, \tag{3.110}$$

with

$$\mathbf{U} = (\mathbf{H}_X\mathbf{H}_X^T)^{-1}\mathbf{C}\begin{pmatrix}\mathbf{X} \\ -1\end{pmatrix}, \tag{3.111}$$

$$\mathbf{B}_1 = \begin{bmatrix} \mathbf{H}_X\mathbf{F}_1^T U & \mathbf{H}_X\mathbf{F}_2^T\mathbf{U} & \ldots & \mathbf{H}_X\mathbf{F}_L^T\mathbf{U} \end{bmatrix}, \tag{3.112}$$

$$\mathbf{B}_2 = \begin{bmatrix} \mathbf{F}_1\mathbf{H}_X^T U & \mathbf{F}_2\mathbf{H}_X^T\mathbf{U} & \ldots & \mathbf{F}_L\mathbf{H}_X^T\mathbf{U} \end{bmatrix}, \tag{3.113}$$

$$\mathbf{B}_2 = \begin{bmatrix} \mathbf{F}_1^T U & \mathbf{F}_2^T\mathbf{U} & \ldots & \mathbf{F}_L^T\mathbf{U} \end{bmatrix}, \tag{3.114}$$

where

$$\mathbf{C} = \begin{bmatrix} \mathbf{A} & \mathbf{b} \end{bmatrix}, \tag{3.115}$$

$$\mathbf{F}_1 = \begin{bmatrix} -2B_{x1}^s & 0 & 0 & & & & & \\ & & & -2B_{x2}^s & 0 & 0 & & \\ & & & & & & \ddots & \\ & & & & & & 2B_{xq}^s & 0 & 0 \end{bmatrix}_{q\times 3q}, \tag{3.116}$$

$$\mathbf{F}_2 = \begin{bmatrix} -B_{y1}^s & -B_{x1}^s & 0 & & & & & \\ & & & -B_{y2}^s & -B_{x2}^s & 0 & & \\ & & & & & & \ddots & \\ & & & & & & -B_{yq}^s & -B_{xq}^s & 0 \end{bmatrix}_{q\times 3q}, \tag{3.117}$$

$$\mathbf{F}_3 = \begin{bmatrix} -B_{z1}^s & 0 & -B_{x1}^s & & & & & \\ & & & -B_{z2}^s & 0 & -B_{x2}^s & & \\ & & & & & & \ddots & \\ & & & & & & -B_{zq}^s & 0 & -B_{xq}^s \end{bmatrix}_{q\times 3q}, \tag{3.118}$$

$$\mathbf{F}_4 = \begin{bmatrix} 0 & -B_{y1}^s & 0 & & & & & \\ & & & 0 & -B_{y2}^s & 0 & & \\ & & & & & & \ddots & \\ & & & & & & 0 & -B_{yq}^s & 0 \end{bmatrix}_{q\times 3q}, \tag{3.119}$$

$$\mathbf{F}_5 = \begin{bmatrix} 0 & -B^s_{z1} & -B^s_{y1} & & & & & & \\ & & & 0 & -B^s_{z2} & -B^s_{y2} & & & \\ & & & & & & \ddots & & \\ & & & & & & & 0 & -B^s_{zq} & -B^s_{yq} \end{bmatrix}_{q\times 3q}, \tag{3.120}$$

$$\mathbf{F}_6 = \begin{bmatrix} -1 & 0 & 0 & & & & & & \\ & & & -1 & 0 & 0 & & & \\ & & & & & & \ddots & & \\ & & & & & & & -1 & 0 & 0 \end{bmatrix}_{q\times 3q}, \tag{3.121}$$

$$\mathbf{F}_7 = \begin{bmatrix} 0 & -1 & 0 & & & & & & \\ & & & 0 & -1 & 0 & & & \\ & & & & & & \ddots & & \\ & & & & & & & 0 & -1 & 0 \end{bmatrix}_{q\times 3q}, \tag{3.122}$$

$$\mathbf{F}_8 = \begin{bmatrix} 0 & 0 & -1 & & & & & & \\ & & & 0 & 0 & -1 & & & \\ & & & & & & \ddots & & \\ & & & & & & & 0 & 0 & -1 \end{bmatrix}_{q\times 3q}, \tag{3.123}$$

$$\mathbf{F}_9 = 0_{q\times 3q}, \tag{3.124}$$

$$\mathbf{F}_{10} = \begin{bmatrix} 0 & 0 & -2B^s_{z1} & & & & & & \\ & & & 0 & 0 & -2B^s_{z2} & & & \\ & & & & & & \ddots & & \\ & & & & & & & 0 & 0 & -2B^s_{zq} \end{bmatrix}_{q\times 3q}, \tag{3.125}$$

and

$$\mathbf{H}_X = \sum_{i=1}^{9} x_i \mathbf{F}_i - \mathbf{F}_{10} \tag{3.126}$$

where x_i is the r^{th} element of $\mathbf{X}$.

The third step consists of repeating the second until $||\boldsymbol{T}_r|| < \varepsilon_{stop}$ or r reaches an iteration limit.

Finally, the estimated $\mathbf{X}$ is converted into actual error parameters (biases, scale factors and misalignments) in terms of the previously defined global variables using the analytical solution presented by Vasconcelos et al. (2011) described here in (3.69) to (3.82) and (3.93) to (3.100), also noting that CTLS's $\boldsymbol{X}$ is the same of MLE's $\boldsymbol{X}_v$. Table 3.4 summarizes the relation between local and global variables for CTLS.

Table 3.4 – Input and output variables equivalency for the CTLS method.

Local variables	Global equivalent	Type (I/O)	Definition
$\mathbf{B}^s$	$\tilde{\boldsymbol{m}}$	I	Measured magnetic field density in the sensor frame
$\mathbf{B}^b$	$(C_b^s)^T \boldsymbol{m}$	I	Uncorrupted magnetic field density in the body frame
$\mathbf{K}$	$C_s C_m C_b^s$	O	Misalignments and scale factors
$\mathbf{O}$	$\boldsymbol{c}_b$	O	Biases

where C_b^s is a rotation matrix from body to sensor frame.

3.4.5 Optimal Maximum Likelihood-based Method

Wu and Shi (2015) introduced an alternative magnetometer calibration technique based on an MLE algorithm. However, in contrast to the methodologies used previously, the so called Optimal Maximum Likelihood (OML) was proposed as a means of overcoming shortcomings of the regular MLE implementation, such as its sensitivity to initial estimates errors, which may cause the calibration not to converge..

The error model follows the same pattern as the ones presented previously. For easiness of reference with the original work by Wu and Shi (2015), however, the following local variables are adopted here:

$$\mathbf{y} = \mathbf{R}^{-1}\mathbf{m}^b + \mathbf{h} + \mathbf{e} \tag{3.127}$$

where $\mathbf{y}$ is the sensor measurement, $\mathbf{R}^{-1}$ is a matrix containing the scale factors, misalignment errors and soft iron effects, $\mathbf{m}^b$ is the Earth's magnetic field density in the body frame, $\mathbf{h}$ contains

the bias errors and hard iron effects, and **e** is the measurement noise, considered to be Gaussian and have covariance $\sigma\mathbf{I}_3$. The OML-based method requires an initial estimate, which is found via a linear least squares, as follows:

$$\mathbf{Y}_k\mathbf{z} = \begin{bmatrix} \mathbf{y}_k^T \otimes \mathbf{y}_k^T & \mathbf{y}_k^T & 1 \end{bmatrix} \begin{bmatrix} vec(\mathbf{A}) \\ \mathbf{b} \\ c \end{bmatrix} = 0 \tag{3.128}$$

where k is the measurement index, $\otimes$ represents the Kronecker product (see Appendix A for details), $vec(\boldsymbol{A})$ is the operator that forms a vector by stacking the columns of the matrix $\boldsymbol{A}$ but excluding the lower triangular zero entries, and **A** (symmetric), **b** and c are functions of the error parameters.

$$\boldsymbol{A} = \boldsymbol{R}^T\boldsymbol{R} \tag{3.129}$$

$$\boldsymbol{b} = -2\boldsymbol{R}^T\boldsymbol{R}\boldsymbol{h} \tag{3.130}$$

$$c = \boldsymbol{h}^T\boldsymbol{R}^T\boldsymbol{R}\boldsymbol{h} - 1 \tag{3.131}$$

Considering the availability of N measurements, we can form:

$$\mathbf{Y}\mathbf{z} = 0 \tag{3.132}$$

with

$$\mathbf{Y} = [\mathbf{Y}_1'^T \ldots \mathbf{Y}_N'^T]^T \tag{3.133}$$

where

$$\mathbf{Y}_k' = \begin{bmatrix} \mathbf{Y}_{k,1} & \mathbf{Y}_{k,2} + \mathbf{Y}_{k,4} & \mathbf{Y}_{k,5} & \mathbf{Y}_{k,3} + \mathbf{Y}_{k,7} & \mathbf{Y}_{k,6} + \mathbf{Y}_{k,8} & \mathbf{Y}_{k,8} & \ldots & \mathbf{Y}_{k,13} \end{bmatrix} = 0 \tag{3.134}$$

A linear least-squares problem can be expressed as:

$$\mathbf{z} = min|\mathbf{Y}\mathbf{z}|^2 \tag{3.135}$$

The solution of (3.135) should satisfy:

$$\mathbf{Y}^T\mathbf{Y}\mathbf{z} = 0 = 0\mathbf{z} \tag{3.136}$$

Therefore, the solution $\mathbf{z}_e$ is the eigenvector $\mathbf{Y}^T\mathbf{Y}$, with zero or minimum eigenvalue. Noticing that $\alpha\mathbf{z}_e$ for any real α is also solution to (3.135), allows us to write:

$$\begin{bmatrix} vec(\mathbf{A}) \\ \mathbf{b} \\ c \end{bmatrix} = \alpha\mathbf{z}_e = \alpha \begin{bmatrix} vec(\mathbf{A}_e) \\ \mathbf{b}_e \\ c_e \end{bmatrix} \tag{3.137}$$

where

$$\alpha = \frac{4}{\mathbf{b}_e^T\mathbf{A}_e^{-1}\mathbf{b}_e - 4c_e} \tag{3.138}$$

The actual error parameters initial estimates are:

$$\mathbf{h}^{(0)} = -\frac{1}{2}\mathbf{A}^{-1}\mathbf{b} \tag{3.139}$$

$$\mathbf{R}^{(0)} = chol(\mathbf{A}) \tag{3.140}$$

where $chol(.)$ represents the matrix Cholesky factorization.

The next step is to initialize the Optimal Maximum Likelihood estimation vector [9]:

$$\mathbf{x} = \begin{bmatrix} vec^T(\mathbf{T}) & \mathbf{h}^T & \mathbf{m}_1^{bT} & \dots & \mathbf{m}_N^{bT} & \lambda_1 & \dots & \lambda_N \end{bmatrix}^T \tag{3.141}$$

where the initial Lagrange coefficients $\lambda_k^{(0)}$ are set to zero, $\mathbf{m}_k^b = \mathbf{R}^{(0)}(\mathbf{y}_k - \mathbf{h}^{(0)})$, and $\mathbf{T}^{(0)} = (\boldsymbol{R}^{(0)})^{-1}$.

In sequence, the estimate is updated using Gauss-Newton's descent method until a stop condition is fulfilled:

$$\mathbf{x}^{(i+i)} = \mathbf{x}^{(i)} - \left[\nabla_{\mathbf{x}}^2 f|_{\mathbf{x}^{(i)}}\right]^{-1}\left(\nabla_{\mathbf{x}} f|_{\mathbf{x}^{(i)}}\right) \tag{3.142}$$

[9] Notice a small typo in the original paper by (WU; SHI, 2015), where the equation corresponding to (3.141) lacks some transpose operators.

where i is the i^{th} iteration.

The Jacobian (gradient) vector and the Hassian matrix are derived as [10]:

$$\nabla_{\mathbf{x}} f = \begin{bmatrix} \mathbf{J}_T^T & \mathbf{J}_h^T & \mathbf{J}_{m_k^b}^T & \mathbf{J}_{\lambda_k}^T \\ & & {\scriptstyle k=1:N} & {\scriptstyle k=1:N} \end{bmatrix}^T \tag{3.143}$$

$$\nabla_{\mathbf{x}}^2 f = \begin{bmatrix} \mathbf{H}_{TT} & \mathbf{H}_{Th} & \mathbf{H}_{Tm_k^b}\dots & 0_{6\times 1}\dots \\ \mathbf{H}_{Th}^T & \mathbf{H}_{hh} & \mathbf{H}_{hm_k^b}\dots & 0_{3\times 1}\dots \\ \mathbf{H}_{Tm_k^b}^T & \mathbf{H}_{hm_k^b}^T & \mathbf{H}_{m_k^b m_k^b}\dots & \mathbf{H}_{m_k^b\lambda_k}\dots \\ \vdots & \vdots & \vdots & \vdots \\ 0_{6\times 1}^T & 0_{3\times 1} & \mathbf{H}_{m_k^b\lambda_k}\dots & 0\dots \\ \vdots & \vdots & \vdots & \vdots \\ & & {\scriptstyle k=1:N} & {\scriptstyle k=1:N} \end{bmatrix}_{(4N+9)\times(4N+9)} \tag{3.144}$$

with

$$\mathbf{J}_T = -2\sum_{k=1}^{N} \mathbf{m}_k^b \otimes \left(\mathbf{u}_k - \mathbf{T}\mathbf{m}_k^b\right) \tag{3.145}$$

$$\mathbf{J}_h = -2\sum_{k=1}^{N} \left(\mathbf{u}_k - \mathbf{T}\mathbf{m}_k^b\right) \tag{3.146}$$

$$\mathbf{J}_{m_k^b} = -2\mathbf{T}^T\left(\mathbf{u}_k - \mathbf{T}\mathbf{m}_k^b\right) + 2\lambda_k \mathbf{m}_k^b \tag{3.147}$$

$$\mathbf{J}_{\lambda_k} = |\mathbf{m}_k^b|^2 - 1 \tag{3.148}$$

$$\mathbf{H}_{TT} = 2\sum_{k=1}^{N} \left(\mathbf{m}_k^b \mathbf{m}_k^{bT}\right) \otimes \mathbf{I} \tag{3.149}$$

$$\mathbf{H}_{Th} = 2\sum_{k=1}^{N} \mathbf{m}_k^b \otimes \mathbf{I} \tag{3.150}$$

$$\mathbf{H}_{Tm_k^b} = 2\left[\left(\mathbf{m}_k^b \otimes I\right)\mathbf{T} - \mathbf{I} \otimes \left(\mathbf{u}_k - \mathbf{T}\mathbf{m}_k^b\right)\right] \tag{3.151}$$

[10] Notice the presence of three typos in the equation equivalent to (3.144) in the original paper, i.e., a misplaced transpose sign and the dimensions of the 6×1 matrices.

$$\mathbf{H}_{hh} = 2N\mathbf{I} \tag{3.152}$$

$$\mathbf{H}_{hm_k^b} = 2\mathbf{T} \tag{3.153}$$

$$\mathbf{H}_{m_k^b m_k^b} = 2\mathbf{T}^T\mathbf{T} + 2\lambda_k\mathbf{I} \tag{3.154}$$

$$\mathbf{H}_{m_k^b \lambda_k} = 2\mathbf{m}_k^b \tag{3.155}$$

where

$$\mathbf{u}_k \triangleq \mathbf{y}_k - \mathbf{h} \tag{3.156}$$

After the estimation convergence, corrected magnetometer measurements can be achieved by substituting the estimated $\mathbf{R}$ (or $\mathbf{T}$) and $\mathbf{h}$ in (3.127) and solving for $\mathbf{m}^b$.

Lastly, and for comparison purposes with the other methods, we shall find the OML's estimated error parameters in terms of the previously defined global variables. The biases $\boldsymbol{c}_b$ are simply equal to $\mathbf{h}$. In contrast, finding C_s and C_m from $\mathbf{T}$ is not trivial (as C_sC_m has been defined as a lower triangular matrix, while $\mathbf{T}$, an upper triangular one), and actually requires the knowledge of the real (not only estimated) error parameters. Therefore, even though not necessary in a real application, this transformation is derived here for the sake of clear comparison between methods. The first step is to compute the following intermediate estimated matrix.

$$M' = \frac{\mathbf{T}}{m_t} \tag{3.157}$$

Next, we use the modified Gram-Schmidt (see Appendix B for details) decomposition algorithm described by Stewart (1998), and denoted here as $mgs(.)$, upon the true error matrix $M_t = C_sC_m$, in order to extract the following orthogonal matrices:

$$Q = mgs(M_t^{-1}) \tag{3.158}$$

$$q = mgs(M_t^T) \tag{3.159}$$

Next, we find M:

$$M = M' Q^T q^T \tag{3.160}$$

And from M:

$$\rho = \arctan \frac{M_{2,1}}{M_{2,2}} \tag{3.161}$$

$$\phi = \arctan \frac{M_{3,1}}{M_{3,3}} \tag{3.162}$$

$$\lambda = \arctan \left(\frac{M_{3,2}}{M_{3,1}} \right) \sin \phi \tag{3.163}$$

$$C_s = \begin{bmatrix} M_{1,1} & 0 & 0 \\ 0 & \frac{M_{2,1}}{\sin \rho} & 0 \\ 0 & 0 & \frac{M_{3,2}}{\sin \lambda} \end{bmatrix} \tag{3.164}$$

The variables equivalency are summarized in Table 3.5.

Table 3.5 – Input and output variables equivalency for the OML method.

Local variables	Global equivalent	Type (I/O)	Definition
$\mathbf{y}$	$\tilde{\boldsymbol{m}}$	I	Measured magnetic field density
$\mathbf{m}^b$	$(C_b^s)^T \boldsymbol{m}$	I	Uncorrupted magnetic field density in body-frame
$\mathbf{e}$	$\boldsymbol{c}_\mu$	I	Measurement noise
$\mathbf{h}$	$\boldsymbol{c}_b$	O	Biases
$\mathbf{R}^{-1}$	$(C_s C_m)^T q^T Q^T$	O	Misalignments and scale factors

3.4.6 MAG.I.C.AL Method

Lastly, we mathematically describe the MAGnetometer-Inertial sensors Calibration and ALignment (MAG.I.C.AL) method presented by Papafotis and Sotiriadis (2019), which uses an iterative process with a linear least-squares initial estimate. The mathematical model used to describe the corrupted measurements is the same as the previous ones, but is formulated in terms of the following local variables, as in the work by Papafotis and Sotiriadis (2019):

$$y_m = T_m m + h_m + \varepsilon \tag{3.165}$$

where y_m is the measured magnetic field density vector, T_m is a 3×3 matrix containing a combination of the total scale factor, misalignment error and soft iron, m the true magnetic field density vector, h_m is the bias vector, and ε is the measurement noise, considered to be a zero mean random vector. The model (3.165) can be represented in matrix format as:

$$Y = LG + E \tag{3.166}$$

with

$$Y = \begin{bmatrix} y_{m1} & y_{m2} & \dots & y_{mN} \end{bmatrix} \tag{3.167}$$

$$L = \begin{bmatrix} T_m & h_m \end{bmatrix} \tag{3.168}$$

$$G = \begin{bmatrix} m_1 & m_2 & \dots & m_N \\ 1 & 1 & \dots & 1 \end{bmatrix} \tag{3.169}$$

$$E = \begin{bmatrix} \varepsilon_1 & \varepsilon_1 & \dots & \varepsilon_N \end{bmatrix} \tag{3.170}$$

where N is the total number of available measurements.

The calibration algorithm is based on the minimization of the following penalty function:

$$J = \sum_{k=1}^{N} \left[|y_{mk} - T_m m_k - h_m|^2 + \lambda \left(|m_k|^2 - 1 \right)^2 \right] \tag{3.171}$$

where k is the measurement index and λ is the Lagrange coefficient (positive constant), which is usually selected to be in the order of $|T_m|$.

The methodology is divided by the authors into six steps:

Step 1: Initialize m_k for $k = 1 \dots N$, as:

$$m_k = \frac{y_{mk}}{|y_{mk}|} \tag{3.172}$$

Step 2: Solve for L using the least-squares formulation:

$$L = YG^T(GG^T)^{-1} \tag{3.173}$$

Step 3: Extract T_m and h_m from L.

Step 4: Calculate $\tilde{m}_k$ for $k = 1 \ldots N$:

$$\tilde{m}_k = T_m^{-1}(y_{mk} - h_m) \tag{3.174}$$

Step 5: Update G using:

$$m_k = \frac{\tilde{m}_k}{||\tilde{m}_k||} \tag{3.175}$$

Step 6: Calculate J using (3.171).

Step 7: Repeat steps 2-6 until J reaches a predetermined stop condition.

Lastly, and for the purpose of comparison between methods, we present a conversion of the local T_m and h_m in terms of the global parameters for scale factors, misalignments and biases.

$$\boldsymbol{c}_b = h_m \tag{3.176}$$

$$M = \frac{T_m}{m_t} \tag{3.177}$$

$$\rho = \arctan\frac{M_{2,1}}{M_{2,2}} \tag{3.178}$$

$$\phi = \arctan\frac{M_{3,1}}{M_{3,3}} \tag{3.179}$$

$$\lambda = \arctan\left(\frac{M_{3,2}}{M_{3,1}}\right)\sin\phi \tag{3.180}$$

$$\mathbf{C}_s = \begin{bmatrix} M_{1,1} & 0 & 0 \\ 0 & \frac{M_{2,1}}{\sin\rho} & 0 \\ 0 & 0 & \frac{M_{3,2}}{\sin\lambda} \end{bmatrix} \tag{3.181}$$

The variables equivalency are summarized in Table 3.6.

Table 3.6 – Input and output variables equivalency for the MAG.I.C.AL method.

Local variables	Global equivalent	Type (I/O)	Definition
y_m	$\tilde{\boldsymbol{m}}$	I	Measured magnetic field density
m	$\boldsymbol{m}/\|\|\boldsymbol{m}\|\|$	I	Uncorrupted unitary magnetic field density vector in sensor-frame
ε	$\boldsymbol{c}_\mu$	I	Measurement noise
T_m	$C_s C_m m_t$	O	Error matrix
h_m	$\boldsymbol{c}_b$	O	Biases

4 TWO-DIMENSIONAL NUMERICAL AND ANALYTICAL SOLUTIONS FOR THE EXTENDED TWO-STEP CALIBRATION METHODOLOGY

In this chapter, novel numerical and analytical solutions for the two-dimensional ETS calibration method (FOSTER; ELKAIM, 2008) are presented, with a meticulous derivation. Simulated and real data experiments are performed in order to validate the solutions.

4.1 Numerical Solution

As mentioned in Section 3.4.2.1, the solutions for the two-dimensional error parameters b_x, b_y, s_x, s_y and ρ are not provided by Foster and Elkaim (2008), but since they are a function of the estimated parameters A, B, C, D, E and F, they can be derived.

First, let us rewrite the equations (3.44) to (3.47) that establish the relationship between the aforementioned parameters, in terms of the previously defined global variables:

$$\tilde{m}_x = s_x m_x + b_x \tag{4.1}$$

$$\tilde{m}_y = s_y(m_y \cos\rho + m_x \sin\rho) + b_y \tag{4.2}$$

$$A\tilde{m}_x^2 + B\tilde{m}_x\tilde{m}_y + C\tilde{m}_y^2 + D\tilde{m}_x + E\tilde{m}_y + F = 0 \tag{4.3}$$

$$m_x^2 + m_y^2 = m_h^2 \tag{4.4}$$

We begin the manipulation by solving (4.1) for m_x and plugging it into (4.2), so we can solve it for m_y, in terms of $\tilde{m}_x$ and $\tilde{m}_y$ only:

$$m_x = \frac{\tilde{m}_x - b_x}{s_x} \tag{4.5}$$

$$m_y = -\frac{b_y - \tilde{m}_y + \dfrac{[s_y \sin(\rho)(\tilde{m}_x - b_x)]}{s_x}}{s_y \cos\rho} \tag{4.6}$$

which is rearranged as:

$$m_y = -\frac{s_x b_y - s_x \tilde{m}_y + s_y \sin(\rho)(\tilde{m}_x - b_x)}{s_x s_y \cos\rho} \tag{4.7}$$

Next, we plug (4.5) and (4.7) into (4.4), yielding:

$$\left[\frac{\tilde{m}_x - b_x}{s_x}\right]^2 + \left[-\frac{s_x b_y - s_x \tilde{m}_y + s_y \sin(\rho)(\tilde{m}_x - b_x)}{s_x s_y \cos\rho}\right]^2 = m_h^2 \tag{4.8}$$

In order to find the ellipse parameters A, B, C, D, E and F, we expand (4.8) and compare the result with (4.3). In particular, in order to find F in terms of b_x, b_y, s_x, s_y and ρ, one looks for the expanded terms in (4.8) that multiply neither $\tilde{m}_x$ nor $\tilde{m}_y$, which yields:

$$F = \frac{\left(b_y - \frac{s_y b_x \sin\rho}{s_x}\right)}{s_y^2 \cos^2\rho} + \frac{b_x^2}{s_x^2} - m_h^2 \tag{4.9}$$

The parameters A and D, which multiply $\tilde{m}_x^2$ and $\tilde{m}_x$ in (4.3), respectively, can be found by substituting $\tilde{m}_y$ by zero in (4.8) and subtracting F from it, yielding:

$$A = -\frac{1}{s_x^2(\sin^2\rho - 1)} \tag{4.10}$$

$$D = \frac{2 s_y b_x - 2 s_x b_y \sin\rho}{s_x^2 s_y (\sin^2\rho - 1)} \tag{4.11}$$

The same process is repeated for C and E by substituting $\tilde{m}_x$ by zero in (4.8) and subtracting F, producing:

$$C = -\frac{1}{s_y^2(\sin^2\rho) - 1} \tag{4.12}$$

$$E = \frac{s_x b_y - 2 s_y b_x \sin\rho}{s_x s_y^2 (\sin^2\rho - 1)} \tag{4.13}$$

The only parameter left is B, which is found by subtracting the already known parameters from (4.8), yielding:

$$B = \frac{2\sin\rho}{s_x s_y (\sin^2\rho - 1)} \tag{4.14}$$

Even though there are six parameters in (4.3), only five are necessary to characterize the ellipse. Therefore, the ETS methodology (FOSTER; ELKAIM, 2008) only estimates five

auxiliary parameters. There are many ways to rearrange (4.3) in order to achieve that. Here, we follow the same as in the work by Foster and Elkaim (2008):

$$\frac{A}{C}\tilde{m}_x^2 + \frac{B}{C}\tilde{m}_x\tilde{m}_y + \tilde{m}_y^2 + \frac{D}{C}\tilde{m}_x + \frac{E}{C}\tilde{m}_y + \frac{F}{C} = 0 \tag{4.15}$$

Therefore, the parameters estimated via the least-squares relate to the ellipse parameters as in (3.50):

$$\boldsymbol{X}_{2D} = \begin{bmatrix} x_{2D_1} \\ x_{2D_2} \\ x_{2D_3} \\ x_{2D_4} \\ x_{2D_5} \end{bmatrix} = \begin{bmatrix} \frac{A}{C} \\ \frac{B}{C} \\ \frac{D}{C} \\ \frac{E}{C} \\ \frac{F}{C} \end{bmatrix} \tag{4.16}$$

For the sake simplicity, the subscripts $_{2D}$ in x_{2D_1}, x_{2D_2}, x_{2D_3}, x_{2D_4} and x_{2D_5} are omitted throughout this chapter, yielding, x_1, x_2, x_3, x_4 and x_5, respectively. However, these estimates shall not be confused with those from three-dimensional calibration procedures.

Finally, substituting (4.9) to (4.14) into the right hand side of (4.16) allows us to numerically solve (4.16) for s_x, s_y, b_x, b_y and ρ with computational aid like MATLAB *solve* function.

4.2 Analytical Solution

Despite the appropriateness of the numerical solution derived above, real-time magnetometer calibration would be further benefited from its analytical counterpart (if existent), especially in situations with limited computational capabilities. In order to derive an analytical solution for the error parameters s_x, s_y, b_x, b_y and ρ from the two-dimensional ETS estimated $\boldsymbol{X}_{2D}$, we need a geometrical understanding of (4.15), which is the general equation for a conic section, particularly a shifted, rotated ellipse (Fig. 3.2).

4.2.1 Biases

From a geometrical perspective, the biases b_x and b_y are the ellipse's offset from the origin. Therefore, by calculating the center of the ellipse (4.15), we also calculate the biases. Since (4.15) describes an ellipse with a symmetric shape, if we draw a line between $\tilde{m}_x$ maxima

and minima, and another line between $\tilde{m}_y$ maxima and minima, the two lines intersect at the center of the ellipse (Fig. 4.1).

Figure 4.1 – Partial derivative functions intersecting at the center of the ellipse.

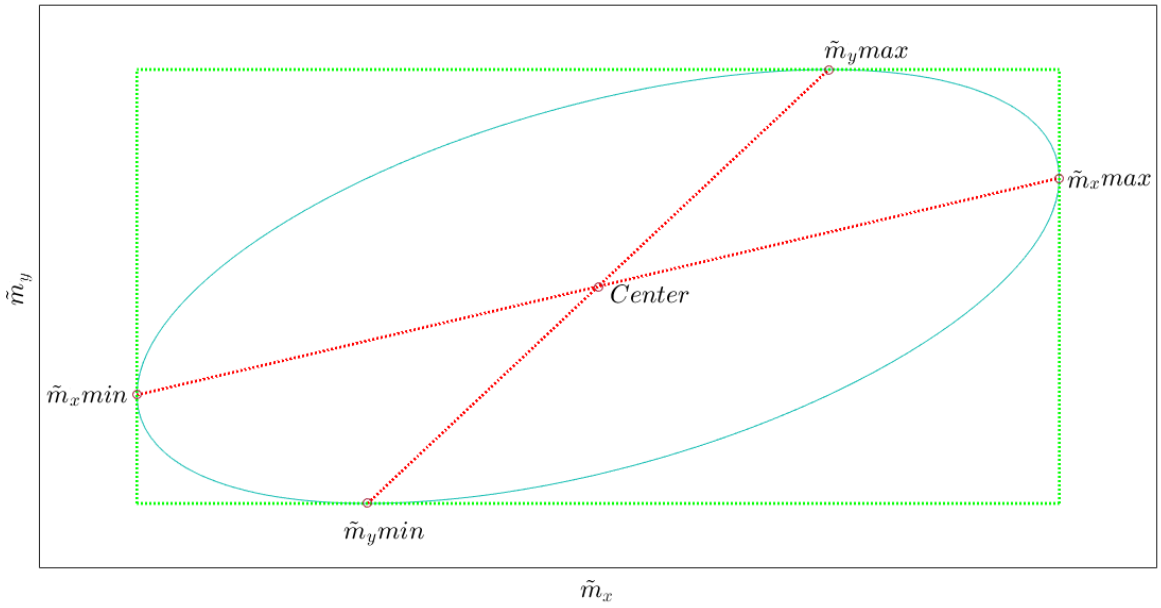

Source: Author

The functions that intersect the points of maxima and minima $\tilde{m}_x max$ and $\tilde{m}_x min$, and $\tilde{m}_y max$ and $\tilde{m}_y max$ can be derived by taking the partial derivatives of (4.15). Let us first rewrite (4.15) in terms of the estimated parameters $\boldsymbol{X}_{2D}$:

$$Q(\tilde{m}_x, \tilde{m}_y) = x_1\tilde{m}_x^2 + x_2\tilde{m}_x\tilde{m}_y + \tilde{m}_y^2 + x_3\tilde{m}_x + x_4\tilde{m}_y + x_5 = 0 \tag{4.17}$$

The partial derivatives of (4.17) with respect to $\tilde{m}_x$ and $\tilde{m}_y$ are expressed as:

$$\frac{\partial Q}{\partial \tilde{m}_x} = 2x_1\tilde{m}_x + x_2\tilde{m}_y + x_3 \tag{4.18}$$

$$\frac{\partial Q}{\partial \tilde{m}_y} = x_2\tilde{m}_x + 2\tilde{m}_y + x_4 \tag{4.19}$$

The points $\tilde{m}_x max$ and $\tilde{m}_x min$, and $\tilde{m}_y max$ and $\tilde{m}_y min$ can be calculated by solving (4.18) and (4.19), when $\frac{\partial Q}{\partial \tilde{m}_x}$ and $\frac{\partial Q}{\partial \tilde{m}_y}$ intersect $Q(\tilde{m}_x, \tilde{m}_y)$, respectively.

Finally, we can find the biases solving a system of equations with $\frac{\partial Q}{\partial \tilde{m}_x} = 0$ and $\frac{\partial Q}{\partial \tilde{m}_y} = 0$, where b_x and b_y are the solutions for $\tilde{m}_x$ and $\tilde{m}_y$, respectively:

$$\tilde{m}_x = -\frac{2x_3 - x_2x_4}{-x_2^2 + 4x_1} \equiv b_x \tag{4.20}$$

$$\tilde{m}_y = -\frac{2x_1x_4 - x_2x_3}{-x_2^2 + 4x_1} \equiv b_y \tag{4.21}$$

The analytical biases solutions of equations (4.20) and (4.20) can be verified by substituting the ETS estimates x_1, x_2, x_3 and x_4 by their counterparts of equation (4.16), as:

$$-\frac{2x_3 - x_2x_4}{-x_2^2 + 4x_1} = -\frac{2\frac{D}{C} - \frac{B}{C}\frac{E}{C}}{-\left(\frac{B}{C}\right)^2 + 4\frac{A}{C}} \tag{4.22}$$

$$-\frac{2x_1x_4 - x_2x_3}{-x_2^2 + 4x_1} = -\frac{2\frac{A}{C}\frac{E}{C} - \frac{B}{C}\frac{D}{C}}{-\left(\frac{B}{C}\right)^2 + 4\frac{A}{C}} \tag{4.23}$$

and substituting the terms A, B, C, D and E of the resulting equations (4.22) and (4.23) by their analytical descriptions in terms of b_x, b_y, s_x, s_y and ρ as presented in equations (4.10) to (4.14). After simplification, only b_x and b_y are left on the right hand sides of equations (4.24) and (4.25), respectively, as follows:

$$-\frac{2x_3 - x_2x_4}{-x_2^2 + 4x_1} = b_x \tag{4.24}$$

$$-\frac{2x_1x_4 - x_2x_3}{-x_2^2 + 4x_1} = b_y \tag{4.25}$$

which proves the adequacy of (4.20) and (4.21).

4.2.2 Misalignment

Once analytical expressions have been derived for the biases, the misalignment ρ can be described in terms of $\boldsymbol{X}_{2D}$ via algebraic manipulation:

$$\frac{x_1}{x_2^2} = \frac{\frac{A}{C}}{\frac{B^2}{C^2}} = \frac{AC}{B^2} \tag{4.26}$$

Next, we substitute A, B and C in (4.26) by their analytical descriptions of (4.10), (4.14) and (4.12), respectively, and simplify the result, yielding:

$$\frac{x_1}{x_2^2} = (4\sin^2\rho)^{-1} \tag{4.27}$$

Finally, solving (4.27) for $\sin^2\rho$ yields:

$$\sin^2\rho = \frac{x_2^2}{4x_1} \tag{4.28}$$

Computing $cos^2\rho$ from (4.28), and using it to determine $\tan\rho$ allows an explicit analytical solution for ρ to be derived, namely [1]:

$$\cos^2\rho = 1 - \sin^2\rho = 1 - \frac{x_2^2}{4x_1} \tag{4.29}$$

$$\tan^2\rho = \frac{\sin^2\rho}{\cos^2\rho} = \frac{{x_2}^2}{4x_1 - {x_2}^2} \tag{4.30}$$

$$\tan\rho = \sqrt{\frac{{x_2}^2}{4x_1 - {x_2}^2}} \tag{4.31}$$

$$\rho = \arctan\left(\sqrt{\frac{{x_2}^2}{4x_1 - {x_2}^2}}\right) \tag{4.32}$$

4.2.3 Scale Factors

Once we have analytically determined b_x, b_y and ρ in terms of $\boldsymbol{X}_{2D}$, we substitute them in (4.9) to (4.14) and arrange a system equations as in (4.16), with five equations and two unknowns: s_x and s_y. The solution is then:

$$s_x = \pm 2\frac{\sqrt{x_1\left(x_5x_2^2 - x_2x_3x_4 + x_3^2 + x_1x_4^2 - 4x_1x_5\right)}}{\sqrt{x_1}\left(-m_h x_2^2 + 4m_h x_1\right)} \tag{4.33}$$

$$s_y = \pm 2\frac{\sqrt{x_1\left(x_5x_2^2 - x_2x_3x_4 + x_3^2 + x_1x_4^2 - 4x_1x_5\right)}}{-m_h x_2^2 + 4m_h x_1} \tag{4.34}$$

As by definition, s_x and s_y are positive scalars (with value close to the unity), the $\pm$ sign in (4.33) and (4.34) should be selected accordingly, so that the latter requirement is fulfilled.

[1] We can use the arctan function in (4.32) because, by definition, ρ is a small angle, i.e., it lies in the first or fourth quadrant.

4.3 Simulated Experiments

In this section, we perform the two-dimensional ETS calibration of magnetometers using simulated data, with both the numerical and analytical solutions, and their performance is compared. The simulations are presented with two different approaches. The first is an example of a consumer-grade magnetometer calibration, where the error parameters corrupting the measurements were selected in accordance with a regular consumer-grade sensor, like the Honeywell HMC5883L used in future sections of this work for real data experiments. The second is a Monte Carlo analysis performed in order to statistically characterize the solutions.

4.3.1 Calibration Example

In this scenario, a 2D magnetometer calibration was performed. As mentioned before, this version of the technique is useful when only two axes are available (or required). In this case, sensors must be horizontally leveled and are rotated about the z-axis. Accordingly, 3600 samples of corrupted magnetometer measurements were generated at frequency of 15 Hz, while rotating in yaw with constant rate of 10 deg/s ; the error parameters corrupting the signal are given in the first two columns of Table 4.1. Noise was defined as a zero-mean Gaussian distribution with variance of 2 mG^2, as estimated from stationary measurements, throughout this entire section. Figure 4.2 shows the corrupted and corrected data, and a reference circle with radius m_h, computed via the WMM[2]. Notice that the corrupted data assume the shape of a shifted, rotated ellipse, while the calibrated data lies on top of the expected circle. The calibration was conducted via both the numerical and analytical solutions, with approximately equal results. The difference between the estimates was in the order of 10^{-15} mG for the biases, 10^{-17} for the scale factors and 10^{-15} deg for the misalignment. Therefore, the analytical and numerical solutions are represented as the same in Table 4.1 (column 3) and Figure 4.2.

The correction displayed in Figure 4.2 was preceded by the error parameters estimation, whose results are given in Table 4.1. As can be inferred, satisfactory accuracy was obtained with ETS method for two-dimensional case (see fourth column of Table 4.1).

[2] Notice that the calibration is model dependent. Therefore, its performance is sensitive to model errors or inaccuracies. In addition, using other models may result in different results.

Table 4.1 – Two-dimensional calibration results for simulated data

Error component	Original	Estimated	Error	Unit
b_x	-45	-44.9938	6.2212×10^{-3}	mG
b_y	10	9.9994	-5.9245×10^{-4}	mG
s_x	0.98	0.9801	9.3635×10^{-5}	unitless
s_y	1.09	1.0898	-2.0603×10^{-4}	unitless
ρ	-6	-6.0305	-3.0488×10^{-2}	deg

Figure 4.2 – Corrupted and corrected data, in red and green, respectively. In addition, the expected uncorrupted circle is plotted in black.

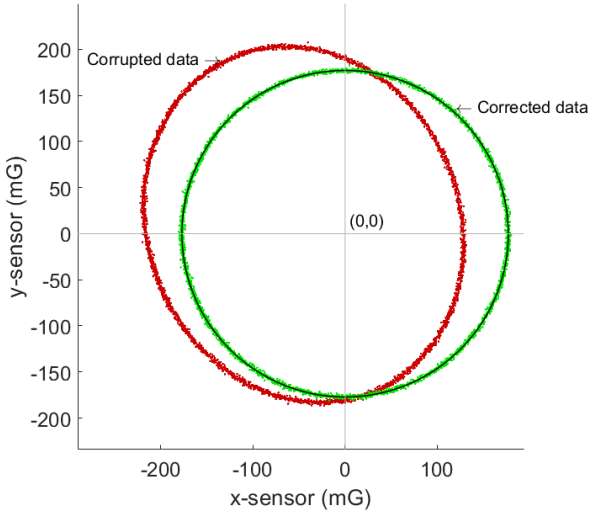

4.3.2 Monte Carlo Analysis

A Monte Carlo analysis was conducted in order to identify the estimation error distributions for each error parameter for the two-dimensional ETS analytical and numerical solutions. The data was generated throughout 5000 runs, each containing 2500 samples, where the error parameters were randomly selected in each run, following normal distributions as expressed in Table 4.2.

The resulting histograms of each estimation error are plotted in Figures 4.3 to 4.7.

Table 4.2 – Error parameters used to generate the data for the Monte Carlo analysis.

Error Parameter	Mean	Standard Deviation	Unit
b_x	0	50	mG
b_y	0	50	mG
s_x	1	0.1	unitless
s_y	1	0.1	unitless
ρ	0	1	deg

Figure 4.3 – Histograms of the b_x estimation error, with numerical and analytical solutions, resulting from the Monte Carlo Analysis.

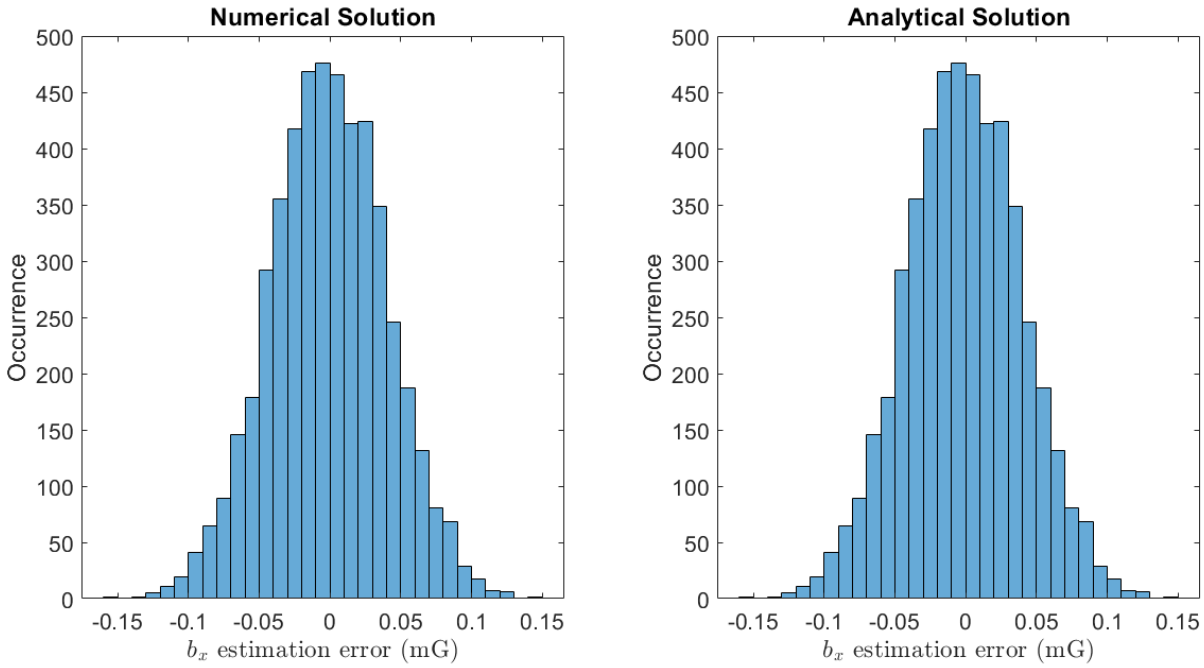

Source: Author

Figure 4.4 – Histograms of the b_y estimation error, with numerical and analytical solutions, resulting from the Monte Carlo Analysis.

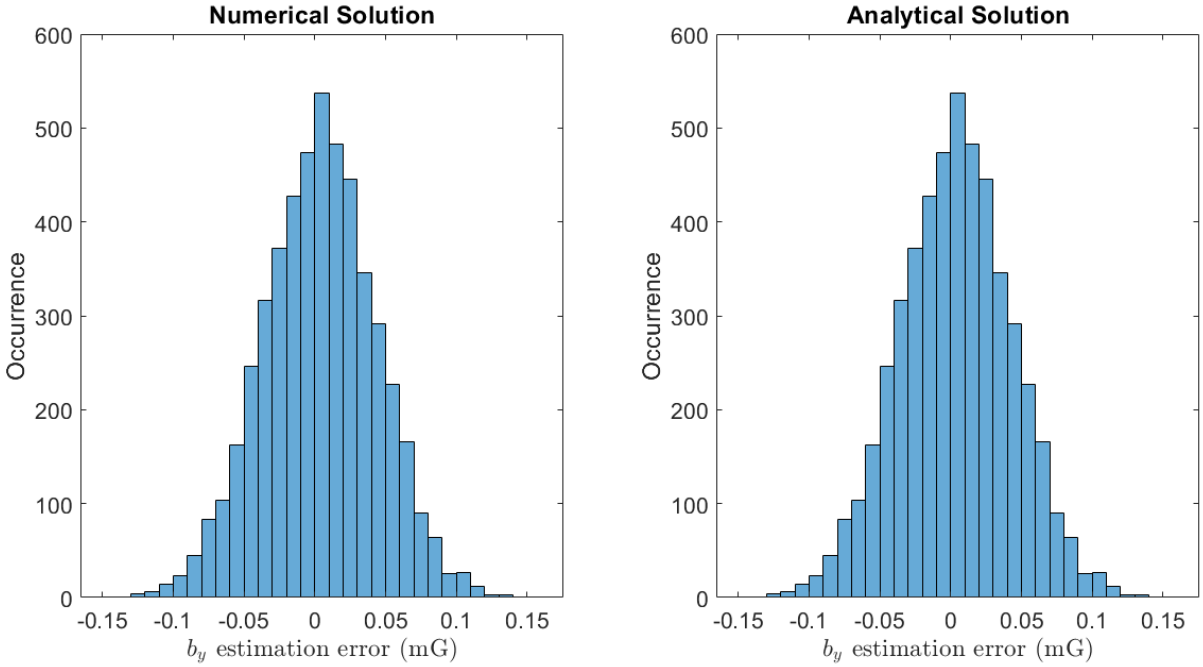

Source: Author

Figure 4.5 – Histograms of the s_x estimation error, with numerical and analytical solutions, resulting from the Monte Carlo Analysis.

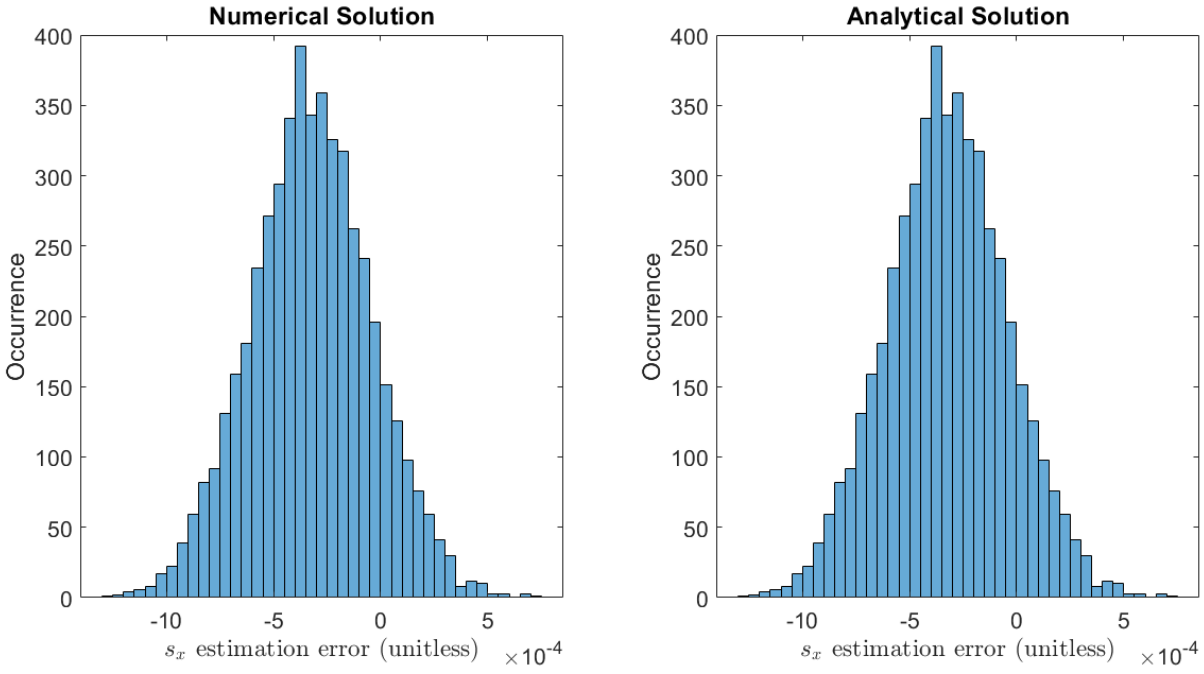

Source: Author

Figure 4.6 – Histograms of the s_y estimation error, with numerical and analytical solutions, resulting from the Monte Carlo Analysis.

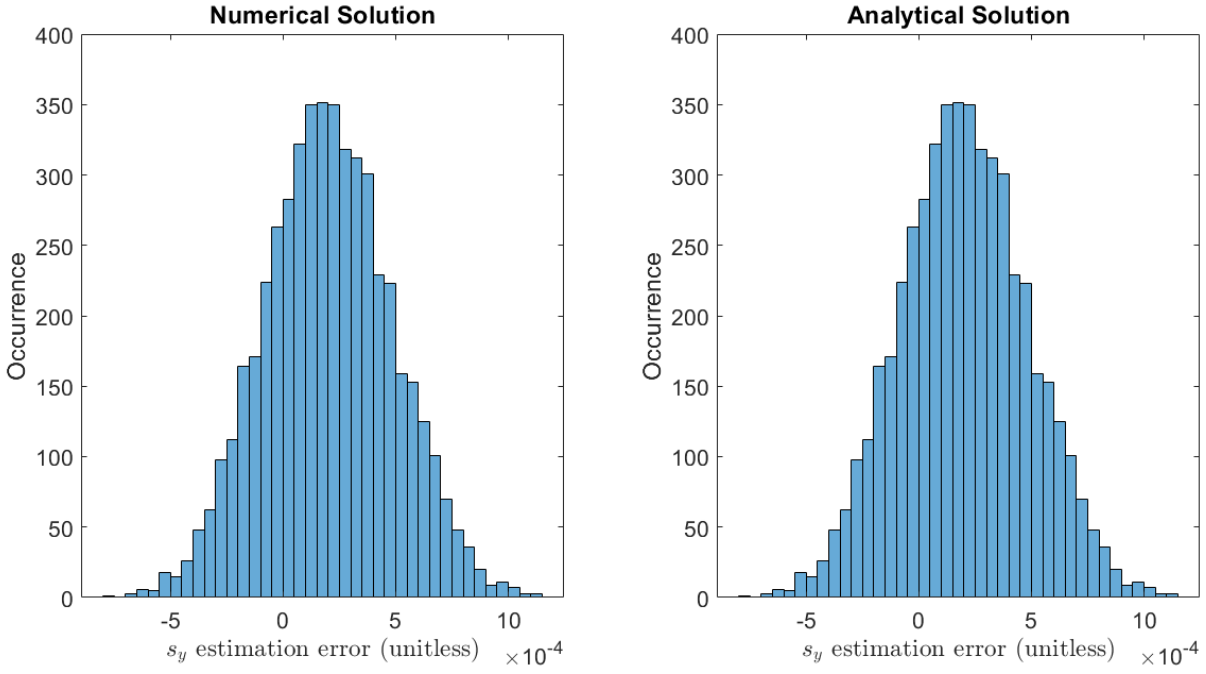

Source: Author

Figure 4.7 – Histograms of the ρ estimation error, with numerical and analytical solutions, resulting from the Monte Carlo Analysis.

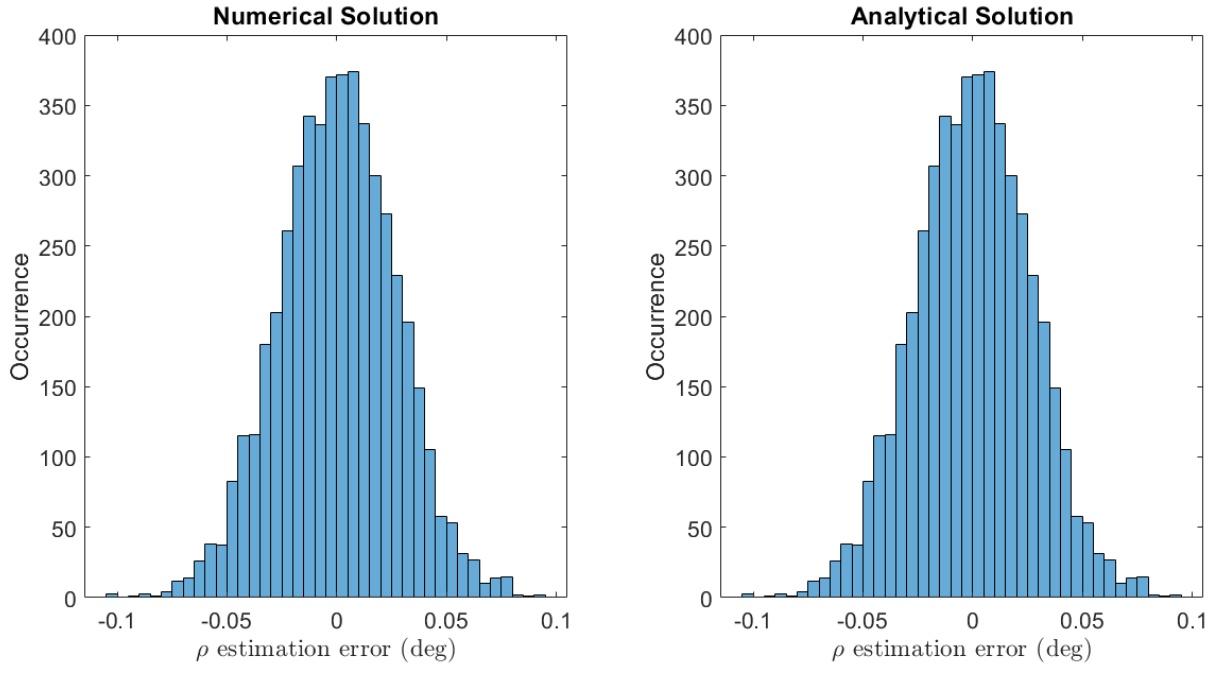

Source: Author

The identified estimation error for each parameter are characterized through their mean and standard deviation, as expressed in Table 4.3. Notice that the distributions identified for the analytical and the numerical solutions are approximately the same, where the difference in mean is in the order of 10^{-20} to 10^{-17} and 0 to 10^{-17} in standard deviation (Table 4.4), confirming the adequacy of both for the purpose of two-dimensional magnetometer calibration.

Table 4.3 – Errors in estimation identified via the Monte Carlo Analysis.

Error Parameter	Mean	Standard Deviation	Unit
b_x	-1.0977×10^{-3}	4.0882×10^{-2}	mG
b_y	3.6401×10^{-3}	3.9978×10^{-2}	mG
s_x	-3.2319×10^{-4}	2.8199×10^{-4}	unitless
s_y	2.0128×10^{-4}	2.8483×10^{-4}	unitless
ρ	7.8067×10^{-6}	4.6550×10^{-4}	deg

Table 4.4 – Estimation error difference between analytical and numerical solutions.

Error Parameter	Mean	Standard Deviation	Unit
b_x	-4.4235×10^{-17}	0	mG
b_y	8.2399×10^{-17}	2.7755×10^{-17}	mG
s_x	-2.3581×10^{-17}	2.2768×10^{-18}	unitless
s_y	2.3879×10^{-17}	-2.4394×10^{-18}	unitless
ρ	5.2516×10^{-20}	0	deg

In conclusion, both solutions can be used interchangeably, without significant loss of accuracy, as shown in Table 4.4. On the other hand, as displayed in Table 4.3, the scale factors estimation error means (s_x and s_y) are not centered around zero, as ideally expected for accuracy. This characteristic can be investigated in order to further improve the estimation, considering the distribution characteristics obtained here.

Even though the numerical and analytical solutions are very similar in terms of accuracy and precision, they differ dramatically with respect to computational effort. An analysis of such matter is provided for the three-dimensional solutions in the Chapter 5.

4.4 Real Data Experiments

In this section, we perform the calibration of a Honeywell HMC5883L magnetometer, which has a built-in Analog-to-Digital Converter that offers a 12-bit digital resolution. Conversely, there is a trade-off between magnetic field resolution and measurement range. The default

option, used throughout this work, is 0.92 mG/LSb and $\pm$1300 mG, respectively. The experiments were conducted in two different scenarios: in the first, the sensor was rotated by hand, while in the second, a robot arm Motoman MH5 was used. Notice that, in this section, we are only using the two-dimensional ETS analytical calibration solution, since it requires less computational effort and is more suitable for embedded applications. These data sets were meant to represent a restricted scenario where only limited motion is possible, such as in a land, or maritime vehicle application. In this case, the vehicle was supposed not being able to perform rotations around its x or y axes. Even though this is beyond the scope defined by the authors, we also tested the two-dimensional ETS methodology for a scenario where the vehicle is not precisely leveled, as eventually found in real in-field applications.

4.4.1 Manual Calibration

In this section, the data were acquired while the triaxial magnetometer was rotated by hand on top of a regular table. The sampling frequency was also set to 15 Hz, and a total of 3600 samples were collected. Figure 4.8 shows the sampled data and a reference sphere of radius m_t, computed via WMM.

Figure 4.8 – Corrupted, restricted measurements, in red, plotted with the reference sphere of radius m_t, computed via the WMM.

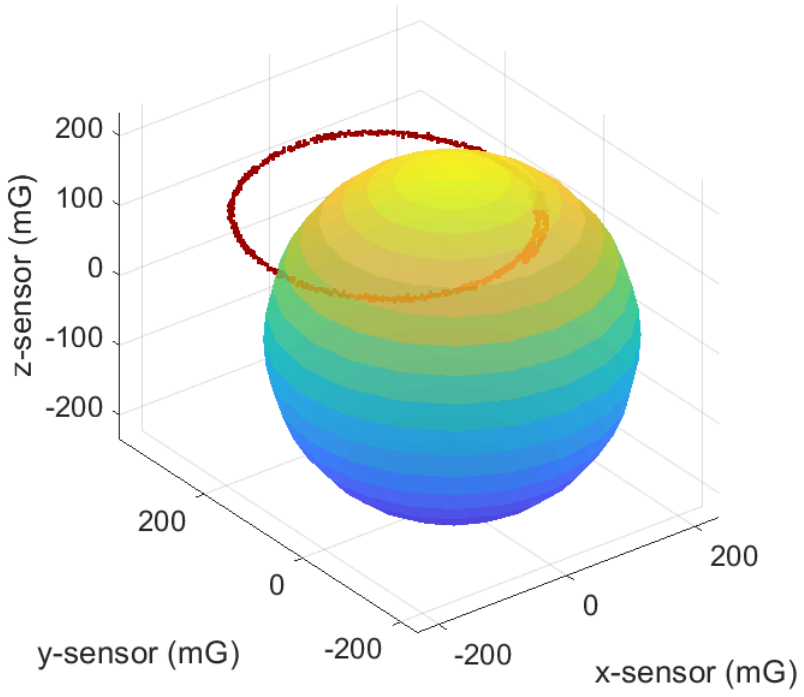

Source: Author

We assumed a two-dimensional magnetometer in the restricted scenario, not considering measurements from z-sensor, and conducted calibration using the two-dimensional ETS method via analytical solution. Figure 4.9 shows the 2D corrupted and corrected data plotted with the reference circle, and Table 4.5 contains the estimated parameters.

Table 4.5 – Calibration results for real data acquired while the sensor was rotated by hand.

Error component	2D Calibration	Unit
b_x	41.0439	mG
b_y	185.2486	mG
s_x	1.1050	unitless
s_y	1.0486	unitless
ρ	-2.4280	deg

Figure 4.9 – Corrupted and corrected measurements acquired manually, in red and green, respectively, for x- and y-sensors, plotted with the reference circle of radius m_h, in black.

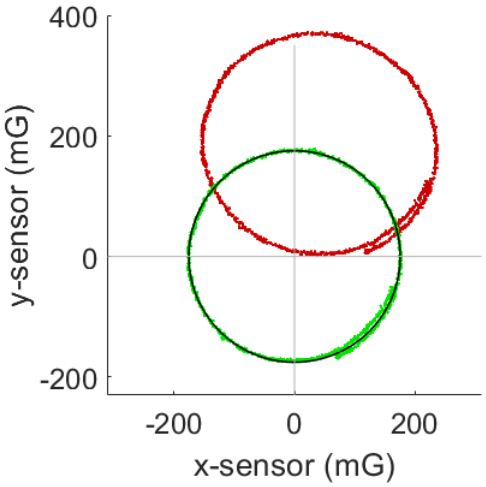

Source: Author

Notice that, after one complete turn, the plotted data do not overlap the first circle. This effect occurs due to non deterministic errors that appear during sensor use, like the in-run biases, which can be mitigated, for example, with posterior filtering. Despite the non deterministic errors affecting the data during calibration, the systematic errors were successfully estimated and corrected for, which resulted in a major improvement, as displayed in Figure 4.9.

4.4.2 Robot Arm Aided Calibration

Lastly, we performed the 2D calibration using ETS analytical solution and data acquired while the magnetometer was rotated with a robot arm Motoman MH5 (Figure 4.10). Again, the scenario is considered restricted, since even though there may be a three dimensional sensor, the rotation is only performed around the z-axis, which precludes 3D calibration. However, the scenario is not perfectly suitable for 2D calibration either, since leveling is not guaranteed. This experiment differs from the previous manual rotation because of the magnetic interference (hard and soft iron effects) possibly caused by the robot arm, which emulates practical applications where the sensors are mounted into a vehicle. This scenario can be considered a hostile environment for magnetometer calibration, since the magnetic interference magnitude may be as high as Earth's magnetic field density itself. The experimental setup is displayed in Figure 4.11, where the digitized data acquired via the HMC5883L is fed into an Arduino Mega, which is only responsible to deliver the measurements to a PC, for processing and storage.

Figure 4.10 – The robot arm Motoman MH5 used in the experiments, at the Federal University of Lavras.

Source: Author (picture by Gustavo Carvalho)

Figure 4.11 – Experimental setup with the Honeywell HMC5883L, the Arduino Mega used as a communication interface, and the robot arm Motoman MH5.

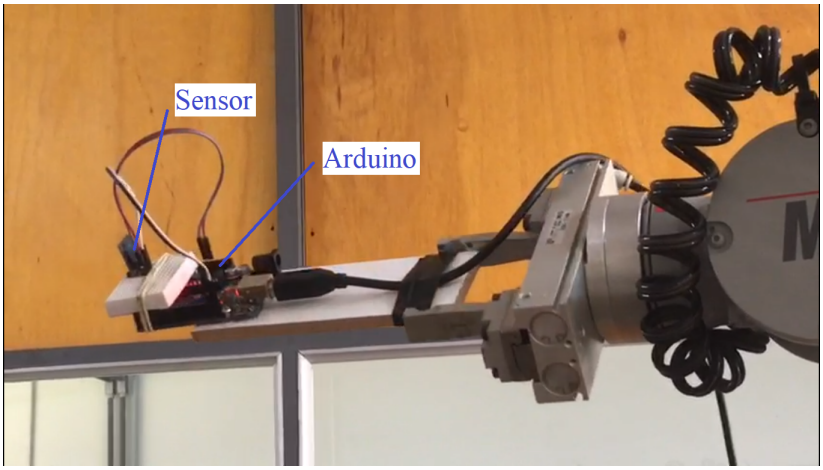

Source: Author (picture by Gustavo Carvalho)

Table 4.6 displays the error parameters estimated with the acquired data by the means of ETS analytical solutions. Notice that, even though the sensor is the same Honeywell HMC5883L used in the previous section, the errors have become larger. This occurs, as explained before, due to errors that change over time, namely run-to-run and in-run biases, and to intrinsic magnetic interference, as hard and soft iron effects. The magnetic interference caused by the Motoman MH5 has certainly degraded the raw measurements.

Table 4.6 – Calibration results for real data acquired while the sensor was rotated by the Motoman MH5

Error component	2D Calibration	Unit
b_x	-217.0674	mG
b_y	50.2206	mG
s_x	0.8180	unitless
s_y	0.8696	unitless
ρ	8.9781	deg

The measurements were corrected with respect to the estimated parameters of Table 4.6 and plotted around the reference circle of Figure 4.12, calculated via WMM.

Figure 4.12 – Corrupted and corrected measurements acquired with the aid of the robot arm, in red and green, respectively, for x- and y-sensors, plotted with the reference circle of radius m_h, in black.

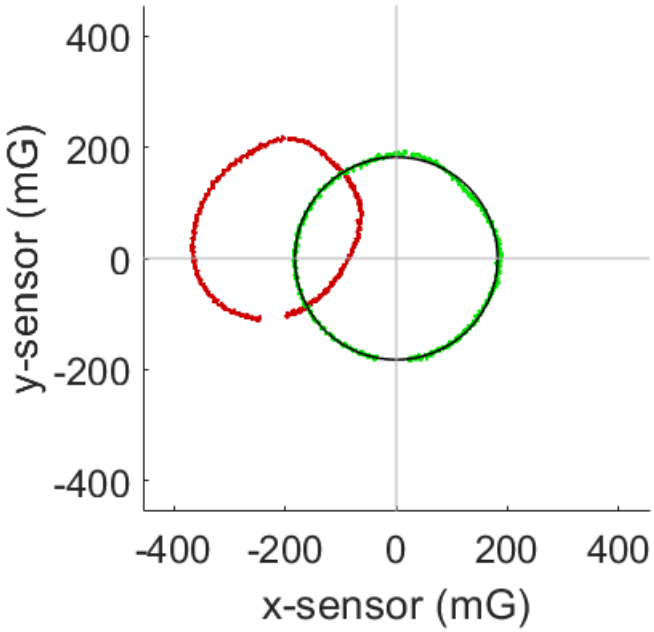

Source: Author

From Figure 4.12 we can see that the measurements do not complete a revolution (360 deg). This fact is due to a motion limitation in the Motoman MH5 joint. In addition, the corrupted measurements do not draw the exact shape of an ellipse, as expected, presenting an asymmetric shape. However, the calibration could be performed despite that, and the results proved the efficacy and robustness of the analytical solution derived for the two-dimensional ETS calibration method.

5 THREE-DIMENSIONAL NUMERICAL AND ANALYTICAL SOLUTIONS FOR THE EXTENDED TWO-STEP CALIBRATION METHODOLOGY

In this chapter, novel numerical and analytical solutions for the three-dimensional ETS calibration methodology (FOSTER; ELKAIM, 2008), described in Chapter 3, are presented. Firstly, the derivations that originated the solutions are introduced; in sequence, they are implemented and compared with other usual calibration techniques also presented in Chapter 3. The calibration techniques are implemented in simulated and real data scenarios.

5.1 Numerical Solution

As explained in Chapter 3, the ETS methodology proposed by Foster and Elkaim (2008) only estimates the auxiliary (or intermediate) ellipsoid parameters $(A, B, ..., J)$, and no conversion method is provided for recovering the sensors error parameters of interest $(b_x, b_y, ..., \lambda)$. Nevertheless, in order to calibrate a three-axial magnetometer, it is necessary to find the biases, scale factors, and misalignments, as discussed in the previous chapter for the two-dimensional case.

Aiming at deriving numerical and analytical solutions for the three-dimensional ETS method, let us first recall the equations presented in Chapter 3 for the estimated ellipsoid (3.56), the error model (3.45), (3.46), (3.54), and the total magnetic flux density magnitude (3.55), in terms, now, of the previously defined global variables:

$$A\tilde{m}_x^2 + B\tilde{m}_x\tilde{m}_y + C\tilde{m}_x\tilde{m}_z + D\tilde{m}_y^2 + E\tilde{m}_y\tilde{m}_z + F\tilde{m}_z^2 + G\tilde{m}_x + H\tilde{m}_y + I\tilde{m}_z + J = 0, \tag{5.1}$$

$$\tilde{m}_x = s_x m_x + b_x \tag{5.2}$$

$$\tilde{m}_y = s_y(m_y \cos\rho + m_x \sin\rho) + b_y, \tag{5.3}$$

$$\tilde{m}_z = s_z(m_z \cos\phi \cos\lambda + m_x \sin\phi \cos\lambda + m_y \sin\lambda) + b_z \tag{5.4}$$

$$m_t^2 = m_x^2 + m_y^2 + m_z^2 \tag{5.5}$$

The first step is the same as performed in Chapter 4, i.e., solving (5.2) for m_x and (5.3) for m_y, yielding:

$$m_x = \frac{\tilde{m}_x - b_x}{s_x} \tag{5.6}$$

$$m_y = -\frac{s_x b_y - s_x \tilde{m}_y + s_y \sin\rho\,(\tilde{m}_x - b_x)}{s_x s_y \cos\rho} \tag{5.7}$$

The next step is to plug (5.6) and (5.7) into (5.4) and solve it for m_z, resulting in:

$$m_z = -\frac{b_z - \tilde{m}_z + s_z \left\{ \frac{\cos\lambda \sin\phi (\tilde{m}_x - b_x)}{s_x} - \frac{\sin\lambda \left[b_y - \tilde{m}_y + \frac{s_y \sin\rho (\tilde{m}_x - b_x)}{s_x} \right]}{s_y \cos\rho} \right\}}{s_z \cos\lambda \cos\phi} \tag{5.8}$$

Now that expressions for the true magnetic field densities m_x, m_y and m_z have been determined, we can plug them into (5.5), which is the equation of an sphere, yielding a rotated, shifted ellipsoid:

$$m_t^2 = \frac{(\tilde{m}_x - b_x)^2}{s_x^2} + \frac{\xi_1^2}{s_y^2 \cos^2\rho} + \frac{\left\{ b_z - \tilde{m}_z + s_z \left[\frac{\cos\lambda \cos\phi (\tilde{m}_x - b_x)}{s_x} - \frac{\sin\lambda \xi_1}{s_y \cos\rho} \right] \right\}^2}{s_z^2 \cos^2\lambda \cos^2\phi} \tag{5.9}$$

where

$$\xi_1 = -\tilde{m}_y + b_y + \frac{s_y \sin\rho\,(\tilde{m}_x - b_x)}{s_x} \tag{5.10}$$

In sequence, we can find $A, B, C, D, E, F, G, H, I$ and J in terms of the sought error parameters and the total magnetic field density magnitude, by comparing (5.9) with (5.1), and looking for the parameters that mutually multiply each combination of $\tilde{m}_x$, $\tilde{m}_y$ and $\tilde{m}_z$, as done for the two-dimensional case in Chapter 4, yielding:

$$A = \frac{1}{s_x^2} + \frac{\sin^2\rho}{s_x^2 \cos^2\rho} + \frac{\left(\frac{\cos\rho \sin\phi}{s_x} - \frac{\sin\lambda \sin\rho}{s_x \cos\rho} \right)^2}{\cos^2\lambda \cos^2\phi} \tag{5.11}$$

$$B = -\frac{2(\sin\rho \cos^2\lambda \cos^2\phi - \sin\rho \cos^2\lambda - \cos\rho \sin\lambda \sin\phi \cos\lambda + \sin\rho)}{s_x s_y \cos^2\lambda \cos^2\rho \cos^2\phi} \tag{5.12}$$

$$C = \frac{2(\sin\lambda\sin\rho - \cos\lambda\cos\rho\sin\phi)}{s_x s_z \cos^2\lambda\cos\rho\cos^2\phi} \tag{5.13}$$

$$D = \frac{s_x s_z(\cos^2\lambda\cos^2\phi + \sin^2\lambda)}{s_x s_y^2 s_z \cos^2\lambda\cos^2\rho\cos^2\phi} \tag{5.14}$$

$$E = -\frac{2\sin\lambda}{s_y s_z \cos^2\lambda\cos\rho\cos^2\phi} \tag{5.15}$$

$$F = \frac{1}{s_z\cos^2\lambda\cos^2\phi} \tag{5.16}$$

$$G = -\frac{2b_x}{s_x^2} + \frac{2\sin(\rho)\xi_2}{s_x s_y\cos^2\rho} + \frac{\left(\frac{\cos\lambda\sin\phi}{s_x} - \frac{\sin\lambda\sin\rho}{s_x\cos\rho}\right)\left[2b_z - 2s_z\left(\frac{b_x\cos\lambda\sin\phi}{s_x} + \frac{\sin\lambda\xi_2}{s_y\cos\rho}\right)\right]}{s_z\cos^2\lambda\cos^2\phi} \tag{5.17}$$

$$H = \frac{-2\xi_3}{s_x s_y^2 s_z\cos^2\lambda\cos^2\rho\cos^2\phi} \tag{5.18}$$

$$I = -2\frac{s_x(s_y b_z\cos\rho - s_z b_y\sin\lambda) + s_y s_z(b_x\sin\lambda\sin\rho - b_x\cos\lambda\cos\rho\sin\phi)}{s_x s_y s_z^2\cos^2\lambda\cos\rho\cos^2\phi} \tag{5.19}$$

$$J = -m_t^2 + \frac{b_x^2}{s_x^2} + \frac{\xi_4^2}{s_y^2\cos^2\rho} + \frac{\left[b_z - s_z\left(\frac{b_x\cos\lambda\sin\phi}{s_x} + \frac{\sin(\lambda)\xi_4}{s_y\cos\rho}\right)\right]^2}{s_z^2\cos^2\lambda\cos^2\phi} \tag{5.20}$$

where

$$\xi_2 = b_y - \frac{s_y b_x\sin\rho}{s_x} \tag{5.21}$$

$$\begin{gathered}\xi_3 = s_x s_z b_y(\sin^2\lambda + \cos^2\lambda\cos^2\phi) - s_x s_y b_z\cos\rho\sin\lambda - s_y s_z \\ b_x(\sin^2\lambda\sin\rho + \cos^2\lambda\cos^2\phi\sin\rho - \cos\lambda\cos\rho\sin\lambda\sin\rho)\end{gathered} \tag{5.22}$$

$$\xi_4 = b_y - \frac{s_y b_x\sin\rho}{s_x} \tag{5.23}$$

Finally, we rearrange the expressions for the ellipsoid parameters in order to match the estimated parameters as in (3.59):

$$\mathbf{X}_{3D} = \begin{bmatrix} x_{3D_1} \\ x_{3D_2} \\ x_{3D_3} \\ x_{3D_4} \\ x_{3D_5} \\ x_{3D_6} \\ x_{3D_7} \\ x_{3D_8} \\ x_{3D_9} \end{bmatrix} = \begin{bmatrix} \frac{A}{D} \\ \frac{B}{D} \\ \frac{C}{D} \\ \frac{E}{D} \\ \frac{F}{D} \\ \frac{G}{D} \\ \frac{H}{D} \\ \frac{I}{D} \\ \frac{J}{D} \end{bmatrix}, \tag{5.24}$$

For the sake of simplicity, the thee-dimensional ETS estimates x_{3D_1} to x_{3D_9} are written in this chapter simply as x_1 to x_9, but they shall not be confused with the estimates from previous chapters.

After the parameters $\mathbf{X}_{3D}$ are estimated via (3.62), they can be substituted in the left hand side of (5.24). Equations (5.11) to (5.23), in turn, can be substituted in the right hand side of (5.24), producing a system of equations with nine unknowns, i.e., s_x, s_y, s_z, b_x, b_y, b_z, ρ, ϕ and λ and nine equations that can be numerically solved resorting to computational aid (e.g., MATLAB's *solve* function).

5.2 Analytical Solution

In this section, we provide novel analytical solutions for the error parameters, i.e., biases, scale factors and misalignments, for the three-dimensional ETS calibration method (FOSTER; ELKAIM, 2008). In addition, we present the derivation of the formulas and a comparison with the analytical solution provided by Vasconcelos et al. (2011).

5.2.1 Biases

The analytical solution for the biases is based on the same rationale used in the two-dimensional analytical solution, that is, calculating the partial derivatives of the ellipsoid equation in terms of each corrupted measurement, and using the resulting functions in a system of equations, whose solution is the ellipsoid center, equivalent to the bias parameters. This concept

is geometrically explained in Figure 4.1, where we can see that the lines generated by the partial derivatives always cross the center of the ellipse due to the symmetry property of the ellipse. In the three-dimensional case, instead of two lines, we generate three planes that intersect at the center (Figure 5.1).

Figure 5.1 – Estimated ellipsoid plotted with the partial derivative planes that intersect at the center.

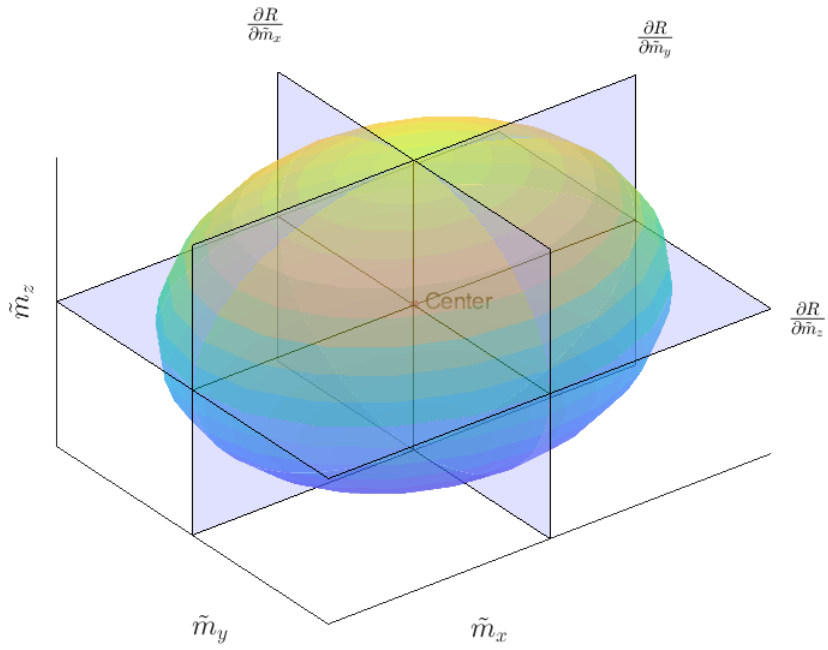

Let us start by restating the rearranged ellipsoid equation (5.1), whose parameters are the Least Squares solution $\mathbf{X}_{3D}$:

$$R(\tilde{m}_x,\tilde{m}_y,\tilde{m}_z) = x_1\tilde{m}_x^2 + x_2\tilde{m}_x\tilde{m}_y + x_3\tilde{m}_x\tilde{m}_z + \tilde{m}_y^2 + x_4\tilde{m}_y\tilde{m}_z + x_5\tilde{m}_z^2 + x_6\tilde{m}_x + x_7\tilde{m}_y + x_8\tilde{m}_z + x_9 = 0 \tag{5.25}$$

In sequence, we find the partial derivatives of $R(\tilde{m}_x,\tilde{m}_y,\tilde{m}_z)$ in terms of $\tilde{m}_x$, $\tilde{m}_y$ and $\tilde{m}_z$:

$$\frac{\partial R}{\partial \tilde{m}_x} = 2x_1\tilde{m}_x + x_2\tilde{m}_y + x_3\tilde{m}_z + x_6 \tag{5.26}$$

$$\frac{\partial R}{\partial \tilde{m}_y} = 2\tilde{m}_y + x_2\tilde{m}_x + x_4\tilde{m}_z + x_7 \tag{5.27}$$

$$\frac{\partial R}{\partial \tilde{m}_z} = x_3\tilde{m}_x + x_4\tilde{m}_y + 2x_5\tilde{m}_z + x_8 \tag{5.28}$$

Finally, the intersection of the planes (5.26), (5.27) and (5.28) creates a system of equations $\frac{\partial R}{\partial \tilde{m}_x} = \frac{\partial R}{\partial \tilde{m}_y} = \frac{\partial R}{\partial \tilde{m}_z} = 0$, whose solution, for $\tilde{m}_x$, $\tilde{m}_y$ and $\tilde{m}_z$ characterizes the biases, as follows:

$$\tilde{m}_x = -\frac{x_4^2 x_6 + 2x_3x_8 - 4x_5x_6 - x_2x_4x_8 + 2x_2x_5x_7 - x_3x_4x_7}{2(x_5x_2^2 - x_2x_3x_4 + x_3^2 + x_1x_4^2 - 4x_1x_5)} \equiv b_x \tag{5.29}$$

$$\tilde{m}_y = -\frac{x_3^2 x_7 + 2x_1x_4x_8 - 4x_1x_5x_7 - x_2x_3x_8 + 2x_2x_5x_6 - x_3x_4x_6}{2(x_5x_2^2 - x_2x_3x_4 + x_3^2 + x_1x_4^2 - 4x_1x_5)} \equiv b_y \tag{5.30}$$

$$\tilde{m}_z = -\frac{x_2^2 x_8 - 4x_1x_8 + 2x_3x_6 + 2x_1x_4x_7 - x_2x_3x_7 - x_2x_4x_6}{2(x_5x_2^2 - x_2x_3x_4 + x_3^2 + x_1x_4^2 - 4x_1x_5)} \equiv b_z \tag{5.31}$$

The adequacy of (5.29), (5.30) and (5.31) can be verified using the same rationale employed for the two-dimensional ETS equations (4.22) to (4.23). In this case, the parameters x_1 to x_9 in (5.29) to (5.31) shall be substituted by their counterparts of (5.24), and the outcomes by their analytical descriptions in terms of biases, scale factors and misalignments derived in (5.11) to (5.23). After manipulation it can be demonstrated that the right hand sides of the resulting equations simplifies to b_x, b_y and b_z, respectively.

If we compare the analytical biases solution derived above with the one proposed by Vasconcelos et al. (2011) (3.82), we can notice that the expressions for b_x and b_z are the same. However, their solution for b_y is misleading. Let us rearrange it in terms of $\boldsymbol{X}_{3D}$ variables:

$$b_{v_y} = -\frac{\frac{{x_2}^2 x_8 - 4x_1x_8 + 2x_3x_6 + 2x_1x_4x_7 - x_2x_3x_7 - x_2x_4x_6}{{x_5}^3}}{\frac{2{x_2}^2 - 8x_1}{{x_5}^2} + \frac{2{x_3}^2 + 2x_1{x_4}^2 - 2x_2x_3x_4}{{x_5}^3}} \tag{5.32}$$

We can check the analytical solution of (5.32) by: (a) substituting x_1 to x_9 by their counterparts in terms of A to J established in (5.24); (b) substituting the A to J terms in the resulting equation by their counterparts in terms of biases, scale factors and misalignments established in (5.11) to (5.20); and (c) simplifying the results. If the Vasconcelos' solution was correct, we should be left with $b_{v_y} = b_y$. However, the following equation is produced (after extensive simplification):

$$b_{v_y} = -\frac{\left(\begin{array}{r} 2s_xs_zb_y - 2s_yb_x\sin\rho - 4s_xs_zb_y\cos^2\lambda + 2s_xs_zb_y\cos^4\lambda - 2s_xs_zb_y\cos^2\rho \ldots \\ +6s_xs_zb_y\cos^2\lambda\cos^2\rho - 4s_xs_zb_y\cos^4\lambda\cos^2\rho + 2s_xs_zb_y\cos^2\lambda\cos^2\theta \ldots \\ -2s_xs_zb_y\cos^4\lambda\cos^2\theta - 2s_xs_yb_z\cos\rho\sin\lambda + 4s_ys_zb_x\cos^2\lambda\sin\rho \ldots \\ +2s_xs_yb_z\cos^3\rho\sin\lambda - 2s_ys_zb_x\cos^4\lambda\sin\rho + 2s_ys_zb_x\cos^2\rho\sin\rho \ldots \\ -2s_xs_zb_y\cos^2\lambda\cos^2\rho\cos^2\theta + 2s_xs_zb_y\cos^4\lambda\cos^2\rho\cos^2\theta \ldots \\ +s_xs_zb_y\cos^4\lambda\cos^2\rho\cos^4\theta + 2s_xs_yb_z\cos^2\lambda\cos\rho\sin\lambda \ldots \\ -4s_xs_yb_z\cos^2\lambda\cos^3\rho\sin\lambda - 10s_ys_zb_x\cos^2\lambda\cos^2\rho\sin\rho \ldots \\ +8s_ys_zb_x\cos^4\lambda\cos^2\rho\sin\rho - 2s_ys_zb_x\cos^2\lambda\cos^2\theta\sin\rho \ldots \\ +2s_ys_zb_x\cos^4\lambda\cos^2\theta\sin\rho + 6s_ys_zb_x\cos\lambda\cos\rho\sin\lambda\sin\theta \ldots \\ +2s_xs_yb_z\cos^2\lambda\cos^3\rho\cos^2\theta\sin\lambda + 6s_ys_zb_x\cos^2\lambda\cos^2\rho\cos^2\theta\sin\rho \ldots \\ -6s_ys_zb_x\cos^4\lambda\cos^2\rho\cos^2\theta\sin\rho - 6s_ys_zb_x\cos\lambda\cos^3\rho\sin\lambda\sin\theta \ldots \\ -6s_ys_zb_x\cos^3\lambda\cos\rho\sin\lambda\sin\theta + 4s_xs_yb_z\cos\lambda\cos^2\rho\sin\rho\sin\theta \ldots \\ -2s_xs_yb_z\cos^2\lambda\cos\rho\cos^2\theta\sin\lambda + 8s_ys_zb_x\cos^3\lambda\cos^3\rho\sin\lambda\sin\theta \ldots \\ -4s_xs_yb_z\cos^3\lambda\cos^2\rho\sin\rho\sin\theta + 4s_xs_zb_y\cos^3\lambda\cos\rho\sin\lambda\sin\rho\sin\theta \ldots \\ +2s_ys_zb_x\cos^3\lambda\cos\rho\cos^2\theta\sin\lambda\sin\theta - 4s_xs_zb_y\cos\lambda\cos\rho\sin\lambda\sin\rho\sin\theta \ldots \\ -2s_ys_zb_x\cos^3\lambda\cos^3\rho\cos^2\theta\sin\lambda\sin\theta \end{array}\right)}{s_xs_z\cos^4\lambda\cos^2\rho\cos^4\theta} \tag{5.33}$$

which confirms that the analytical solution proposed by Vasconcelos et al. (2011) for b_y is not accurate.

5.2.2 Scale Factors

Analytical solutions for the scale factors were also proposed by Vasconcelos et al. (2011), as described in equations (3.75), (3.76) and (3.77), which are rewritten here in terms of $\boldsymbol{X}_{3D}$ variables as:

$$a = -\frac{x_5^3\sqrt{\frac{\xi_5(-x_4^2+4x_5)}{x_5^6}}}{2(x_5x_2^2 - x_2x_3x_4 + x_3^2 + x_1x_4^2 - 4x_1x_5)} \tag{5.34}$$

$$b = -\frac{x_5^3\sqrt{-\frac{\xi_5(x_3^2-4x_1x_5)}{x_5^6}}}{2(x_5x_2^2 - x_2x_3x_4 + x_3^2 + x_1x_4^2 - 4x_1x_5)} \tag{5.35}$$

$$c = -\frac{x_5^3\sqrt{\frac{\xi_5(-x_2^2+4x_1)}{x_5^6}}}{2(x_5x_2^2 - x_2x_3x_4 + x_3^2 + x_1x_4^2 - 4x_1x_5)} \tag{5.36}$$

with

$$\begin{aligned}\xi_5 = &-x_2^2x_8^2 + 4x_5x_9x_2^2 - 4x_9x_2x_3x_4 + 2x_2x_3x_7x_8 + 2x_2x_4x_6x_8 - 4x_5x_2x_6x_7 \\ &- x_3^2x_7^2 + 4x_9x_3^2 + 2x_3x_4x_6x_7 - 4x_3x_6x_8 - x_4^2x_6^2 + 4x_1x_9x_4^2 - 4x_1x_4x_7x_8 \\ &+ 4x_5x_6^2 + 4x_1x_5x_7^2 + 4x_1x_8^2 - 16x_1x_5x_9\end{aligned} \tag{5.37}$$

where a, b and c are the scale factor analytical solutions for the ETS methodology derived via the formulations proposed by (VASCONCELOS et al., 2011).

Such solutions can be verified by first substituting x_1 to x_9 in (5.34) to (5.37) by their counterparts presented in (5.24), and then rewriting them in terms of biases, scale factors and misalignments using (5.11) to (5.20). After simplification, the following relations are obtained:

$$\begin{aligned}a &= m_t s_x \\ b &= m_t s_y \\ c &= m_t s_z\end{aligned} \tag{5.38}$$

Equation (5.38) reveals that Vasconcelos' analytical solution for the scale factors a, b, c, are actually misleading, as they correspond to the true scale factors s_x, s_y, s_z multiplied by the magnitude of the local Earth magnetic field density (m_t). As m_t is a value easily computed through magnetic models (WMM or IGRF), corrected analytical solutions for the scale factors can be devised:

$$s_x = -\frac{x_5^3\sqrt{\frac{\xi_5(-x_4^2+4x_5)}{x_5^6}}}{2m_t(x_5x_2^2 - x_2x_3x_4 + x_3^2 + x_1x_4^2 - 4x_1x_5)} \tag{5.39}$$

$$s_y = -\frac{x_5^3\sqrt{-\frac{\xi_5(x_3^2-4x_1x_5)}{x_5^6}}}{2m_t(x_5x_2^2 - x_2x_3x_4 + x_3^2 + x_1x_4^2 - 4x_1x_5)} \tag{5.40}$$

$$s_z = -\frac{x_5^3\sqrt{\frac{\xi_5(-x_2^2+4x_1)}{x_5^6}}}{2m_t(x_5x_2^2 - x_2x_3x_4 + x_3^2 + x_1x_4^2 - 4x_1x_5)} \tag{5.41}$$

5.2.3 Misalignments

The analytical misalignment solutions proposed by Vasconcelos et al. (2011) for the ETS methodology, given in (3.78) to (3.80), can be rewritten in terms of $\boldsymbol{X}_{3D}$ variables, as follows:

$$\rho_v = \arctan\left(\frac{2x_2x_5 - x_3x_4}{2x_5^2\sqrt{-\frac{x_5x_2^2 - x_2x_3x_4 + x_3^2 + x_1x_4^2 - 4x_1x_5}{x_5^3}}}\right) \tag{5.42}$$

$$\phi_v = \arctan\left(-\frac{\frac{2x_3}{{x_5}^2} - \frac{x_2x_4}{{x_5}^2}}{\sqrt{\frac{4x_1}{{x_5}^2} - \frac{{x_2}^2}{{x_5}^2} - \frac{{x_3}^2}{{x_5}^3} - \frac{x_1{x_4}^2}{{x_5}^3} + \frac{x_2x_3x_4}{{x_5}^3}}}\right) \tag{5.43}$$

$$\lambda_v = -\arctan\left(\frac{x_4}{x_5}\sqrt{-\frac{x_5^2(x_5x_2^2 - x_2x_3x_4 + x_3^2 + x_1x_4^2 - 4x_1x_5)}{2x_2^2x_4^2x_5 - 4x_2^2x_5^2 - x_2x_3x_4^3 + x_3^2x_4^2 + x_1x_4^4 - 8x_1x_4^2x_5 + 16x_1x_5^2}}\right) \tag{5.44}$$

where the subscript $_v$ indicates the analytical solutions by Vasconcelos et al. (2011).

The analytical solutions above can be verified by first substituting x_1 to x_9 in (5.42) to (5.44) by their respective counterparts presented in (5.24), and then rewriting them in terms of biases, scale factors and misalignments using (5.11) to (5.20). After simplifying, the following results are obtained:

$$\begin{aligned} \rho_v &= -\rho \\ \phi_v &= \frac{2s_z\cos\lambda\sin\phi}{s_y\cos\rho} \\ \lambda_v &= \lambda \end{aligned} \tag{5.45}$$

We can conclude from (5.45) that the analytical solutions proposed by Vasconcelos et al. (2011) are only correct for λ_v, while ρ_v has a switched sign, and ϕ_v has the residual variables displayed in (5.45). Since we have already derived analytical solutions for such variables, namely, s_y and s_z, we can correct ρ_v and ϕ_v accordingly, yielding the following corrected analytical solutions for the misalignments:

$$\rho = -\arctan\left(\frac{2x_2x_5 - x_3x_4}{2x_5^2\sqrt{-\frac{x_5x_2^2 - x_2x_3x_4 + x_3^2 + x_1x_4^2 - 4x_1x_5}{x_5^3}}}\right) \tag{5.46}$$

$$\phi = -\arctan\left(\frac{\eta_3\sqrt{\eta_6\eta_1}\sqrt{\frac{\eta_7(\eta_4-\eta_5)}{\eta_2}}}{\sqrt{(\eta_4-\eta_5)\eta_1}\sqrt{1-\frac{\eta_3^2}{\eta_2}}\sqrt{-\frac{\eta_7\eta_6}{\eta_5-\eta_4+\eta_{10}+\eta_8-\eta_9}}\sqrt{\eta_4-\eta_5-\eta_{10}-\eta_8+\eta_9)}}\right) \tag{5.47}$$

$$\lambda = -\arctan\left(\frac{x_4}{x_5}\sqrt{-\frac{x_5^2(x_5x_2^2-x_2x_3x_4+x_3^2+x_1x_4^2-4x_1x_5)}{2x_2^2x_4^2x_5-4x_2^2x_5^2-x_2x_3x_4^3+x_3^2x_4^2+x_1x_4^4-8x_1x_4^2x_5+16x_1x_5^2}}\right) \tag{5.48}$$

where

$$\begin{aligned}\eta_1 =& \frac{4x_6^2}{x_5^3}+\frac{4x_1x_7^2}{x_5^3}+\frac{4x_1x_8^2}{x_5^4}+\frac{4x_2^2x_9}{x_5^3}+\frac{4x_3^2x_9}{x_5^4}-\frac{x_2^2x_8^2}{x_5^4}-\frac{x_3^2x_7^2}{x_5^4}-\frac{x_4^2x_6^2}{x_5^4}-\frac{16x_1x_9}{x_5^3}+\frac{4x_1x_4^2x_9}{x_5^4}\\ &-\frac{4x_2x_6x_7}{x_5^3}-\frac{4x_3x_6x_8}{x_5^4}-\frac{4x_2x_3x_4x_9}{x_5^4}-\frac{4x_1x_4x_7x_8}{x_5^4}+\frac{2x_2x_3x_7x_8}{x_5^4}+\frac{2x_2x_4x_6x_8}{x_5^4}+\frac{2x_3x_4x_6x_7}{x_5^4}\end{aligned} \tag{5.49}$$

$$\begin{aligned}\eta_2 &= \tfrac{16x_1}{x_5^3}-\tfrac{4x_2^2}{x_5^3}-\tfrac{8x_1x_4^2}{x_5^4}+\tfrac{x_1x_4^4}{x_5^5}+\tfrac{2x_2^2x_4^2}{x_5^4}+\tfrac{x_3^2x_4^2}{x_5^5}-\tfrac{x_2x_3x_4^3}{x_5^5}\\ \eta_3 &= \tfrac{2x_3}{x_5^2}-\tfrac{x_2x_4}{x_5}2\\ \eta_4 &= \tfrac{4x_1}{x_5^2}\\ \eta_5 &= \tfrac{x_2^2}{x_5^2}\\ \eta_6 &= \tfrac{4x_1}{x_5}-\tfrac{x_3^2}{x_5^2}\\ \eta_7 &= \tfrac{4}{x_5}-\tfrac{x_4^2}{x_5^2}\\ \eta_8 &= \tfrac{x_1x_4^2}{x_5^3}\\ \eta_9 &= \tfrac{x_2x_3x_4}{x_5^3}\\ \eta_{10} &= \tfrac{x_3^2}{x_5^3}\end{aligned} \tag{5.50}$$

One may also numerically verify the adequacy of the proposed analytical solution for the biases, scale factors and misalignments by implementing the numerical solution from the previous section and comparing the results, as done in sequence.

5.3 Simulated Experiments

The simulated experiments are divided into a calibration example using data corrupted by arbitrary error parameters within the range expected for a consumer grade magnetometer, followed by a Monte Carlo analysis that aimed at identifying the estimation error distribution for each implemented method, which enables a more comprehensive comparison.

5.3.1 Calibration Example

In this section, we perform the three-dimensional calibration of a simulated magnetometer using the methodologies described in Chapter 3. Since Foster and Elkaim (2008) do not provide a closed-form solution for their ETS method, the latter is employed with our numerical and analytical solutions. In addition, since Vasconcelos et al. (2011) initialize their MLE algorithm with a partially incorrect analytical solution from ETS (as demonstrated in Section 5.2), we also alternatively use ours to initialize it, and compare the outcome.

The magnetometer data generated were corrupted by errors in the range expected for a consumer grade sensor like the Honeywell HMC5883L used in the real data experiments, as displayed in Table 5.1. There were no conventions about how the sensor should be rotated; the idea was to rotate it in a way that enabled the full ellipsoid estimation. In this case, we simulated the sensor continuously rotating in yaw, while oscillating in roll and pitch. The data were generated at a rate of 15 Hz, with a total of 2500 samples.

Table 5.1 – Three-dimensional errors randomly chosen for corrupting the simulated measurements.

Error parameter	Simulated value	Unit
b_x	39.8316	mG
b_y	27.1376	mG
b_z	-12.4947	mG
s_x	0.8893	unitless
s_y	0.9796	unitless
s_z	0.8234	unitless
ρ	0.8234	deg
ϕ	0.6166	deg
λ	1.3106	deg

After the generation, the data were then calibrated via the investigated calibration algorithms. The resulting estimation errors are displayed in Tables 5.2 to 5.4 [1].

Table 5.2 – Three-dimensional bias calibration results for a simulated data example.

Calibration methodology	b_x estimation error (mG)	b_y estimation error (mG)	b_z estimation error (mG)
TWOSTEP	-3.1438×10^{-2}	7.4135×10^{-3}	-3.8911×10^{-2}
ETS-N	-3.1307×10^{-2}	5.4035×10^{-3}	-4.0235×10^{-2}
ETS-A	-3.1307×10^{-2}	5.4035×10^{-3}	-4.0235×10^{-2}
ETS-V	-3.1350×10^{-2}	-5.5019×10^{1}	-3.9582×10^{-2}
MLE-A	-3.1179×10^{-2}	5.5894×10^{-3}	-4.0504×10^{-2}
MLE-V	-3.6706×10^{2}	-3.6932×10^{2}	-1.0032×10^{2}
CTLS	-2.9226×10^{-2}	3.8999×10^{-3}	-4.2465×10^{-2}
OML	-2.9400×10^{-2}	3.7572×10^{-3}	-4.2646×10^{-2}
MAG.I.C.AL	-6.9230×10^{-1}	-1.6244×10^{0}	4.4378×10^{0}

Table 5.3 – Three-dimensional scale factor calibration results for a simulated data example.

Calibration methodology	s_x estimation error (unitless)	s_y estimation error (unitless)	s_z estimation error (unitless)
TWOSTEP	-7.1609×10^{-5}	5.3208×10^{-5}	4.7034×10^{-4}
ETS-N	1.7792×10^{-5}	-1.3877×10^{-4}	2.4373×10^{-4}
ETS-A	1.7792×10^{-5}	-1.3877×10^{-4}	2.4373×10^{-4}
ETS-V	-8.8931×10^{-1}	-9.7958×10^{-1}	-8.2339×10^{-1}
MLE-A	-3.6319×10^{-6}	-5.7832×10^{-5}	2.0570×10^{-4}
MLE-V	2.1835×10^{-1}	-1.9650×10^{0}	-1.0834×10^{1}
CTLS	-2.1696×10^{-5}	-5.9601×10^{-5}	1.7982×10^{-4}
OML	-1.1752×10^{-5}	-5.2080×10^{-5}	1.8910×10^{-4}
MAG.I.C.AL	-1.8075×10^{-3}	-8.8932×10^{-3}	1.3748×10^{-2}

[1] Abbreviations: TWOSTEP refers to the method presented by Alonso and Shuster (2002b); ETS-N refers to the method by Foster and Elkaim (2008) solved with our proposed numerical solution; ETS-A denotes the method by Foster and Elkaim (2008) solved with our proposed analytical solution; ETS-V represents the method by Foster and Elkaim (2008) solved with the analytical solution proposed by Vasconcelos et al. (2011); MLE-A corresponds to the method by Vasconcelos et al. (2011) initialized with our proposed analytical solution; MLE-V corresponds the method by Vasconcelos et al. (2011) initialized with the solution proposed by Vasconcelos et al. (2011); CTLS refers to the method by Wu et al. (2013); OML refers to th method by Wu and Shi (2015); and MAG.I.C.AL refers to the method by Papafotis and Sotiriadis (2019).

Table 5.4 – Three-dimensional misalignment calibration results for a simulated data example.

Calibration methodology	ρ estimation error (deg)	ϕ estimation error (deg)	λ estimation error (deg)
TWOSTEP	-8.8220×10^{-2}	2.0321×10^{-2}	1.3756×10^{-1}
ETS-N	-1.7941×10^{-2}	8.1703×10^{-3}	1.0490×10^{-2}
ETS-A	-1.7941×10^{-2}	8.1703×10^{-3}	1.0490×10^{-2}
ETS-V	-2.6321×10^{0}	4.3397×10^{-1}	1.0583×10^{-2}
MLE-A	-1.1050×10^{-2}	7.3031×10^{-3}	-1.4013×10^{-2}
MLE-V	6.1042×10^{1}	3.5609×10^{1}	-3.0913×10^{1}
CTLS	-2.0024×10^{-2}	7.7144×10^{-3}	1.0317×10^{-2}
OML	1.0562×10^{-4}	-9.9392×10^{-17}	-1.9878×10^{-16}
MAG.I.C.AL	-1.1968×10^{0}	-6.8887×10^{-1}	-9.5995×10^{-1}

It is also interesting to graphically evaluate the calibration performances. Figure 5.2 shows the corrupted data plotted with the reference sphere of radius m_t (computed via WMM), while Figure 5.3 displays the corrected measurements via the calibration algorithms presented. Notice that ETS-V and MLE-V are omitted, since they performed poorly.

Figure 5.2 – Corrupted data plotted with the reference sphere of radius m_t.

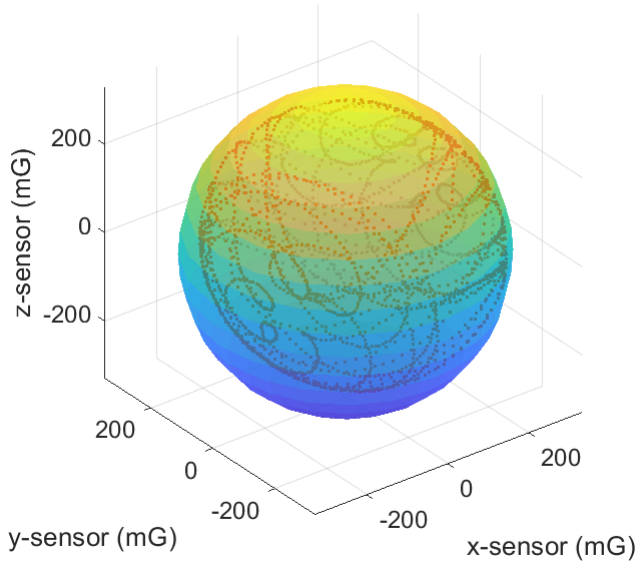

Figure 5.3 – Corrected data plotted with the reference sphere of radius m_t. The data corrected by each calibration arrangement is distinguished by color, in accordance with the legend.

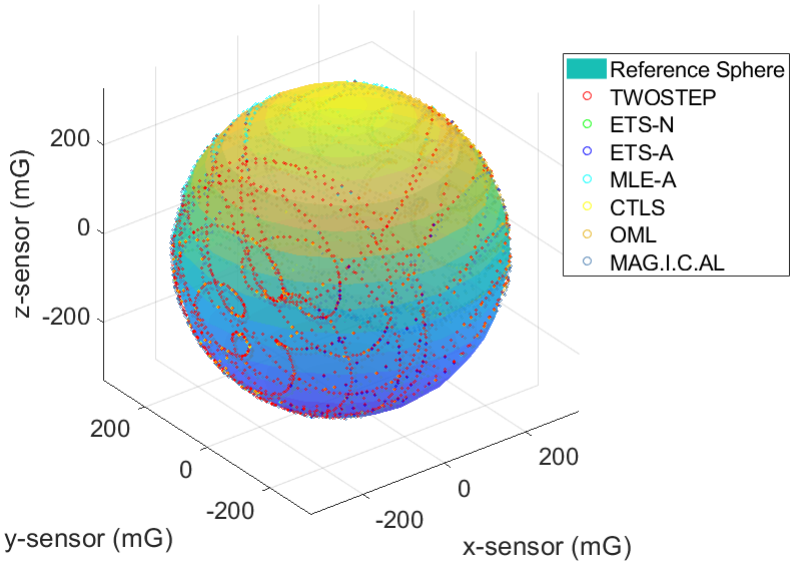

Even though Tables 5.2 to 5.4 and Figure 5.3 are a good indicator of the calibration effectiveness, it is not possible to clearly evaluate the differences between the methods. That is why further analysis is necessary.

5.3.2 Monte Carlo Analysis

A Monte Carlo analysis was conducted in order to further evaluate the performance of each calibration algorithm. The objective was to identify the estimation error distribution for each method, so that their statistical properties were adequately assessed. In the experiment, the calibration using each methodology was performed in 3500 runs with random error parameters within the expected range (for the Honeywell HMC5883L used in the real data experiments) corrupting the measurements, as displayed in Table 5.5. In addition, the calibration location (on Earth) and time were randomly selected for each run in order to avoid a dependency of the results with respect to the place or time when the calibration occurs, since the Earth's magnetic field models are functions of these two variables.

Table 5.5 – Error parameters used to generate the data for the Monte Carlo analysis for the three-dimensional case.

Error Parameter	Mean	Standard Deviation	Unit
b_x	0	50	mG
b_y	0	50	mG
b_z	0	50	mG
s_x	1	0.1	unitless
s_y	1	0.1	unitless
s_z	1	0.1	unitless
ρ	0	1	deg
ϕ	0	1	deg
λ	0	1	deg

Figures 5.4 to 5.12 show a line histogram, where the probability (occurrence divided by the total number of runs) of estimation error is presented for b_x, b_y, b_z, s_x, s_y, s_z, ρ, ϕ and λ, respectively. Notice that the probabilities for the methods ETS-V and MLE-V are not displayed, since their estimates did not converge to reasonable parameters in most cases, so they could be displayed in the same scale as the others.

Figure 5.4 – Probability of b_x estimation error for each calibration methodology.

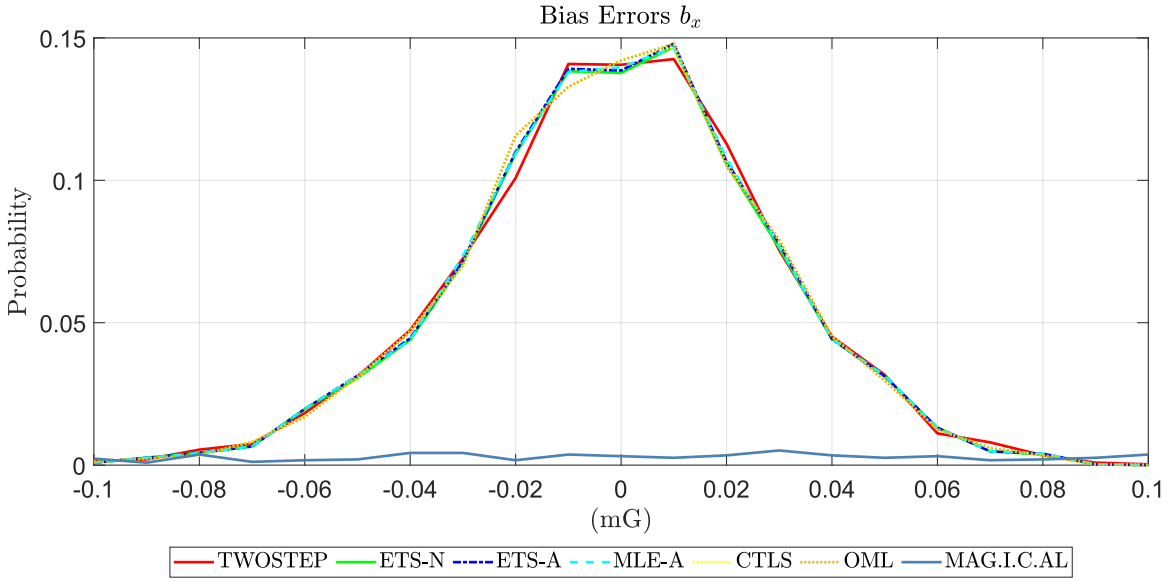

Figure 5.5 – Probability of b_y estimation error for each calibration methodology.

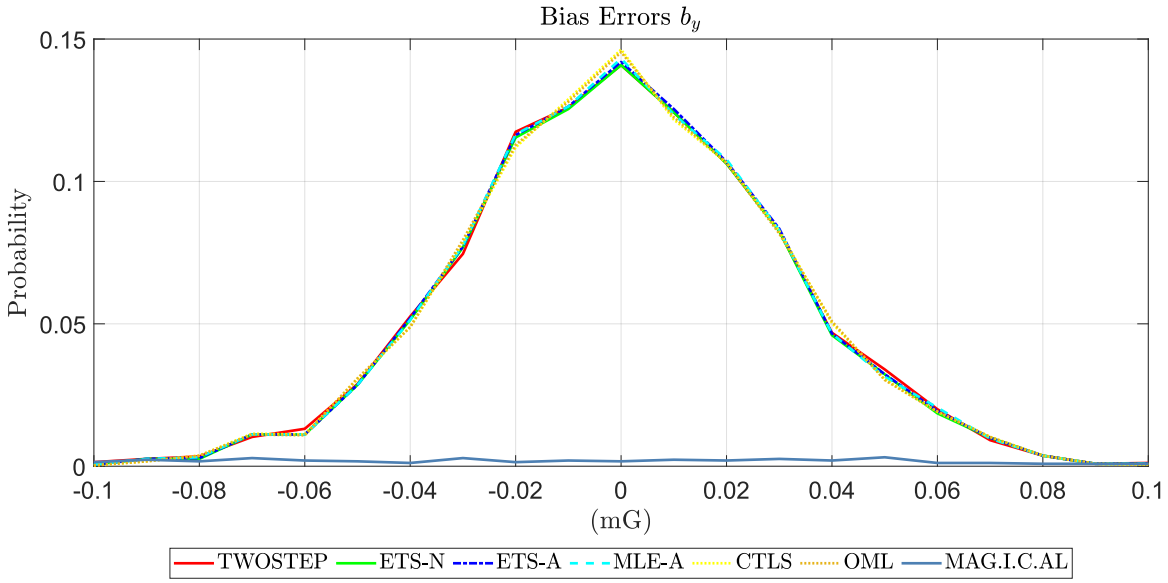

Figure 5.6 – Probability of b_z estimation error for each calibration methodology.

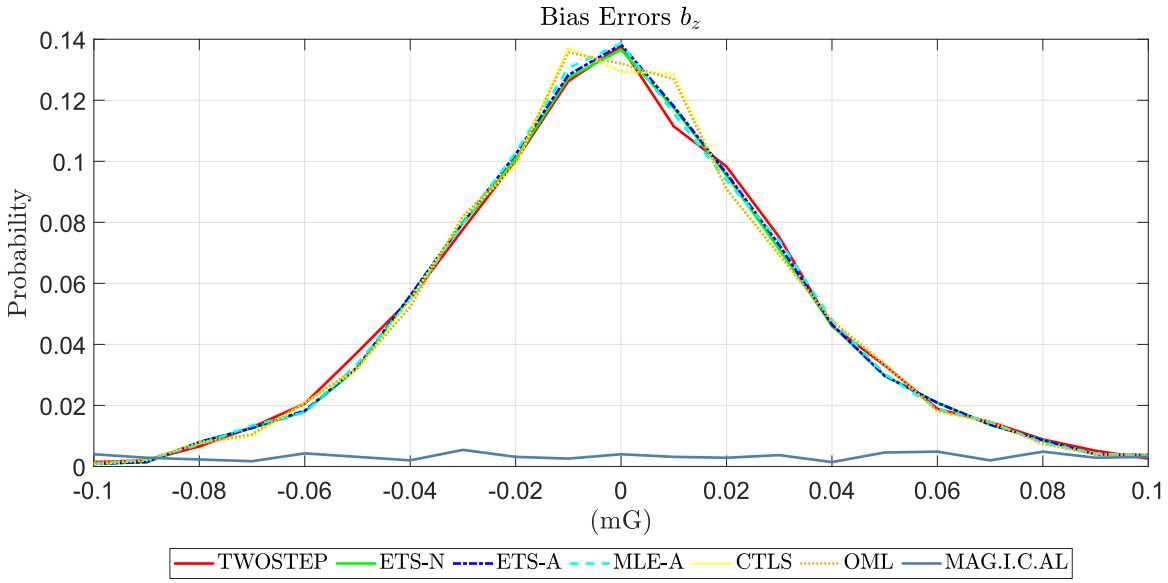

Figure 5.7 – Probability of s_x estimation error for each calibration methodology.

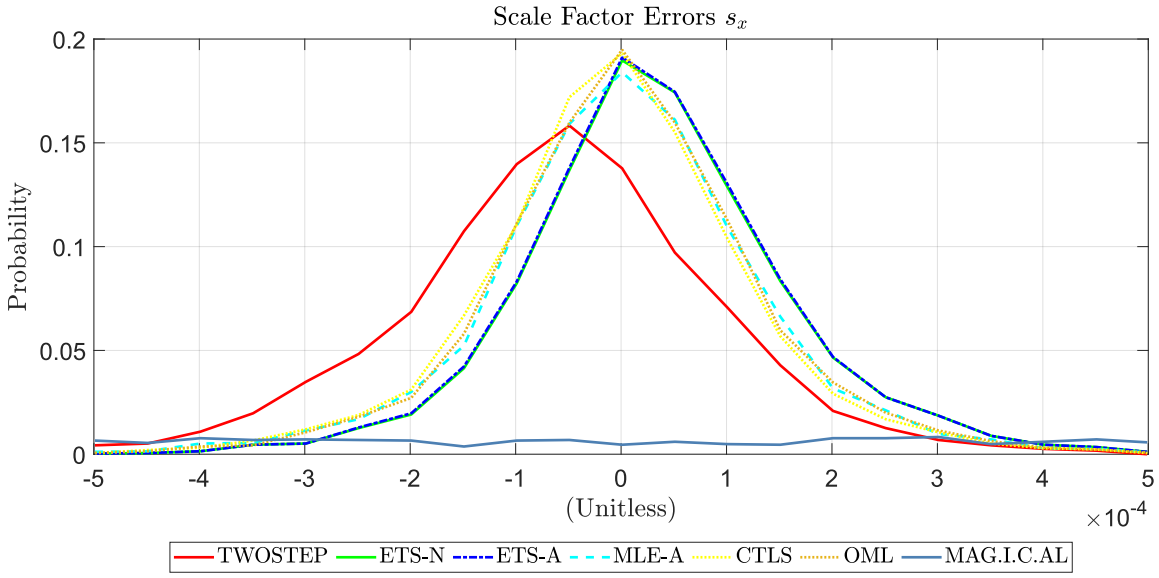

Figure 5.8 – Probability of s_y estimation error for each calibration methodology.

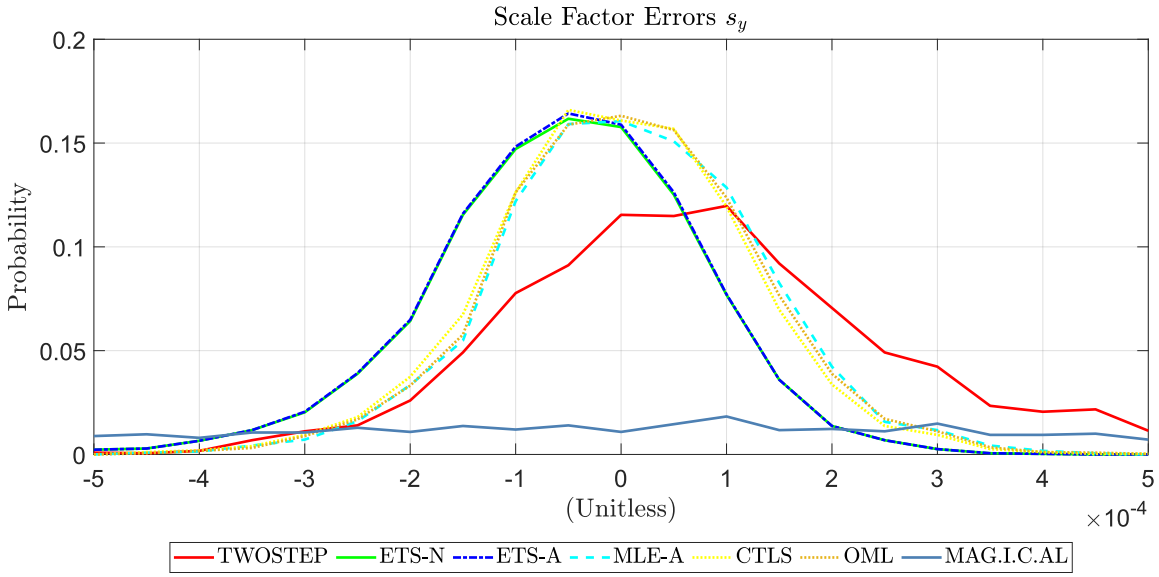

Figure 5.9 – Probability of s_z estimation error for each calibration methodology.

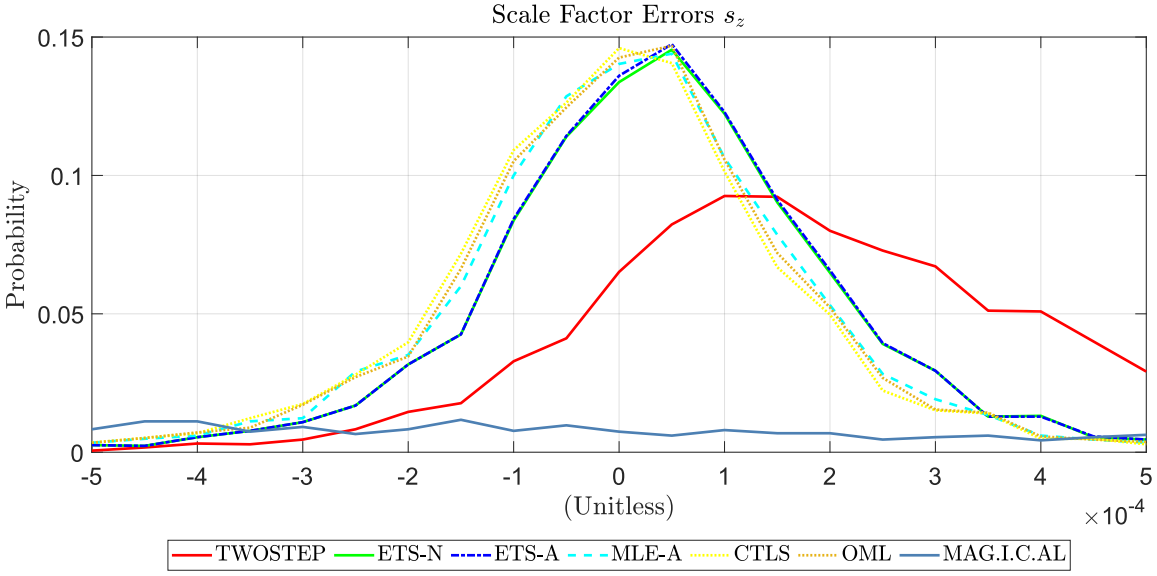

Figure 5.10 – Probability of ρ estimation error for each calibration methodology.

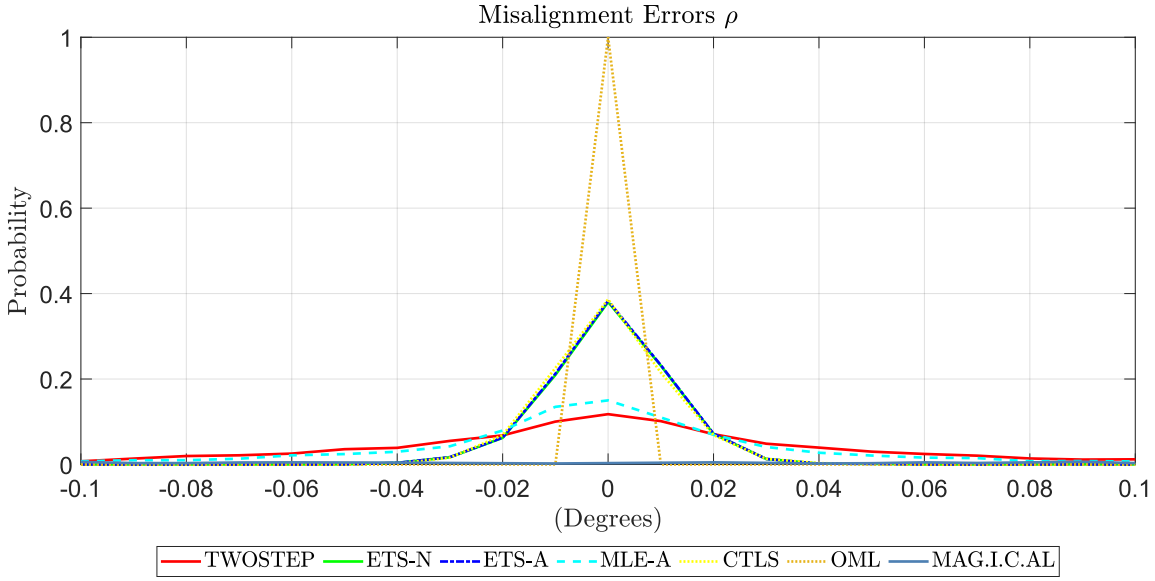

Figure 5.11 – Probability of ϕ estimation error for each calibration methodology.

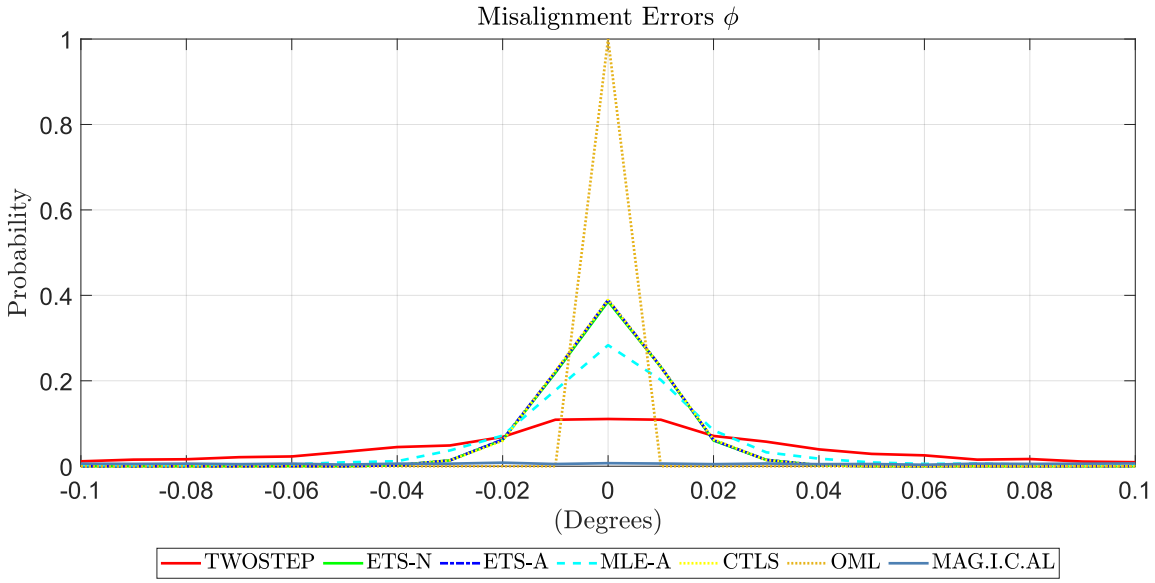

Figure 5.12 – Probability of λ estimation error for each calibration methodology.

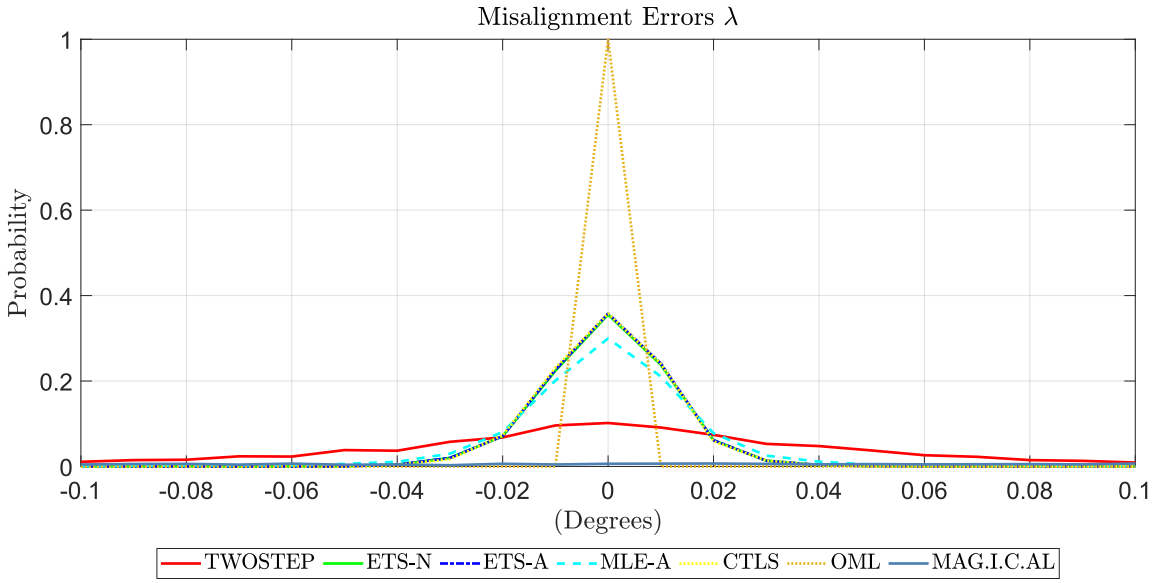

Firstly, Figures 5.4 to 5.6 present the estimation error histograms for the biases, showing that the methods TWOSTEP, ETS-N, ETS-A, MLE-A, CTLS and OML presented similar performances and were clearly superior to MAG.I.C.AL, which visually exhibited a much wider error distribution.

The scale factor estimation error histograms are presented in Figures 5.7 to 5.9, where we can see that as for the biases, a very poor performance was achieved by the MAG.I.C.AL.

method. ETS-N, ETS-A, MLE-A, CTLS and OML performed similarly for s_x and s_z, but ETS-A and ETS-N showed a slight shift to the left for s_y, meaning that their mean is not as close to zero. Even though superior to MAG.I.C.AL, TWOSTEP performed substantially worse than the others, with a right shift for s_x and a left shift for s_y and s_z, in addition to a broader distribution.

For the misalignment estimation errors, the histograms are displayed in Figures 5.10 to 5.12. Regarding ρ (Figure 5.10), OML presented a superior performance, followed by ETS-N, ETS-A and CTLS, which performed similarly, MLE-A and TWOSTEP, with poorer performances. MAG.I.CAL, again, had the worst performance. It is interesting to notice that MLE-A, which employed ETS-A's solutions as initial conditions, worsened the estimates, instead of improving them. The same pattern persists for ϕ and λ (Figures 5.11 and 5.12, respectively), except for MLE-A, which approximated its performance to the ones by ETS-N, ETS-A and CTLS.

The overall conclusions from Figures 5.4 to 5.12 are: (a) MAG.I.C.AL showed, by far, the worst performance in terms of accuracy and precision for biases, scale factors and misalignments; (b) TWOSTEP, ETS-A, ETS-N, MLE-A, CTLS and OML performed similarly for biases; (c) for scale factors, OML, CTLS, MLE-A, ETS-N and ETS-A performed well, with the last two slightly behind, while TWOSTEP showed a substantially worse performance. (d) for misalignments, OML presented the best performance, followed by ETS-N, ETS-A and CTLS (very similar), MLE-A and TWOSTEP.

Even though Figures 5.4 to 5.12 provide rich information for analyzing the robustness of the calibration methods, they should not be considered alone in order to establish a solid conclusion, since they do not account for the cases in which the methods diverge (prone to happen specially in the iterative methods). Such eventual divergences are considered in Tables 5.6 to 5.11, which display the estimation error distribution in terms of mean and standard deviation for each error parameter.

Table 5.6 – Mean of the bias estimation errors (including eventual divergent estimations).

Calibration methodology	b_x estimation error mean (mG)	b_y estimation error mean (mG)	b_z estimation error mean (mG)
TWOSTEP	-4.9221×10^{-3}	2.4261×10^{-3}	-1.8908×10^{-4}
ETS-N	7.8058×10^{-1}	6.1418×10^{-2}	-9.1687×10^{-2}
ETS-A	-5.8442×10^{-3}	2.8462×10^{-3}	1.3294×10^{-5}
ETS-V	-5.8526×10^{-3}	-7.6831×10^{0}	4.0700×10^{-4}
MLE-A	5.9211×10^{0}	-4.9102×10^{1}	-1.7652×10^{1}
MLE-V	6.5960×10^{3}	2.6754×10^{4}	-2.2921×10^{4}
CTLS	-6.6007×10^{-3}	2.8248×10^{-3}	-9.2190×10^{-4}
OML	-6.6025×10^{-3}	2.8441×10^{-3}	-9.2258×10^{-4}
MAG.I.C.AL	4.6092×10^{-1}	-2.2128×10^{-1}	-4.6044×10^{-1}

Table 5.7 – Standard deviations of the bias estimation errors (including eventual divergent estimations).

Calibration methodology	b_x estimation error standard deviation (mG)	b_y estimation error standard deviation (mG)	b_z estimation error standard deviation (mG)
TWOSTEP	2.8847×10^{-1}	2.9594×10^{-1}	3.4122×10^{-1}
ETS-N	4.9777×10^{1}	3.8070×10^{1}	4.9958×10^{1}
ETS-A	2.8498×10^{-1}	2.9268×10^{-1}	3.3762×10^{-1}
ETS-V	2.8501×10^{-1}	9.9723×10^{2}	3.3804×10^{-1}
MLE-A	3.5064×10^{2}	2.9051×10^{3}	1.0443×10^{3}
MLE-V	6.2591×10^{5}	9.2455×10^{5}	1.1177×10^{6}
CTLS	2.8355×10^{-1}	2.9170×10^{-1}	3.3603×10^{-1}
OML	2.8353×10^{-1}	2.9171×10^{-1}	3.3607×10^{-1}
MAG.I.C.AL	3.0635×10^{1}	2.4528×10^{1}	4.0761×10^{1}

Table 5.8 – Mean of the scale factor estimation errors (including eventual divergent estimations).

Calibration methodology	s_x estimation error mean	s_y estimation error mean	s_z estimation error mean
TWOSTEP	-6.1157×10^{-5}	9.5149×10^{-5}	2.4604×10^{-4}
ETS-N	1.6516×10^{-4}	3.5678×10^{-4}	1.0939×10^{-4}
ETS-A	3.2206×10^{-5}	-5.4367×10^{-5}	4.4503×10^{-5}
ETS-V	2.0795×10^{4}	2.0788×10^{4}	2.0814×10^{4}
MLE-A	3.1839×10^{8}	2.9541×10^{7}	-3.0988×10^{8}
MLE-V	Infinite*	8.7390×10^{12}	3.3130×10^{14}
CTLS	-3.6265×10^{-6}	-4.1380×10^{-6}	-1.0661×10^{-6}
OML	4.7168×10^{-6}	4.2183×10^{-6}	7.3496×10^{-6}
MAG.I.C.AL	-6.9909×10^{-4}	-2.0697×10^{-4}	4.8312×10^{-4}

*Numeric solution classified by MATLAB® as *Inf*

Table 5.9 – Standard deviations of the scale factor estimation errors (including eventual divergent estimations).

Calibration methodology	s_x estimation error standard deviation	s_y estimation error standard deviation	s_z estimation error standard deviation
TWOSTEP	1.5175×10^{-4}	2.1426×10^{-4}	2.9017×10^{-4}
ETS-N	7.4667×10^{-3}	8.8041×10^{-3}	6.6859×10^{-3}
ETS-A	1.2673×10^{-4}	1.2453×10^{-4}	1.7056×10^{-4}
ETS-V	5.7474×10^{3}	5.8274×10^{3}	5.8272×10^{3}
MLE-A	1.8836×10^{10}	1.7477×10^{9}	1.8333×10^{10}
MLE-V	1.1955×10^{15}	1.7683×10^{15}	1.9851×10^{16}
CTLS	1.2535×10^{-4}	1.2064×10^{-4}	1.6896×10^{-4}
OML	1.2536×10^{-4}	1.2062×10^{-4}	1.6888×10^{-4}
MAG.I.C.AL	4.3141×10^{-3}	3.2015×10^{-3}	8.6997×10^{-3}

Table 5.10 – Mean of the misalignment estimation errors (including eventual divergent estimations).

Calibration methodology	ρ estimation error mean (deg)	ϕ estimation error mean (deg)	λ estimation error mean (deg)
TWOSTEP	2.7829×10^{-4}	-1.0933×10^{-3}	-4.8143×10^{-4}
ETS-N	-9.5639×10^{-4}	-1.1186×10^{-3}	1.5978×10^{-3}
ETS-A	2.0282×10^{-4}	1.2189×10^{-4}	-2.8400×10^{-4}
ETS-V	-1.5827×10^{-2}	2.0468×10^{-2}	-2.8517×10^{-4}
MLE-A	2.0405×10^{-2}	-5.2992×10^{-3}	9.5832×10^{-3}
MLE-V	-1.1745×10^{-1}	-6.1037×10^{-1}	-2.6362×10^{-1}
CTLS	-3.7615×10^{-5}	1.3473×10^{-4}	-2.7273×10^{-4}
OML	-1.2179×10^{-6}	-5.1442×10^{-18}	4.5314×10^{-18}
MAG.I.C.AL	-3.7953×10^{-2}	-1.4547×10^{-2}	-8.4498×10^{-2}

Table 5.11 – Standard deviations of the misalignment estimation errors (including eventual divergent estimations).

Calibration methodology	ρ estimation error standard deviation (deg)	ϕ estimation error standard deviation (deg)	λ estimation error standard deviation (deg)
TWOSTEP	7.5036×10^{-2}	7.0293×10^{-2}	7.4678×10^{-1}
ETS-N	9.4975×10^{-2}	8.1608×10^{-2}	7.7945×10^{-2}
ETS-A	1.1493×10^{-2}	1.0981×10^{-2}	1.1664×10^{-2}
ETS-V	2.0287×10^{0}	1.0655×10^{0}	1.1659×10^{-2}
MLE-A	1.4317×10^{0}	2.2120×10^{-1}	3.6895×10^{-1}
MLE-V	3.4788×10^{1}	3.2622×10^{1}	2.5139×10^{1}
CTLS	1.1382×10^{-2}	1.0962×10^{-2}	1.1591×10^{-2}
OML	1.9264×10^{-4}	1.9799×10^{-16}	2.3607×10^{-16}
MAG.I.C.AL	1.3312×10^{0}	1.1254×10^{0}	1.0059×10^{0}

In order to identify the number of divergences in the calibration methods analysis, we have established a threshold for an estimate to be considered a divergence: the mean absolute estimation error should be larger than 5 mG, 0.1 and 1 deg, for biases, scale factors and misalignments, respectively. These values were defined based on what we consider to be reasonable estimation errors. Table 5.12 displays the number of divergences for each method, where any divergent estimate at a given run is considered divergence.

Table 5.12 – Number of divergences for each method along the Monte Carlo runs.

Method	Number of divergences
TWOSTEP	0
ETS-N	28
ETS-A	0
ETS-V	3500
MLE-A	69
MLE-V	3500
CTLS	0
OML	0
MAG.I.C.AL	2393

The results displayed in Tables 5.6 to 5.12 confirmed most of the verification outlined for Figures 5.4 to 5.12. Firstly, it confirms that ETS-V and MLE-V presented serious divergence problems and shall not be used for magnetometer calibration. The MAG.I.C.AL method also performed poorly, especially for misalignments estimation, having 2393 divergences in 3500 runs. It is also interesting to notice that even though MLE-A performed mostly well in Figures 5.4 to 5.12, its 69 divergences strongly compromised its overall performance in terms of mean and standard deviation, especially for biases and scale factors. The ETS-N method had 28 divergences, but this did not compromise its general performance in terms of mean and standard deviation. Lastly, the TWOSTEP, ETS-A, CTLS and OML methods did not present any divergence. In terms of mean and standard deviation, they performed almost similarly for biases and scale factors, but OML was clearly superior for misalignments, especially for ϕ and λ.

Lastly, it is important to analyze the methods in terms of computational effort required for calibration. Since these algorithms are often intended to be implemented in embedded systems, with limited computational power, they should be as simple as possible, under the risk of precluding implementation. For this purpose Table 5.13 displays the mean execution time required for each method to complete a calibration procedure implemented in MATLAB®,

running in a Windows 10 computer with 8GB RAM, and an Intel I5 processor. The methods ETS-V and MLE-V are not included, since they do not converge in any of the runs.

Table 5.13 – Mean execution time taken by each method to complete a calibration procedure.

Method	Time [s]
TWOSTEP	3.3442×10^{-3}
ETS-N	1.0165×10^{1}
ETS-A	1.3271×10^{-3}
MLE-A	7.2554×10^{-1}
CTLS	2.8341×10^{2}
OML	9.8737×10^{1}
MAG.I.C.AL	8.9197×10^{-2}

From Table 5.13 we can indirectly analyze the computational effort required by each calibration methodology. The most efficient algorithm, in this perspective, was the ETS-A, which took only 1.3271 ms to perform the calibration, less than half of the time taken by TWOSTEP (3.3442 ms), the second most timely efficient. The MAG.I.C.AL methodology stands in the third place, with 89.197 ms of execution time, despite the poor performance with respect to the other metrics evaluated before. The last method that took less than 1 s to execute was the MLE-A, with 725.54 ms. The ETS-N spent, in average, 10.165 s to perform calibration, about 10,000 times the time taken by ETS-A, which is expected, since ETS-N is based on a numerical solution, while ETS-A offers a straightforward analytical alternative. The OML method, despite the great performances evidenced in Figures 5.4 to 5.12, had the second worst result in terms of computational efficiency, taking 98.737s to perform a single calibration, which is about 75,000 times the time required by ETS-A. The CTLS performance is even worse, with 283.41s to perform a calibration, about 200,000 times ETS-A.

In conclusion, we classify ETS-A as the most recommended method, especially if considering application in real-time embedded systems. This analysis is based on: (a) the results from Figures 5.4 to 5.12, which revealed that ETS-A has good performances in terms of accuracy and precision; (b) the results from Tables 5.4 to 5.12, which indicated reduced estimation error mean and standard deviations, as well as showed that no divergences occurred; and (c) the results from Table 5.13, which displayed a very computationally efficient method, compared to the others. The TWOSTEP method had regular overall performances, suggesting robustness, but was inferior to ETS-A in scale factor and misalignment estimation (Figures 5.7 to 5.12) and computational efficiency (Table 5.13). Other methods, namely ETS-N, MLE-A, CTLS and

OML also had good overall performances, particularly the former, despite some particular weaknesses, especially time inefficiency for the last two. Lastly, MAG.I.C.AL performed mostly poorly compared to the other methods, except in terms of computational efficiency.

5.4 Real Data Experiments

In order to validate the ETS calibration methodology by Foster and Elkaim (2008) with the new numerical and analytical solutions proposed in this chapter, and compare their performance with the other implemented calibration techniques, we conduct experiments with a real triaxial magnetometer, namely, the same Honeywell HMC5883L used in Chapter 4. The experiments were performed in two different scenarios. Firstly, the data acquired for the calibration procedures were sampled while the sensor was rotated by hand; this scenario emulates the calibration of a magnetometer fixed into a small vehicle that can be rotated manually. In the second scenario, a robot arm Motoman MH5, the same used in Chapter 4, was used to produce the rotations.

5.4.1 Manual Calibration

In this experiment, the data used in the three dimensional calibration methodologies were acquired, at a rate of 15 Hz while the sensor was rotated by hand. Firstly, a total of 17170 measurements were sampled. However, as demonstrated in Section 5.3.2, some methods, such as CTLS and OML, require too much computational effort if the data size is large, which may even preclude the estimation process. For instance, if all of the 17170 were considered, a 64 bits PC, with an Intel I5 processor and 8GB of RAM, running MATLAB® 2019a, could not solve the estimation problem due to memory insufficiency, as MATLAB® displays the error message "out of memory". Notice that this limitation is troublesome, since in many cases the calibration is expected to be performed in the initialization process of an embedded navigation system, which provides limited computational power. Therefore, the data size was reduce from 17170 to 1010, which is more compatible with the iterative calibration methods. The calibration results plotted with the reference sphere of radius m_t (computed via WMM) are displayed in Figures 5.13 to 5.16. The magnitude errors for each sample, before and after each calibration procedure are shown in Table 5.14, displaying the so called Mean Absolute Magnitude Error (MAME), and Figures 5.17 to 5.19, where ETS-V is omitted due to scale incompatibility.

Figure 5.13 – Measured, corrupted measurements plotted with the reference sphere of radius m_t.

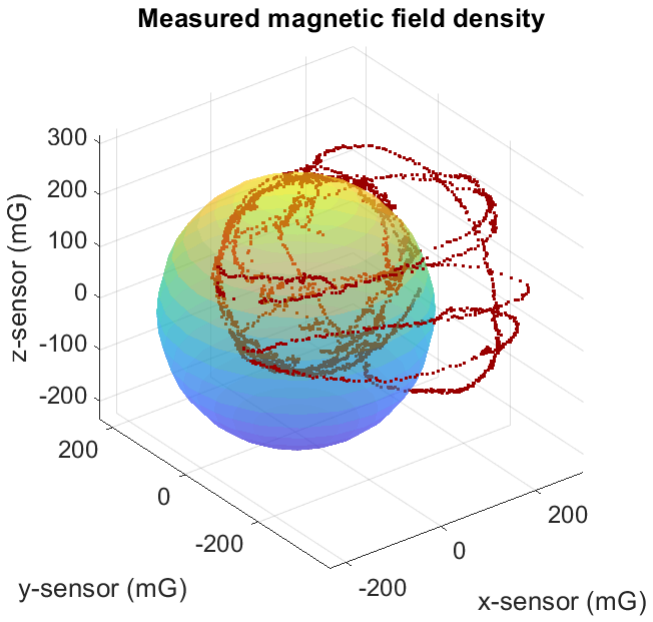

Figure 5.14 – Corrected measurements for TWOSTEP, ETS-N and ETS-A plotted with the reference sphere of radius m_t.

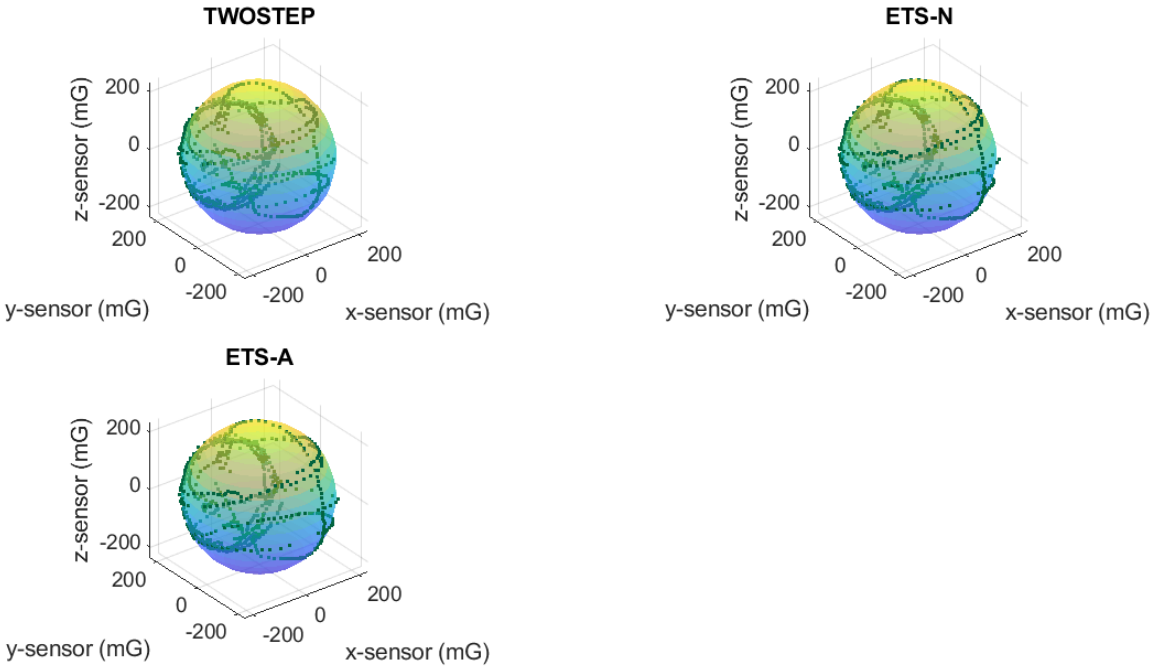

Figure 5.15 – Corrected measurements for ETS-V, MLE-A and MLE-V plotted with the reference sphere of radius m_t.

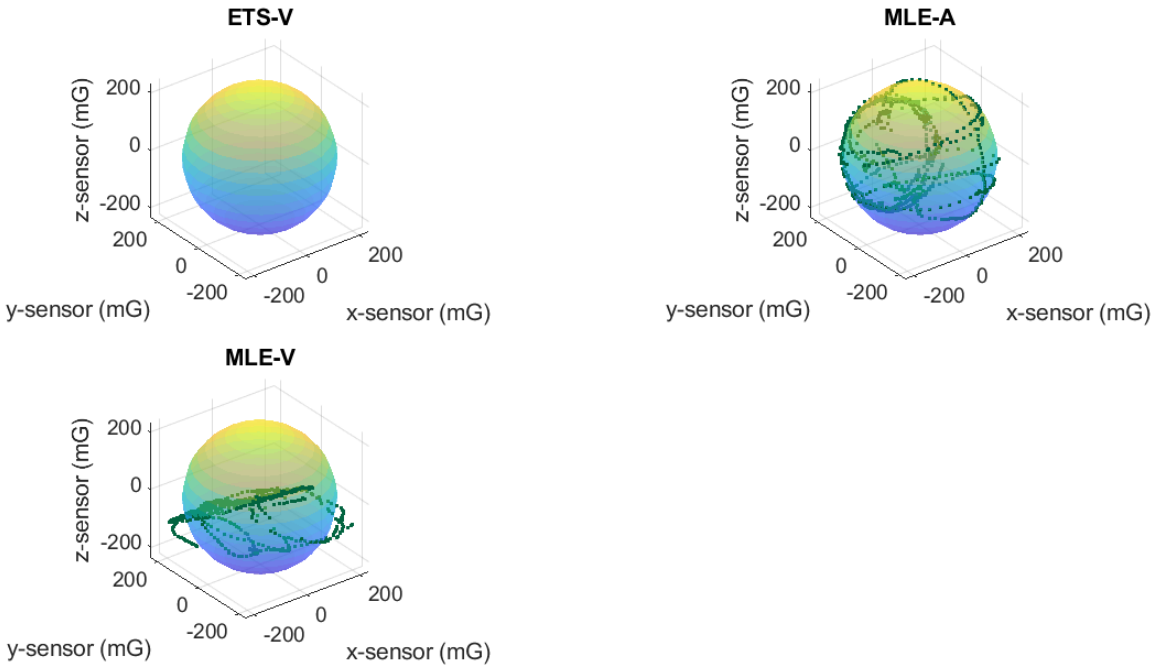

Figure 5.16 – Corrected measurements for CTLS, OML and MAG.I.C.AL plotted with the reference sphere of radius m_t.

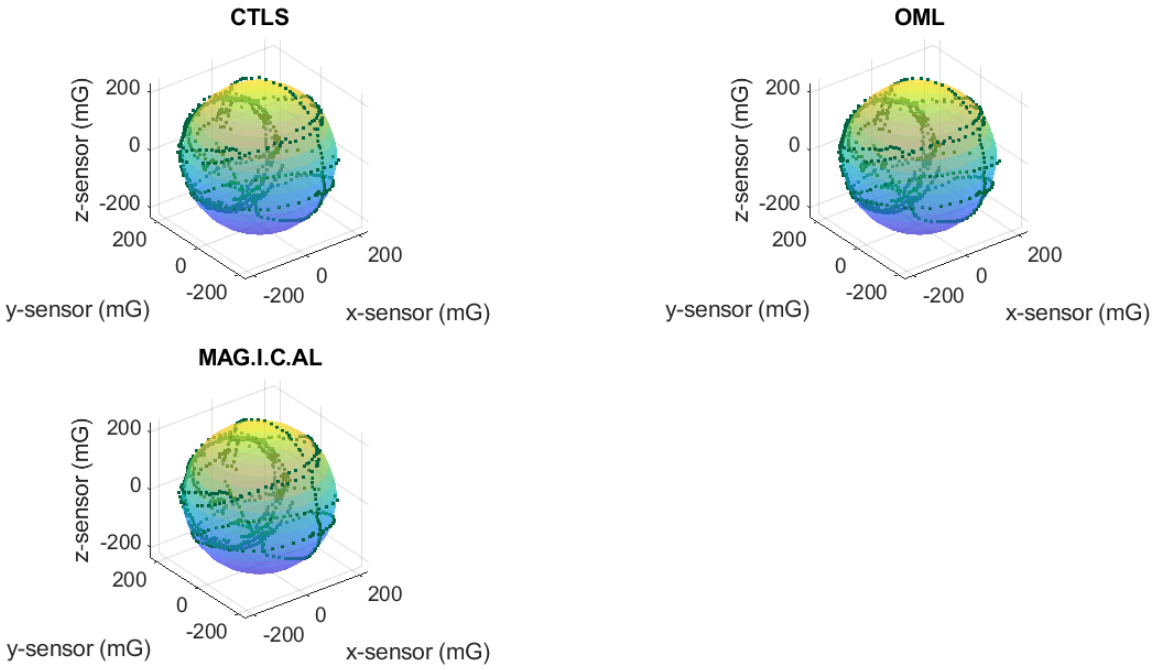

Table 5.14 – Mean Absolute Magnitude Error (MAME) for each method used in the manual calibration.

Method	Error	Unit
Before calibration	78.0483	mG
TWOSTEP	6.9294	mG
ETS-N	4.6621	mG
ETS-A	4.6621	mG
ETS-V	5.7339×10^4	mG
MLE-A	4.6466	mG
MLE-V	48.3276	mG
CTLS	5.2309	mG
OML	4.7363	mG
MAG.I.C.AL	4.7423	mG

Figure 5.17 – Magnitude error for each measurement, before and after TWOSTEP, ETS-N and ETS-A calibration procedures.

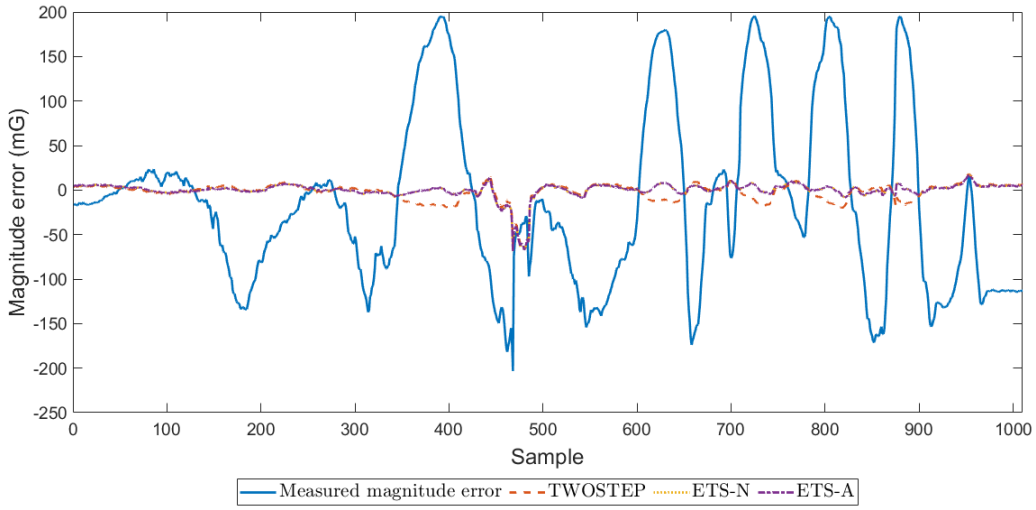

Figure 5.18 – Magnitude error for each measurement, before and after MLE-A and MLE-V calibration procedures.

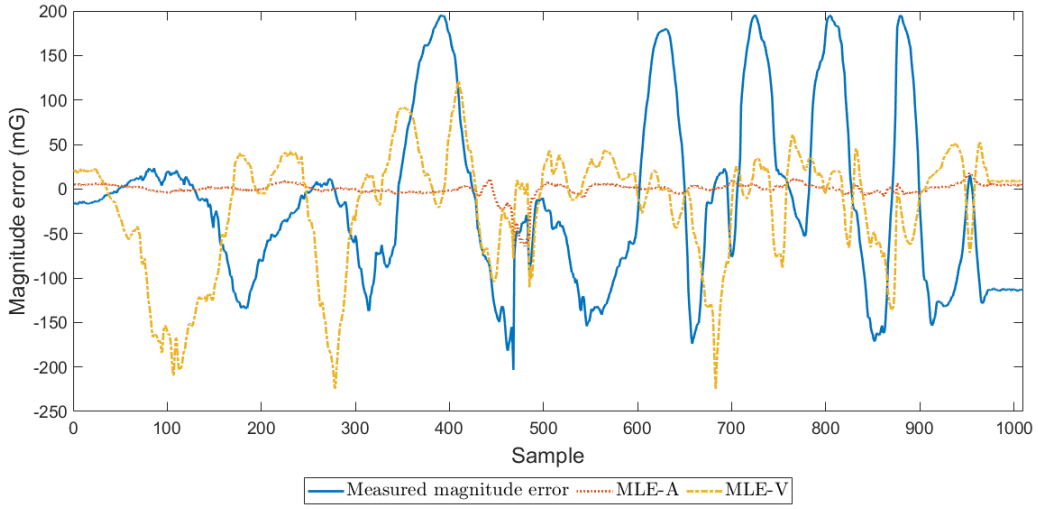

Figure 5.19 – Magnitude error for each measurement, before and after CTLS, OML and MAG.I.C.AL calibration procedures.

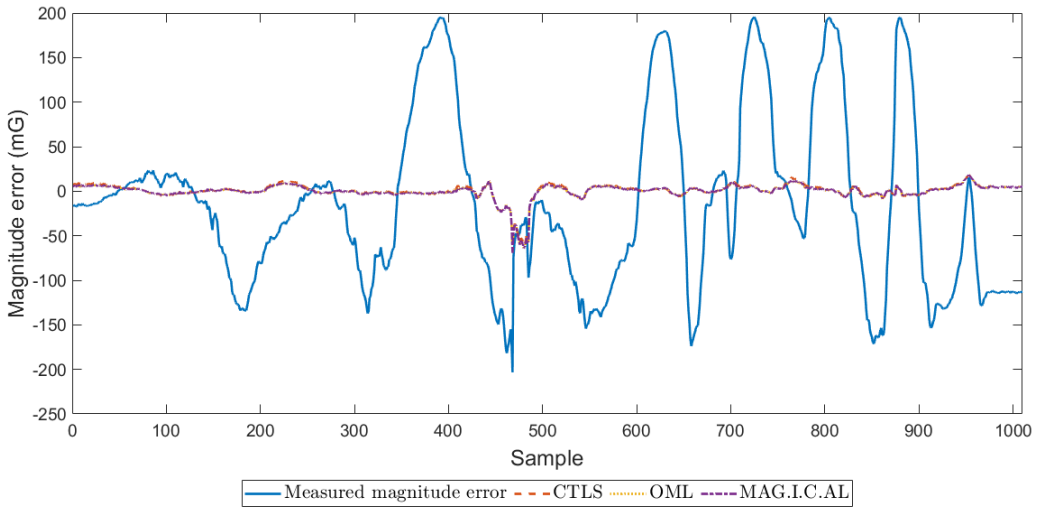

From Figures 5.13 to 5.19 and Table 5.14, we can see that most procedures performed well and similarly, except for ETS-V and MLE-V. What these methodologies have in common, as stated before, is that they rely on the partially incorrect analytical initialization solution proposed by Vasconcelos et al. (2011). In Figure 5.14, particularly, we can clearly see that the ETS-V method impaired the measurements to such an extent that the graphical scale with respect to m_t became incompatible, so that they could not be plotted together; the same occurred in Figure 5.18, where the ETS-V magnitude error is omitted due to scale incompatibility. The

MLE-V also performed poorly, but, at least, its results could still be graphically represented in Figures 5.15 and 5.18 in the same scale of the other methods.

As expected, and confirming the simulated analyses from Section 5.3, TWOSTEP, ETS-N, ETS-A, MLE-A, CTLS, OML and MAG.I.C.AL performed well, with very similar results in terms of magnitude error. Among them, the best performance, as displayed in Table 5.14, came from the MLE-A method, followed by ETS-N/ETS-A, OML, MAG.I.C.AL and CTLS, respectively. Notice, however, that MLE-A used the estimates from ETS-A as initial guesses, and not much improvement was noted. Therefore, using MLE-A may not be worth the computational effort, since the estimates from ETS-A are already accurate and the method requires much less computational power.

5.4.2 Robot Arm Aided Calibration

In this section, the calibration of a triaxial Honeywell HMC5883L magnetometer is performed with data acquired while the sensor was rotated with a robot arm Motoman MH5, using the same setup presented in Section 4.4.2. In this case, consecutive rotations were performed in one axis, while the other were monotonically rotated. As in the previous section, the original size of the data had to be reduced by calculating subsequent means, resulting in 1010 measurements. The calibration performance of each methodology can be observed in Figures 5.20 to 5.23, where the measured, corrupted and the corrected data by each methodology are plotted with the reference sphere of radius m_t (computed via WMM). Figures 5.24 to 5.26 and Table 5.15 show the magnitude error before and after each calibration procedure.

Figure 5.20 – Measured, corrupted measurements plotted with the reference sphere of radius m_t.

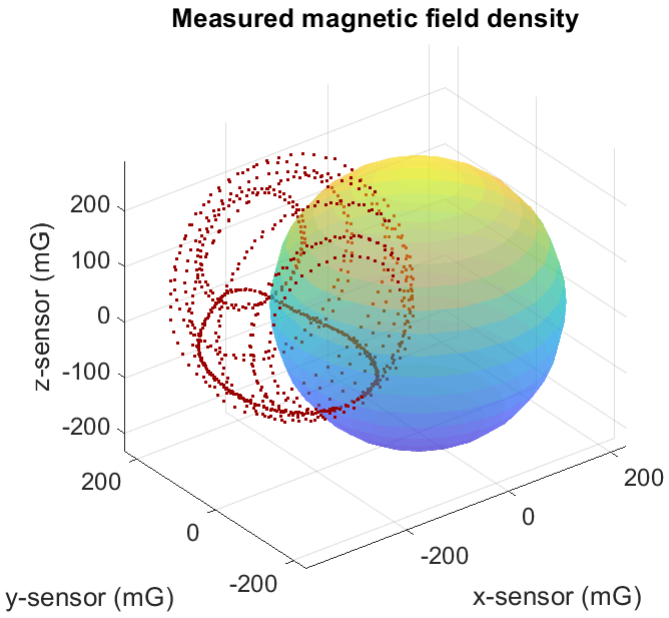

Figure 5.21 – Corrected measurements for TWOSTEP, ETS-N and ETS-A plotted with the reference sphere of radius m_t.

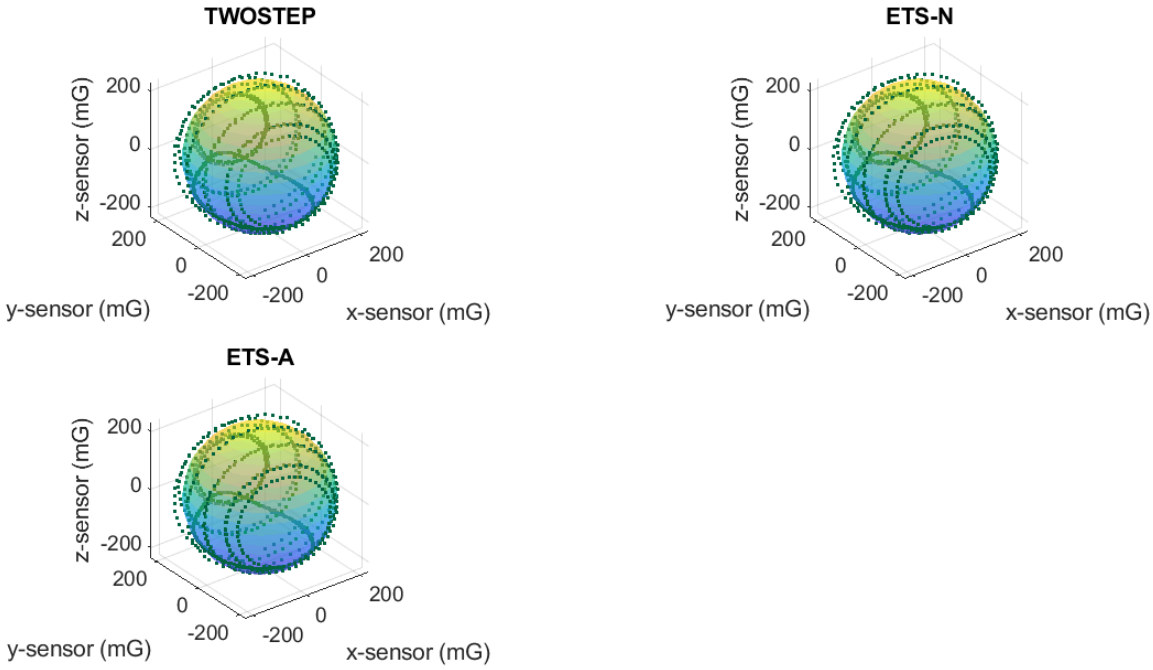

Figure 5.22 – Corrected measurements for ETS-V, MLE-A and MLE-V plotted with the reference sphere of radius m_t.

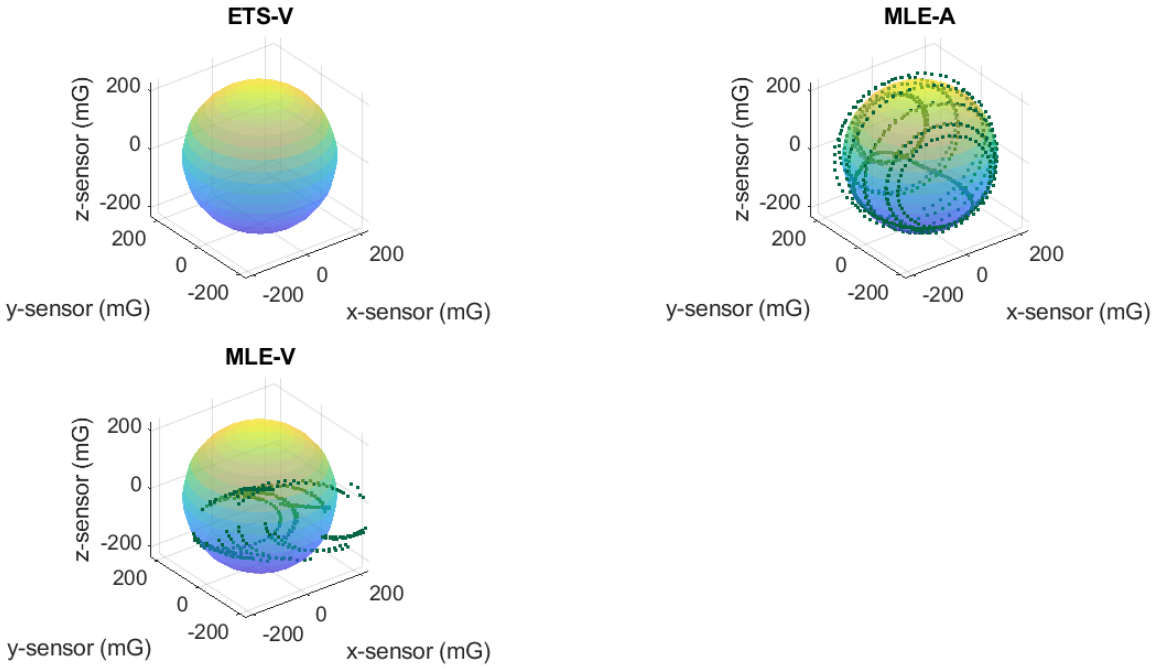

Figure 5.23 – Corrected measurements for CTLS, OML and MAG.I.C.AL plotted with the reference sphere of radius m_t.

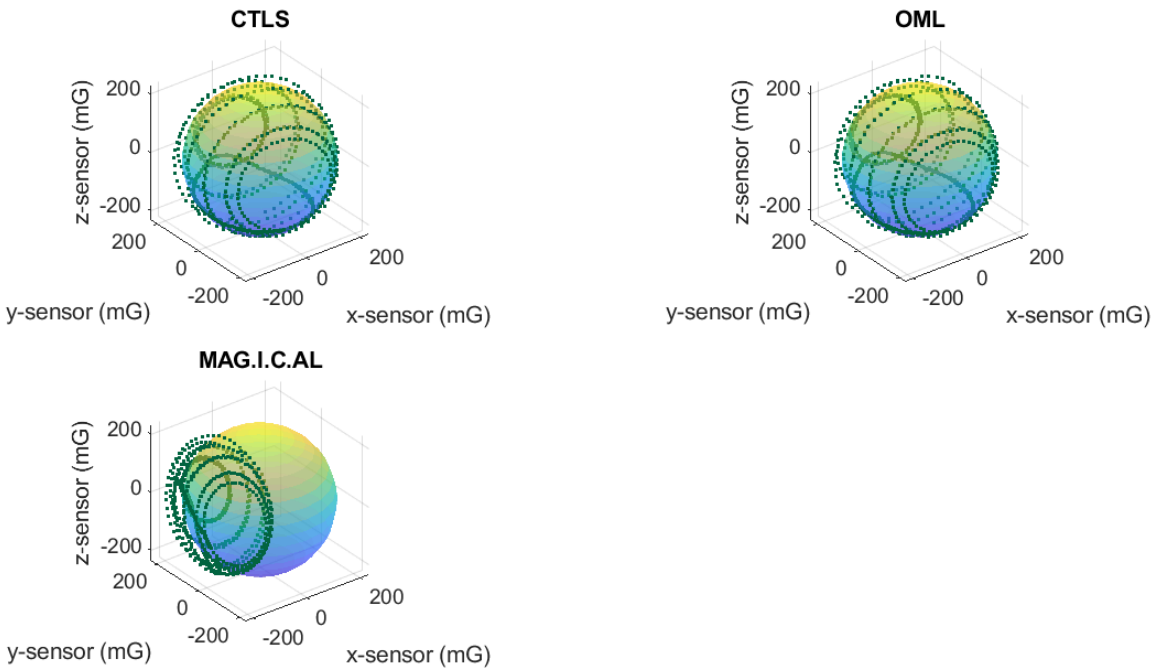

Table 5.15 – Mean Absolute Magnitude Error (MAME) for each method used in the manual calibration.

Method	Error	Unit
Before calibration	90.0533	mG
TWOSTEP	6.9425	mG
ETS-N	6.5866	mG
ETS-A	6.5866	mG
ETS-V	1.2814×10^5	mG
MLE-A	6.5559	mG
MLE-V	82.1072	mG
CTLS	6.5064	mG
OML	6.5389	mG
MAG.I.C.AL	28.2798	mG

Figure 5.24 – Magnitude error for each measurement, before and after TWOSTEP, ETS-N and ETS-A calibration procedures.

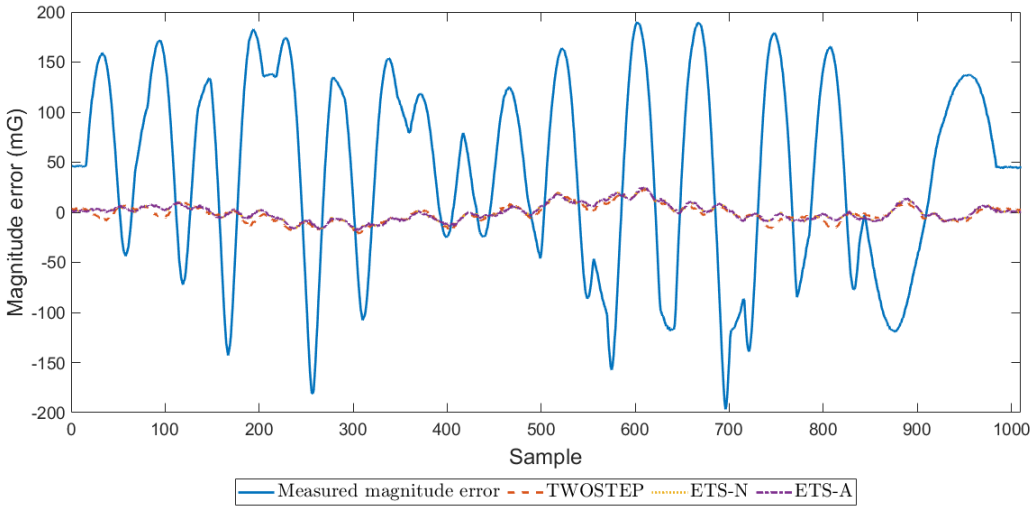

Figure 5.25 – Magnitude error for each measurement, before and after MLE-A and MLE-V calibration procedures.

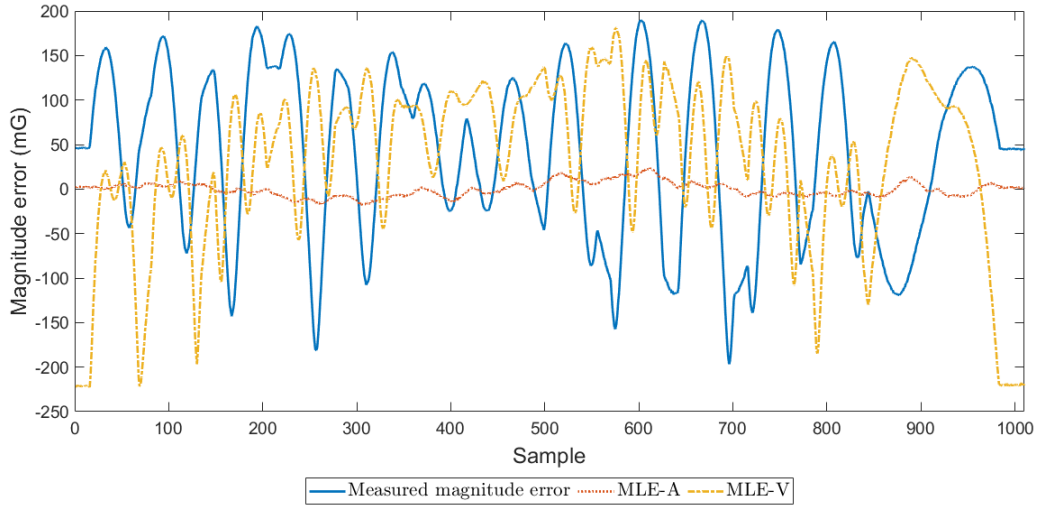

Figure 5.26 – Magnitude error for each measurement, before and after CTLS, OML and MAG.I.C.AL calibration procedures.

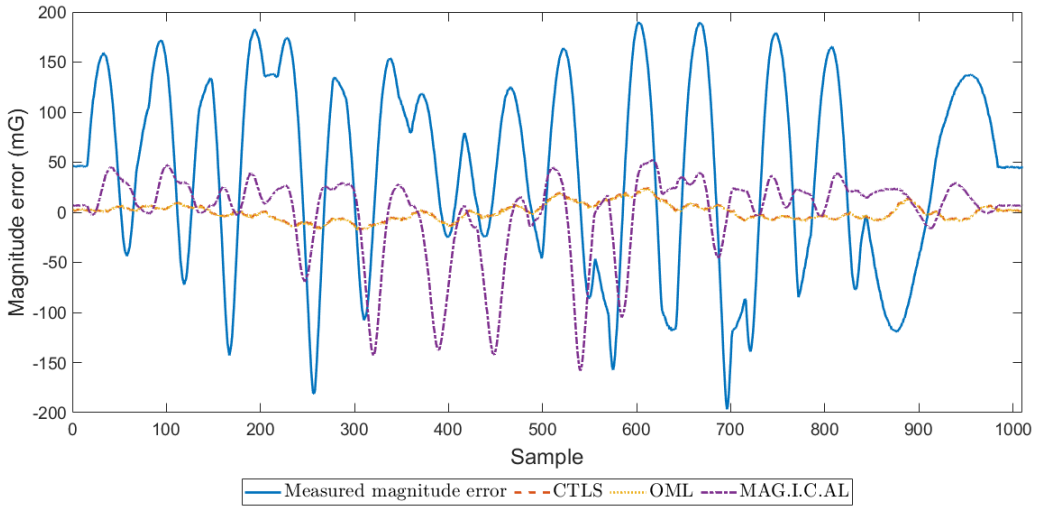

Figures 5.20 to 5.26 show that most methodologies performed well, except for those two relying on the inaccurate analytical initialization solution proposed in (VASCONCELOS et al., 2011), i.e. ETS-V and MLE-V, and MAG.I.C.AL, even though this last one performed well in the manual calibration. On the other hand, CTLS, OML, MLE-A, ETS-N/ETS-A and TWOSTEP had the best results, respectively, which also validates the analyses and verifications presented in Section 5.3. As in the manual calibration, the MAME from MLE-A is slightly

smaller than that from ETS-N/ETS-A, but such a small difference may not justify the use of the former, since it requires much more computational effort.

5.4.3 Brief Comparison between Manual and Robot Aided Calibration

In Sections 5.4.1 and 5.4.2, some calibration methodologies were shown not to converge, resulting in even more incorrect results. On the other hand, the ones that performed well, may have not been sufficiently compared regarding their ability of keeping the magnetic field density magnitude error close to zero. For this reason, Table 5.16 displays the Mean Absolute Magnitude Error (MAME) before and after each calibration procedure, for both manual and robot arm-aided calibration scenarios, as in Tables 5.14 and 5.15.

Table 5.16 – MAME before and after each calibration procedure for the manual and robot arm aided calibration.

Calibration methodology	Manual MAME (mG)	Robot Arm Aided MAME (mG)
None	78.0483	90.0533
TWOSTEP	6.9294	6.9425
ETS-N	4.6621	6.5866
ETS-A	4.6621	6.5866
ETS-V	5.7339×10^{4}	1.2814×10^{5}
MLE-A	4.6466	6.5559
MLE-V	48.3276	82.1072
CTLS	5.2309	6.5064
OML	4.7363	6.5389
MAG.I.C.AL	4.7423	28.2798

We can see from Table 5.16 that the data acquired while the sensor was fixed in the robot arm was corrupted to a larger extent, if compared to the manual data acquisition. As previously suggested, this may be due to hard and soft iron effects caused by the robot structure itself. As can also been seen, the calibration performances follow the same pattern in both scenarios, suggesting that the robot arm aided calibration also introduces errors that fit less accurately to the systematic error models adopted in the methodologies.

6 ADAPTATION OF THE EXTENDED TWO-STEP CALIBRATION METHODOLOGY FOR ACCELEROMETERS

In this Chapter, we present another contribution regarding the ETS methodology presented by Foster and Elkaim (2008): the adaptation of such technique for accelerometer calibration. Foster and Elkaim (2008) suggested that their method could be adapted for accelerometers, but no further information or experiments were provided. Using the same calibration algorithm for both magnetometers and accelerometers can be of significant practical value, since it could save computational power and require less movements in the calibration process. The following sections provide the adapted calibration method, simulated and real data experiments, respectively.

6.1 Adapted Calibration Method

Before tackling the calibration problem itself, let us remember the measurement model adopted here for accelerometers, described in (2.4):

$$\tilde{\boldsymbol{f}} = C_s C_m \boldsymbol{f} + \boldsymbol{c}_b + \boldsymbol{c}_\mu, \tag{6.1}$$

Therefore, as well as in the magnetometer calibration, the accelerometer measurement model considers three types of systematic errors: biases, scale factors and misalignments, as well as a white, zero-mean Gaussian noise.

Once we have the measurement model, considered mathematically the same as for magnetometers, we can move forward to the calibration method. The key concept in the work by Foster and Elkaim (2008) is that if an uncorrupted triaxial magnetometer was rotated into different orientations, the magnitude the three sensors would always lie on the top a sphere with radius equal to the magnitude of the Earth magnetic filed density. However, because of biases, scale factors and misalignments, the sphere becomes a shifted, rotated ellipsoid, whose estimation as a quadric surface is the first step in the calibration. After the quadric surface parameters are found, they are converted back into error parameters by the numerical or analytical means presented in Chapter 5, since they have not been originally provided by Foster and Elkaim (2008).

In order to make this valid for accelerometers, we first need a constant, known reference signal: the acceleration of gravity. For the acceleration of gravity to be the only signal measured by the sensors, the measurements should be taken only while the accelerometer is static. Thus,

the procedure consists of positioning the triaxial accelerometers into different orientations and acquiring the data while motionless. Finally, the exact same algorithms described in Chapter 5 are used. In order to have the measurements compensated for the systematic errors, the following equation shall be used:

$$\hat{\boldsymbol{f}} = \hat{C}_m^{-1}\hat{C}_s^{-1}(\tilde{\boldsymbol{f}} - \hat{\boldsymbol{c}}_b), \tag{6.2}$$

6.2 Simulated Experiments

In order to verify the performance of the ETS calibration methodology for accelerometers, the procedure has been first assessed using simulated data generated in accordance with the model from Section 6.1. The sensor was supposed to be located at a latitude of 21.758254°S, a longitude of 41.341711°W, and a height of 17 m and the gravity model described by Groves (2013) was adopted to generate the constant reference signal. A total of 17 different random orientations were simulated, and the sets of stationary accelerometer data, containing 360 samples each, were generated at a rate of 15 Hz. A random noise with variance of 0.16 mg^2 was also added. The systematic error parameters corrupting the sensor measurements are displayed in Table 6.1; the parameters were randomly chosen, according to the error ranges expected to exist for the real sensor used in Section 6.3. Figures 6.1 and 6.2 show the corrupted and calibrated data, respectively, plotted around the ideal sphere of radius g (magnitude of local gravity acceleration, computed via the aforementioned model). The data were generated via a MATLAB® implementation of the error model described in Section 6.1, in the aforementioned scenario. The analytical solution proposed in Chapter 5 was used to compute the biases, scale factors and misalignments.

Notice in Fig. 6.1 that the red dots, representing to corrupted measurements, do not lie on top of the reference sphere, meaning that they have a magnitude different from the expected one. In contrast, Fig. 6.2 shows the set of calibrated measurements lying on the top of the sphere, evidencing the effectiveness of the ETS calibration methodology for accelerometers. The latter can also be observed in Fig. 6.3, where the magnitude error is plotted before and after calibration, as a function of the accelerometer samples.

Table 6.1 – Calibration results for accelerometer simulated data

Error component	Original	Estimated	Error (%)	Unit
b_x	-0.79	-0.7900	0.0012	m/s^2
b_y	0.85	0.8501	0.0123	m/s^2
b_z	0.94	0.9401	0.0054	m/s^2
s_x	0.98	0.9800	0.0017	unitless
s_y	1.09	1.0899	0.0049	unitless
s_z	1.11	1.1100	0.0017	unitless
ρ	-6.00	-5.9990	0.0175	deg
ϕ	3.00	2.9996	0.0150	deg
λ	5.00	5.0022	0.0444	deg

In order to evaluate the minimum number of orientations required to adequately perform the accelerometer calibration, the Mean Absolute Percentage Error (MAPE) of the estimated error parameters was calculated for different numbers of orientations randomly selected. Figure 6.4 shows, in logarithmic scale, how the MAPE behaves as the number of orientations increases. Notice that nine seems to be the minimum number of orientations for a reasonable MAPE, which is logical, since there are also nine error parameters to estimate and nine parameters that model the ellipsoid. This could have been also analyzed in terms of system observability, by examining the rank.

Figure 6.1 – Generated corrupted measurements, in red, plotted with the reference sphere of radius g.

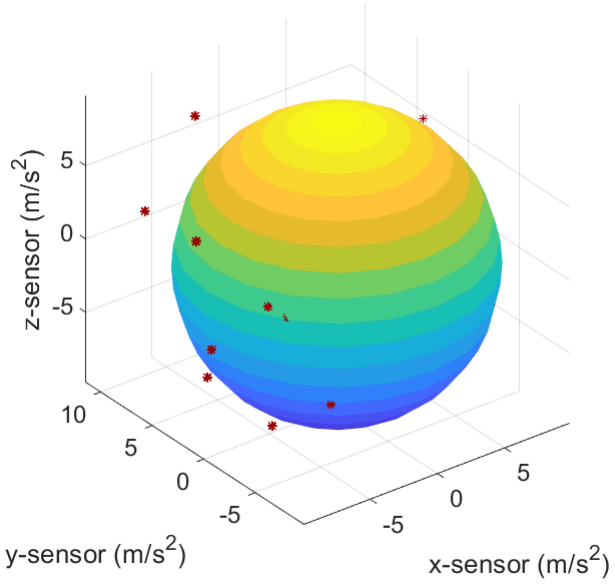

Figure 6.2 – Calibrated measurements, in green, plotted with the reference sphere of radius g.

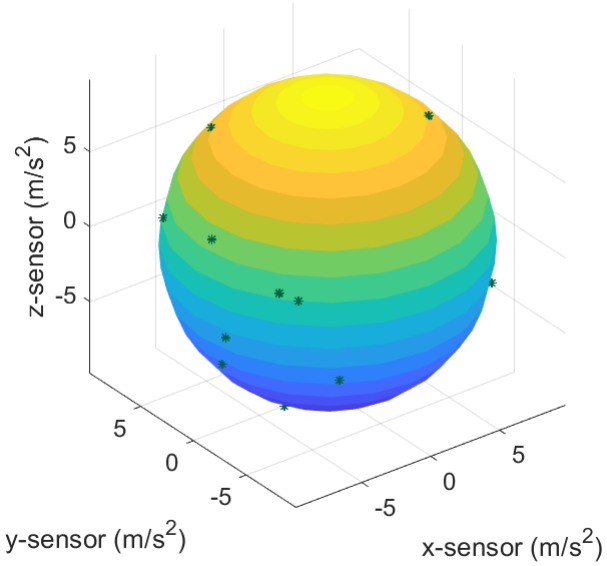

Figure 6.3 – Magnitude error for simulated corrupted and calibrated data, in red and blue, respectively.

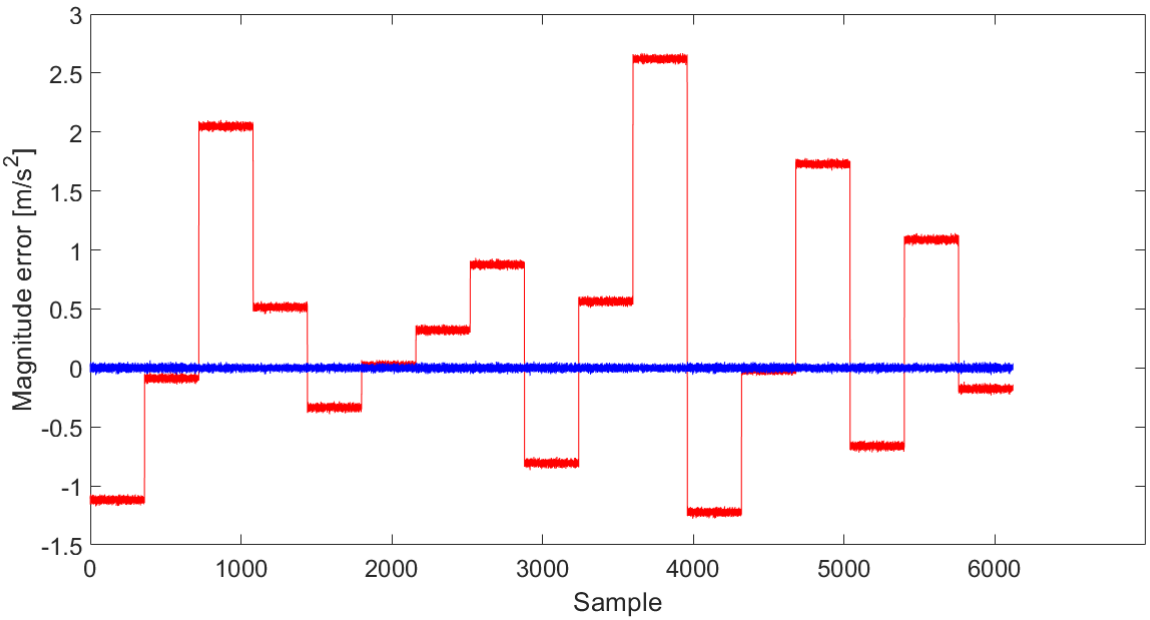

Figure 6.4 – MAPE for each calibration scenario with simulated data, varying the number of orientations.

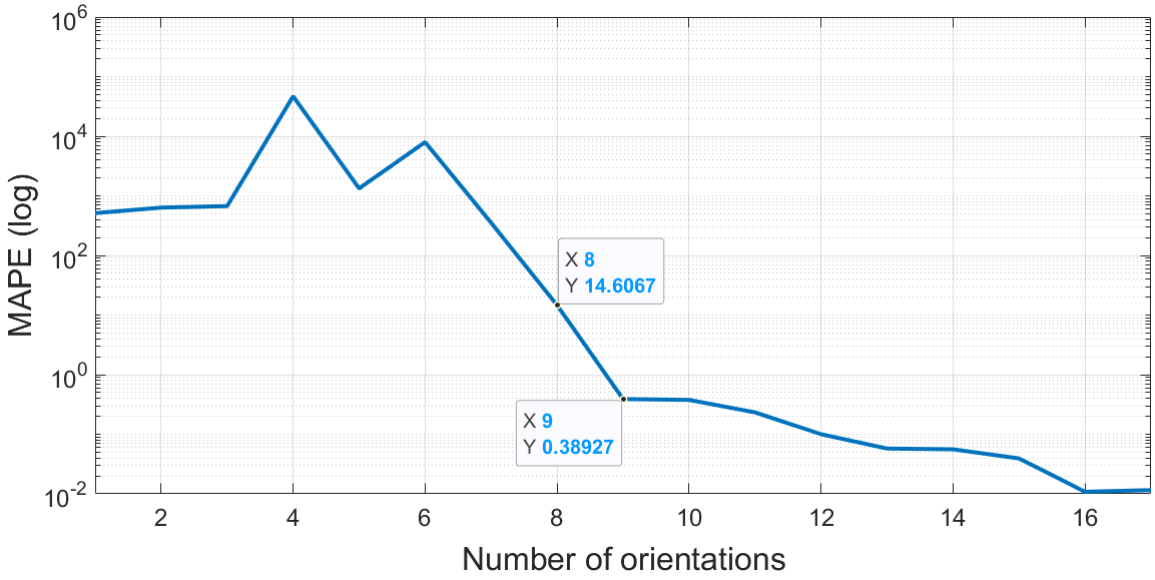

6.3 Real Data Experiments

Finally, calibration with real sensor data was performed in order to validate the adapted ETS methodology. Since one of the motivations of this work is integrated navigation, a consumer-grade triaxial accelerometer was chosen. The ADXL335 by Analog Devices uses a 10-bit Analog to Digital (A/D) converter with a range of $\pm 2g$, resulting in a resolution of $0.0039g$. The sensor was kept static in 13 different (and arbitrary) orientations, and a total of 6000 samples were acquired at a frequency of 100 Hz, which resulted in a minute procedure, not considering the transitions.

The estimated calibration parameters are displayed in Table 6.2. Notice, however, that they cannot be verified from means other than how well the corrected measurements fit the sphere of radius g. Figures 6.5 and 6.6, then, show the measured and corrected outputs of the ADXL335, respectively, plotted around the reference sphere. Notice that the same phenomenon observed in Figs. 6.1 and 6.2 is present in Figs. 6.5 and 6.6. As expected, the measurements in Fig. 6.5 do not lie on the surface of the reference sphere, but on top of a shifted, rotated ellipsoid. By estimating the ellipsoid as a quadric surface, converting its parameters into calibration parameters, and using them in (6.2) to correct the data, Fig. 6.6 is achieved, where the measurement magnitudes lie close to the sphere surface.

Table 6.2 – Calibration results for experimental data

Error component	Estimated value	Unit
b_x	0.1005	m/s^2
b_y	0.6907	m/s^2
b_z	0.9464	m/s^2
s_x	1.0408	unitless
s_y	1.0463	unitless
s_z	1.0030	unitless
ρ	0.3939	deg
ϕ	0.2956	deg
λ	0.5411	deg

Figure 6.5 – ADXL335 corrupted measurements, in red, plotted with the reference sphere of radius g.

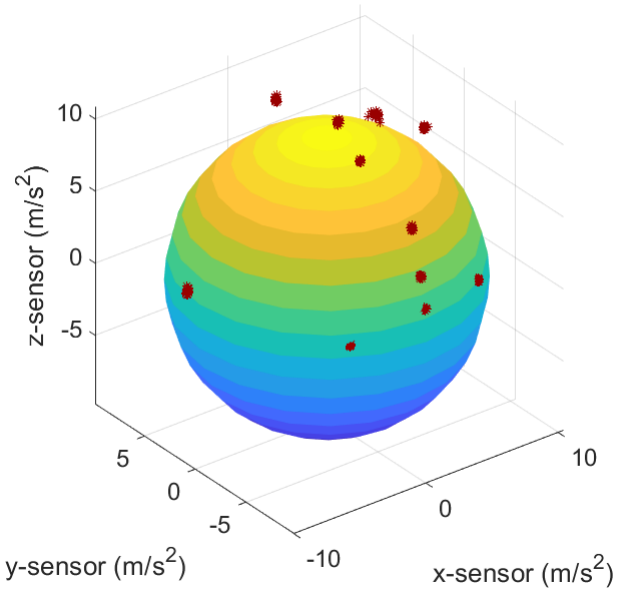

Figure 6.6 – ADXL335 calibrated measurements, in green, plotted with the reference sphere of radius g.

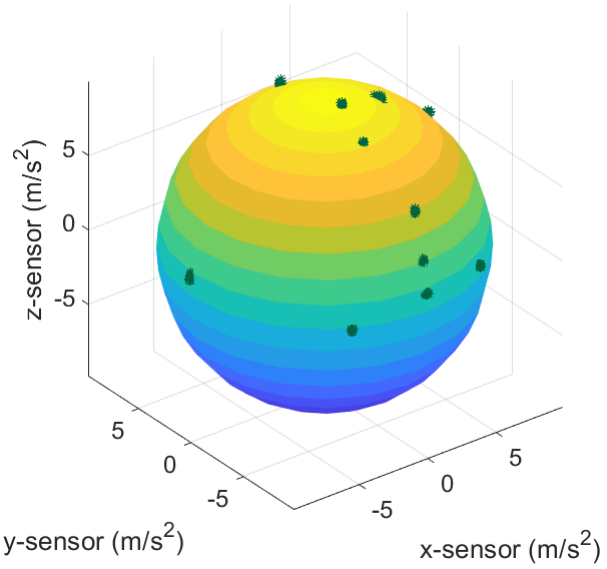

An additional way of evaluating the calibration performance is by looking at the magnitude of the specific force measurements, before and after the procedure, against the magnitude of the local gravity acceleration, calculated via the model by Groves (2013) (Fig. 6.7). Again, the plot suggests a substantial improvement.

Figure 6.7 – Magnitude error before (red) and after (blue) calibration.

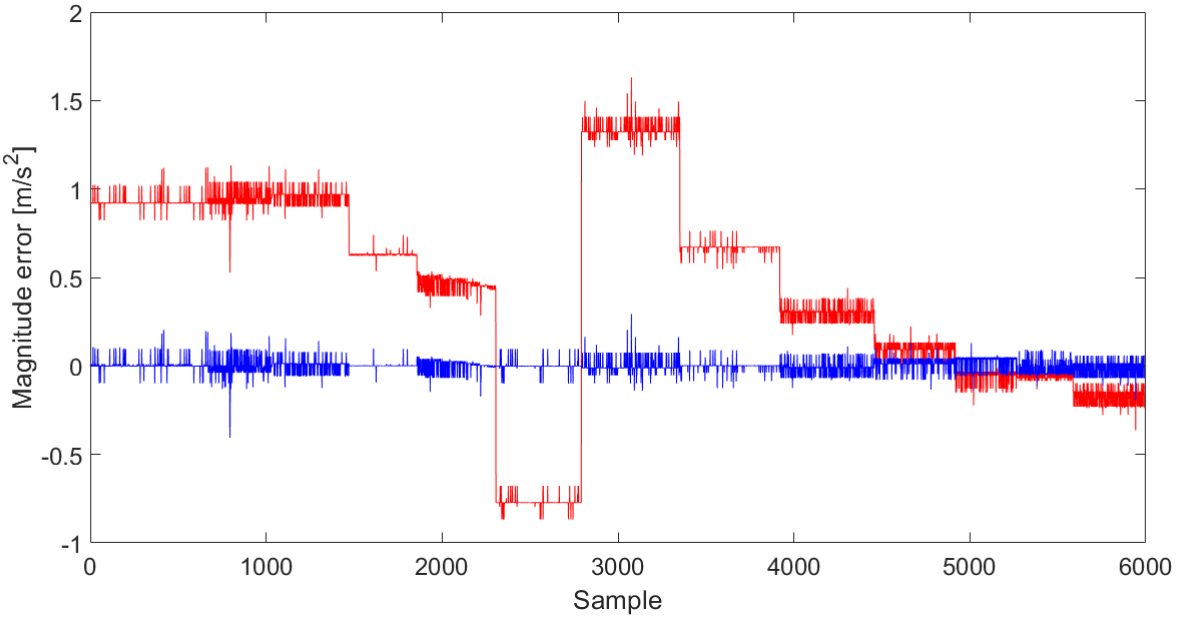

Lastly, because calibration is meant to be performed in real navigation applications, with limited computational resources, we evaluate how the correction process (6.2) performs in an embedded system using fixed-point arithmetic. For this task, we used a platform with a 32-bit computation in Q15.16 format, namely, QFire® by MWF-Dynamics, which provides a MATLAB Simulink® library for simulation and code generation. Since the correction stage must be performed in real-time, after the parameters being estimated, computation is expected to be fast enough so it does not affect the navigation solution rate. Figure 6.8 shows the implementation, where *ax*, *ay* and *az* are the measured (corrupted) data.

Figure 6.8 – Block diagram developed in Simulink, where the central block represents a QFire hardware implementation running a correction algorithm based on the estimated error parameters and the error model presented in Section 6.1.

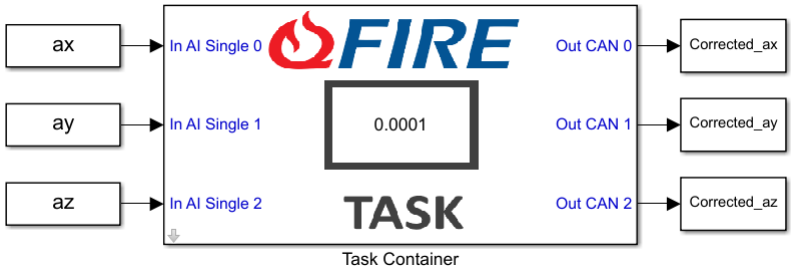

The implementation in the QFire simulator revealed good statistics with respect to processing, where the whole correction computation took only 0.1010 ms, using 1.01% of the platform's computational power. Considering, for example, a navigation system with an update rate of 100 Hz, the measurement correction time is far below the threshold of 10 ms. These values are quite representative of an embedded application, since the QFire library generates code for hardware implementation in the exact same conditions as the Simulink simulation.

7 CONCLUSION

In this work, we revisited the topic of magnetic and inertial sensor calibration, with focus on magnetometers. After briefly reviewing the concepts about accelerometers, gyroscopes and magnetometers, and presenting their measurement models with respect to systematic and stochastic errors, a bibliography review on calibration techniques was conducted. A few calibration methodologies were fully mathematically described and implemented, and contributions related to them were presented.

Chapter 1 introduced the context of this paper, which is closely related to navigation systems and its applications, such as precision agriculture, particularly important in Brazil. In sequence, the problem of costly navigation systems and their possible low-cost counterparts was described, including their issue of strongly corrupted measurements due to many sources of error, especially in magnetometers; this introduced the need for calibration in low-cost navigation systems.

In Chapter 2, the basic concepts regarding accelerometers, gyroscopes and magnetometers were reviewed. In addition, the errors that corrupt the measurements of these sensors were characterized, and models including the systematic and stochastic errors for each sensor were defined.

In Chapter 3, we reviewed the literature on the calibration of accelerometers, magnetometers, and techniques used for multiple sensors. In sequence, some of the most referred ones, i.e. TWOSTEP (ALONSO; SHUSTER, 2002b), ETS (FOSTER; ELKAIM, 2008), MLE (VASCONCELOS et al., 2011), CTLS (WU et al., 2013), OML (WU; SHI, 2015) and MAG.I.C.AL (PAPAFOTIS; SOTIRIADIS, 2019), were fully mathematically described.

In Chapter 4, novel derivations for the two-dimensional ETS magnetometer calibration methodology by Foster and Elkaim (2008) were proposed, including numerical and analytical closed-form solutions. From the latter, the ellipse (intermediate) parameters estimated in the technique could be adequately converted into the actual error parameters, namely, biases, scale factors and misalignment. In sequence, simulated experiments were performed, including a calibration example, with data generated by a model that randomly determined the corrupting errors, within the range of expected values for a consumer-grade sensor. In addition, a Monte Carlo analysis was performed in order to identify the statistical properties of the estimation errors for the proposed solutions. Finally, experiments using a real magnetometer, the HMC5883L, were conducted in two scenarios, with manual and robot aided rotation of the sen-

sor. Both simulated and real experiments demonstrated that the algorithm performs consistently and that the proposed solutions are correct.

In Chapter 5, novel numerical and analytical solutions for the three-dimensional ETS magnetometer calibration methodology presented by Foster and Elkaim (2008) were proposed. The solutions included the calculation of the biases, scale factors and misalignments, from the least squares solution of the ellipsoid fitting problem. In sequence, the new solutions were tested via simulated experiments, including a calibration example using data generated via a model whose error parameters were randomly selected within the range expected for consumer-grade magnetometers. In addition, a Monte Carlo analysis was conducted in order to evaluate the estimation error distribution resulted by the new solutions. Finally, real data experiments were performed using a Honeywell HMC5338L magnetometer. In the first scenario, the calibration was performed with data acquired while the sensor was being rotated by hand; in the second, a robot arm was used to produce the motion. Both in simulated and real data experiments, the solutions were compared with the other implemented methods, namely, TWOSTEP (ALONSO; SHUSTER, 2002b), MLE (VASCONCELOS et al., 2011), CTLS (WU et al., 2013), OML (WU; SHI, 2015) and MAG.I.C.AL (PAPAFOTIS; SOTIRIADIS, 2019). The performances of the methodologies in the experiments, in terms of accuracy, were mostly reasonable, except for some methods that presented divergence problems. The solutions proposed here performed very similarly to other traditional methods like TWOSTEP (ALONSO; SHUSTER, 2002b) and OML (WU; SHI, 2015). However, due to its characteristic of not being iterative, in the analytical case, the computational effort required is lower than in most methods, which makes the analytical solution presented here accurate, fast and straightforward. Besides, it does not incur in the problem of estimation divergence, as the iterative methods (and the proposed numerical solution) eventually do.

In Chapter 6, we presented an adaptation of the three-dimensional ETS calibration methodology proposed by Foster and Elkaim (2008) for accelerometers. The adaptation used the same solutions proposed in Chapter 5 in order to estimate the error parameters. Even though the possibility of using the ETS methodology for accelerometers was mentioned by Foster and Elkaim (2008), it had never been particularly addressed and analyzed (to the best knowledge of the author). The key point in this adaptation is the substitution of the reference signal, originally the magnitude of the Earth's local magnetic field density, by the Earth's local gravity, while the sensor is static. Simulated and real data experiments were performed in order to validate the

test. The results suggested that the calibration of accelerometers can be conducted without loss in performance.

In conclusion, the main contributions of this work were successfully presented, i.e. (a) a comprehensive bibliography review on the topic of inertial and - primarily - magnetic sensor calibration, (b) novel numerical and analytical solutions for the two- and three-dimensional ETS calibration technique proposed by Foster and Elkaim (2008), where the authors only provide an intermediate estimation. The other contributions, including the adaptation of the ETS calibration (FOSTER; ELKAIM, 2008) for accelerometers were also well described and validated. Preliminary contributions of this work have already been published by Filho et al. (2020a) and Filho et al. (2020b).

If one wishes to continue this research, we suggest the following topics for future works: (a) an analysis of how the rotations affect the calibration procedures, aiming at establishing standard movements necessary for good magnetometer and accelerometer calibrations, considering their respective particularities. (b) an analysis of how calibration of inertial and magnetic sensors influences the navigation solution in different scenarios. (c) since the presented calibration methods always rely on some kind of motion, and since such movements are often unpractical, a promising topic of research is the investigation of static calibration methodologies, like the one proposed by Silva et al. (2020). (d) as a new calibration method, implementing a least squares algorithm to directly solve for the errors, i.e. biases, scale factors and misalignments, may also be worth exploring.

REFERENCES

ALONSO, R.; SHUSTER, M. D. TWOSTEP: A fast robust algorithm for attitude-independent magnetometer-bias determination. **Journal of the Astronautical Sciences**, [New York: American Astronautical Society, c1958-, v. 50, n. 4, p. 433–452, 2002a.

ALONSO, R.; SHUSTER, M. D. Complete linear attitude-independent magnetometer calibration. **Journal of the Astronautical Sciences**, [New York: American Astronautical Society, c1958-, v. 50, n. 4, p. 477–490, 2002b.

BARBOUR, N. M. **Inertial navigation sensors**. [S.l.], 2010.

BARSHAN, B.; DURRANT-WHYTE, H. F. Inertial navigation systems for mobile robots. **IEEE Transactions on Robotics and Automation**, Institute of Electrical and Electronics Engineers, v. 11, n. 3, p. 328–342, 1995.

BONNET, S. et al. Calibration methods for inertial and magnetic sensors. **Sensors and Actuators A: Physical**, Elsevier, v. 156, n. 2, p. 302–311, 2009.

BOWDITCH, N. **The american practical navigator**. Greenbelt, Md: Defense Mapping Agency Hydrographic/Topographic Center, 1995.

CHULLIAT, A. et al. The US/UK world magnetic model for 2015-2020. BGS and NOAA, 2015.

CRASSIDIS, J. L.; LAI, K.-L.; HARMAN, R. R. Real-time attitude-independent three-axis magnetometer calibration. **Journal of Guidance, Control, and Dynamics**, v. 28, n. 1, p. 115–120, 2005.

DINALE, J. P. **Magnetic test facility-sensor and coil calibrations**. Thesis (M.Sc.) — The School of Electrical and Electronic Engineering, University of Adelaide, 2013.

DRAPER, C. S. Self-contained guidance systems. **IRE Transactions on Military Electronics**, IEEE, n. 1, p. 25–35, 1958.

ESTRICH, C.; RANGAN, K. An automated accelerometer calibration station. In: **Nat. Conf. Stand. Lab.** [S.l.: s.n.], 1989. p. 6–10.

FARRELL, J. **Aided navigation: GPS with high rate sensors**. [S.l.]: McGraw-Hill, Inc., 2008.

FILHO, R. P. M. et al. Triaxial accelerometer calibration using an extended two-step methodology. In: IEEE. **2020 Latin American Robotics Symposium (LARS), 2020 Brazilian Symposium on Robotics (SBR) and 2020 Workshop on Robotics in Education (WRE)**. [S.l.], 2020. p. 1–6.

FILHO, R. P. M. et al. Calibration of a triaxial, consumer-grade magnetometer via an extended two-step methodology. **Anais da Sociedade Brasileira de Automática**, v. 2, n. 1, 2020.

FORSBERG, T.; GRIP, N.; SABOUROVA, N. Non-iterative calibration for accelerometers with three non-orthogonal axes, reliable measurement setups and simple supplementary equipment. **Measurement Science and Technology**, IOP Publishing, v. 24, n. 3, p. 035002, 2013.

FOSTER, C. C.; ELKAIM, G. H. Extension of a two-step calibration methodology to include nonorthogonal sensor axes. **IEEE Transactions on Aerospace and Electronic Systems**, IEEE, v. 44, n. 3, p. 1070–1078, 2008.

FROSIO, I.; PEDERSINI, F.; BORGHESE, N. A. Autocalibration of MEMS accelerometers. **IEEE Transactions on Instrumentation and Measurement**, IEEE, v. 58, n. 6, p. 2034–2041, 2009.

GAMBHIR, B. Determination of magnetometer biases using module RESIDG. **Computer Sciences Corporation, Report**, n. 3000-32700, p. 01, 1975.

GEBRE-EGZIABHER, D. et al. Calibration of strapdown magnetometers in magnetic field domain. **Journal of Aerospace Engineering**, American Society of Civil Engineers, v. 19, n. 2, p. 87–102, 2006.

GLUECK, M.; BUHMANN, A.; MANOLI, Y. Autocalibration of MEMS accelerometers. In: IEEE. **2012 IEEE International Instrumentation and Measurement Technology Conference Proceedings**. [S.l.], 2012. p. 1788–1793.

GLUECK, M. et al. Real-time autocalibration of MEMS accelerometers. **IEEE Transactions on Instrumentation and Measurement**, IEEE, v. 63, n. 1, p. 96–105, 2014.

GREWAL, M. S.; HENDERSON, V. D.; MIYASAKO, R. S. Application of Kalman filtering to the calibration and alignment of inertial navigation systems. **IEEE Transactions on automatic control**, IEEE, v. 36, n. 1, p. 3–13, 1991.

GROVES, P. D. **Principles of GNSS, inertial, and multisensor integrated navigation systems**. [S.l.]: Artech house, 2013.

HEMERLY, E. M.; COELHO, F. A. Explicit solution for magnetometer calibration. **IEEE Transactions on Instrumentation and measurement**, IEEE, v. 63, n. 8, p. 2093–2095, 2014.

HORN, R. A.; HORN, R. A.; JOHNSON, C. R. **Topics in matrix analysis**. [S.l.]: Cambridge university press, 1994.

JURMAN, D. et al. Calibration and data fusion solution for the miniature attitude and heading reference system. **Sensors and Actuators A: Physical**, Elsevier, v. 138, n. 2, p. 411–420, 2007.

KAYTON, M.; FRIED, W. R. **Avionics navigation systems**. [S.l.]: John Wiley & Sons, 1997.

KROHN, A. et al. Inexpensive and automatic calibration for acceleration sensors. In: SPRINGER. **International Symposium on Ubiquitious Computing Systems**. [S.l.], 2004. p. 245–258.

LANGLEY, R. B. The magnetic compass and GPS. **GPS World**, p. 70–80, 2003.

LÖTTERS, J. C. et al. Procedure for in-use calibration of triaxial accelerometers in medical applications. **Sensors and Actuators A: Physical**, Elsevier, v. 68, n. 1-3, p. 221–228, 1998.

MARIOLI, D.; SARDINI, E.; TARONI, A. A computerized system for the very low frequency calibration of accelerometers. In: **Proc. 6th Int. Symp. Intelligent Instrumentation for Remote and On-Site Measurements, U@ KO TC-4, Antwerp, Belgium**. [S.l.: s.n.], 1993. p. 437–442.

MOLIN, J. P.; AMARAL, L. R. do; COLAÇO, A. **Agricultura de precisão**. [S.l.]: Oficina de Textos, 2015.

MUCCIACCIA, S.; FRIZERA, A.; SALLES, E. Algoritmo direto de calibração de magnetômetros triaxiais por ajuste de elipsoide utilizando distância algébrica. In: **XXI Congresso Brasileiro de Automática**. [S.l.: s.n.], 2016. p. 2884–2889.

PANG, H. et al. Calibration of three-axis magnetometers with differential evolution algorithm. **Journal of Magnetism and Magnetic Materials**, Elsevier, v. 346, p. 5–10, 2013.

PAPAFOTIS, K.; SOTIRIADIS, P. P. MAG. IC AL.–A Unified Methodology for Magnetic and Inertial Sensors Calibration and Alignment. **IEEE Sensors Journal**, IEEE, v. 19, n. 18, p. 8241–8251, 2019.

RENAUDIN, V.; AFZAL, M. H.; LACHAPELLE, G. New method for magnetometers based orientation estimation. In: IEEE. **IEEE/ION Position, Location and Navigation Symposium**. [S.l.], 2010. p. 348–356.

RENK, E. L. et al. Calibrating a triaxial accelerometer-magnetometer-using robotic actuation for sensor reorientation during data collection. **IEEE Control Systems Magazine**, IEEE, v. 25, n. 6, p. 86–95, 2005.

SÄRKKÄ, O. et al. A multi-position calibration method for consumer-grade accelerometers, gyroscopes, and magnetometers to field conditions. **IEEE Sensors Journal**, IEEE, v. 17, n. 11, p. 3470–3481, 2017.

SILVA, F. O. et al. Three-axis attitude determination with pseudo-bias estimation from gravity/magnetic vector observations. **Journal of Guidance, Control, and Dynamics**, American Institute of Aeronautics and Astronautics, v. 43, n. 12, p. 2237–2257, 2020.

SPRINGMANN, J. C.; CUTLER, J. W. Attitude-independent magnetometer calibration with time-varying bias. **Journal of Guidance, Control, and Dynamics**, v. 35, n. 4, p. 1080–1088, 2012.

STEWART, G. W. **Matrix Algorithms: Volume 1: Basic Decompositions**. [S.l.]: SIAM, 1998.

THÉBAULT, E. et al. International geomagnetic reference field: the 12th generation. **Earth, Planets and Space**, Springer, v. 67, n. 1, p. 79, 2015.

THOMPSON, D. (Ed.). **The Concise Oxford Dictionary**. 9th ed.. ed. Oxford, U.K.: Oxford University Press, 1995.

TITTERTON, D.; WESTON, J. L. **Strapdown inertial navigation technology**. [S.l.]: IET, 2004. v. 17.

VARMUZA, K.; FILZMOSER, P. **Introduction to multivariate statistical analysis in chemometrics**. [S.l.]: CRC press, 2016.

VASCONCELOS, J. F. et al. Geometric approach to strapdown magnetometer calibration in sensor frame. **IEEE Transactions on Aerospace and Electronic systems**, IEEE, v. 47, n. 2, p. 1293–1306, 2011.

VČELÁK, J. et al. AMR navigation systems and methods of their calibration. **Sensors and Actuators A: Physical**, Elsevier, v. 123, p. 122–128, 2005.

WANG, J.-H.; GAO, Y. A new magnetic compass calibration algorithm using neural networks. **Measurement Science and Technology**, IOP Publishing, v. 17, n. 1, p. 153, 2005.

WON, S.-h. P.; GOLNARAGHI, F. A triaxial accelerometer calibration method using a mathematical model. **IEEE Transactions on Instrumentation and Measurement**, IEEE, v. 59, n. 8, p. 2144–2153, 2009.

WU, Y.; SHI, W. On calibration of three-axis magnetometer. **IEEE Sensors Journal**, IEEE, v. 15, n. 11, p. 6424–6431, 2015.

WU, Z. et al. Constrained total least-squares calibration of three-axis magnetometer for vehicular applications. **Measurement Science and Technology**, IOP Publishing, v. 24, n. 9, p. 095003, 2013.

WU, Z.; WANG, Z.; GE, Y. Gravity based online calibration for monolithic triaxial accelerometers' gain and offset drift. In: IEEE. **Proceedings of the 4th World Congress on Intelligent Control and Automation (Cat. No. 02EX527)**. [S.l.], 2002. v. 3, p. 2171–2175.

WU, Z. et al. Calibration of three-axis magnetometer using stretching particle swarm optimization algorithm. **IEEE Transactions on Instrumentation and Measurement**, IEEE, v. 62, n. 2, p. 281–292, 2012.

XIAOMING, Z. et al. Calibration of triaxial MEMS vector field measurement system. **IET Science, Measurement & Technology**, IET, v. 8, n. 6, p. 601–609, 2014.

ZHANG, N.; WANG, M.; WANG, N. Precision agriculture—a worldwide overview. **Computers and electronics in agriculture**, Elsevier, v. 36, n. 2-3, p. 113–132, 2002.

ZHANG, Z.-Q.; YANG, G.-Z. Micromagnetometer calibration for accurate orientation estimation. **IEEE Transactions on Biomedical Engineering**, IEEE, v. 62, n. 2, p. 553–560, 2014.

ZHU, R.; ZHOU, Z. Calibration of three-dimensional integrated sensors for improved system accuracy. **Sensors and Actuators A: Physical**, Elsevier, v. 127, n. 2, p. 340–344, 2006.

APPENDIX A

In this Section, we explain the Kronecker product, also referred to as direct or tensor product, which was used in Section 3.4.3. It is defined for the multiplication of matrices with arbitrary sizes (HORN; HORN; JOHNSON, 1994). By definition, the Kronecker product, whose operator is $\otimes$, of $A = [a_{ij}] \in M_{m,n}$ and $B = [b_{ij}] \in M_{p,q}$ is:

$$A \otimes B = \begin{bmatrix} a_{11}B & \dots & a_{1n}B \\ \vdots & \ddots & \vdots \\ a_{m1}B & \dots & a_{mn}B \end{bmatrix} \in M_{mp,nq} \tag{A.1}$$

Therefore, it consists of multiplying each element of matrix A by the entire matrix B, and organizing the results as in the former. Notice hence, that $A \otimes B \neq B \otimes A$. More properties of the Kronecker product can be found in (HORN; HORN; JOHNSON, 1994).

APPENDIX B

In this section, we explain the Modified Gram-Schmidt algorithm used in Chapter 3 for decomposing the true error matrix $M_t = C_s C_m$ into the product of a positive diagonal, upper (or lower) triangular matrix times and orthogonal one. In the following routine, the Modified Gram-Schmidt algorithm by Stewart (1998) is presented, where the $n \times p$ matrix X is factorized into QR, where Q is the orthonormal matrix and R is a positive diagonal, upper triangular matrix.

```
for k = 1:p
    Q(:,k) = X(:,k);
    for i = 1:k-1
        R(i,k) = Q(:,i)'*Q(:,k);
        Q(:,k) = Q(:,k) - R(i,k)*Q(:,i);
    end
    R(k,k) = norm(Q(:,k))';
    Q(:,k) = Q(:,k)/R(k,k);
end
```

The Modified Gram-Schmidt algorithm was used in Chapter 3 as we wanted to decompose M_t into the product of a positive diagonal upper triangular matrix, times an orthogonal one, and not the opposite, as generally provided by the Modified Gram-Schmidt decomposition algorithm. To solve that, it sufficed applying the decomposition over the inverse of M_t.

Conversely, for obtaining the decomposition of M_t as the product of a positive diagonal, lower triangular matrix times an orthogonal one, it sufficed applying the Modified Gram-Schimdt decomposition on the transpose of M_t. Such M_t decomposed matrices, when algebraic related, allowed us to convert the positive diagonal upper triangular matrix $\boldsymbol{T}$ provided by OML into the sought diagonal positive lower triangular matrix $C_s C_m$, as showed in Chapter 3.4.5.